TOPOLOGY OPTIMIZATION ALGORITHMS FOR ADDITIVE MANUFACTURING

by

Andrew T. Gaynor

A dissertation submitted to The Johns Hopkins University in conformity with the requirements for the degree of Doctor of Philosophy.

Baltimore, Maryland

February, 2015

Abstract

Topology optimization is a powerful free-form design tool that couples finite element analysis with mathematical programming to systematically design for any number of engineering problems. Additive manufacturing (AM), specifically 3D printing, is a manufacturing process where material is added through deposition or melting in a layer-by-layer fashion. Additively manufactured parts are 'built' from the bottom up, allowing production of intricate designs without extra effort on the part of the engineer or technician – complexity is often said to be 'free'. This dissertation seeks to leverage the full potential of this burgeoning manufacturing technology by developing several new design algorithms based on topology optimization. These include multi-material projection methods appropriate for multiphase 3D printers, an overhang-prevention projection method capable of designing components that do not need sacrificial anchors in metal AM processes, and models for simultaneously optimizing topology and objects embedded in process. These algorithms are demonstrated on several design examples and shown to produce solutions with capabilities that exceed existing designs and/or that require less post-processing in fabrication.

ABSTRACT

Targeting the capabilities of the Polyjet Stratasys 3D printers, a topology optimization algorithm is developed for the design of multi-material compliant mechanisms in which the algorithm ultimately designs both the topology of the part and the placement of each material – one stiff, one more compliant. Results – obtained through development of a both a new multi-material model and through development of a robust topology optimization technique for the elimination of one-node hinges – show the ability to place both soft and stiff material and lead to dramatic improvements in performance of compliant mechanisms.

One of the manufacturing challenges in metal powder-based 3D printing technologies is material curling due to internal stress development from the heating and cooling cycle during the printing process. To counteract this phenomena, sacrificial support material is introduced to anchor the part to the build plate, which must then be removed chemically or mechanically in post-production: a time consuming process. Components requiring no post-printing material removal are achieved through development of a topology optimization algorithm to design components to respect a designer-prescribed maximum overhang angle, such that the optimized part can be manufactured without using sacrificial support anchors. Solutions are shown to satisfy the prescribed overhang constraint, along with minimum feature length scale constraints as needed.

Finally, an algorithm is developed considering the ability to embed discrete objects such as stiffeners or actuators within a monolithic printed part. Herein, a hybrid

ABSTRACT

continuum-truss topology optimization algorithm is developed to leverage this potential capability, where the algorithm designs not only the continuum phase, but also places discrete truss members within this phase. With an eye towards future AM capabilities, the algorithm is demonstrated on the more contemporary design problem of strut-and-tie models in reinforced concrete design. It is shown that the algorithm is especially useful for designing within complex design domains in which the flow of forces is not obvious. While an exciting direction, it is noted that further advancements in 3D printing technology are needed to allow for such printed topologies.

Primary Reader: James K. Guest (Advisor)

Secondary Readers: Lori Graham-Brady, Sauleh Siddiqui

Acknowledgments

A special thanks to my friends and family, who have supported me along the way.

Dedication

This thesis is dedicated to my wonderful family.

Contents

List of Figures

Chapter 1

Introduction

Topology optimization, an extremely powerful free-form rigorous design method, was introduced in 1988 by the pioneering work of (Bendsøe and Kikuchi, 1988). The method allows the engineer to define the design problem in terms of the desired functionality without requiring a priori knowledge of a typical solution. In this way, innovative solutions are often obtained for even the most straight forward of design problems. With the research field gaining traction, there is a high rate of adoption in academia and industry, creating an ever increasing need to develop new algorithms to design for advanced mechanics and new manufacturing methods. While a powerful tool, one of the disadvantages has been the complexity of the solution topologies, with many critiquing that the solutions are theoretically optimal yet typically difficult or impossible to manufacture.

Additive manufacturing (AM), specifically 3D printing, is a burgeoning technology

in which parts are manufactured by depositing or melting material a layer-by-layer manner. Until recently, the technology was primarily known as rapid prototyping, owing to the fact that it was almost exclusively used to create prototypes for parts which were ultimately to be manufactured by another manufacturing method. With the advancement in printing technology and the understanding and development of new printing materials, there has been a shift towards creating 'end-use' parts via AM. This is especially true with the advancement of metal 3D printing methods such as selective laser melting (SLM). While it is exciting to see the shift to manufacturing actual final parts using AM, the parts that are typically manufactured have topologies determined by the restrictions of older manufacturing methods.

In this dissertation, a new design paradigm is proposed in which topology optimization is harnessed as the design tool for additively manufactured parts, capitalizing on the design freedoms allowed by additive manufacturing and the rigorous design methodology of topology optimization. While there has been high interest in using AM to manufacture parts, the design of the built parts is almost always dictated by older, more geometrically restrictive manufacturing methods, as these parts were engineered when AM was not an option. Therefore, there must be a fundamental shift in approach in order to take full advantage of AM. Every traditional part must be reimagined/reengineered by use of topology optimization, in which the engineer defines the part by way of functionality by defining loads and boundary conditions, and subsequently allows the optimizer to determine the optimal topology. There exist

exciting directions in which the additive manufacturing process may be incorporated into the topology optimization formulation to not only eliminate post-processing of the topology optimization solution to be fed into the printer, but also eliminate the physical post-processing required on the manufactured part.

Manufacturability has long been an issue of topology-optimized solutions, and has been a major hurdle in the adoption of this technology in industry. There have been recent efforts to alter the topology optimization formulation to incorporate manufacturing constraints such that the final solution is manufacturable for the specified method. For example, Guest and Zhu (2012) optimized for the structure assuming a milling manufacturing process. Others have looked at incorporating manufacturing uncertainty - both material and geometric - in the optimization process, producing robust solutions (Asadpoure et al., 2011; Guest and Igusa, 2008; Jalalpour et al., 2011; Jansen et al., 2013; Schevenels et al., 2011; Sigmund, 2009).

1.1 Topology Optimization Background

Topology Optimization is formulated as a material distribution scheme in which a problem is defined by a design domain and applied loads and boundary conditions. The design domain is discretized into a finite elements that each have a material density, ρ^e, where e indicates the particular element. The objective of the optimization is to determine the material distribution to optimize a specified performance perime-

ter, driving each element to either zero, a void element, and one, a solid element. Topology optimization is most commonly formulated as a minimum compliance, or equivalently, maximum stiffness problem. The optimization formulation is as follows:

$$\begin{aligned} \min_{\boldsymbol{\rho}} \quad & f(\boldsymbol{\rho}) = \boldsymbol{F}^T \boldsymbol{d} \\ \text{subject to:} \quad & K(\boldsymbol{\rho})\boldsymbol{d} = \boldsymbol{F} \\ & \sum_{e \in 1} \rho^e v^e \leq V \\ & 0 \leq \rho^e \leq \rho^e_{\max} \quad \forall\, e \in \Omega \end{aligned} \tag{1.1}$$

where design variable vector $\boldsymbol{\rho}$ is the set of material densities for the structure, ρ^e is material concentration in element e, $\boldsymbol{F}$ if the vector of applied nodal loads, $\boldsymbol{d}$ is the vector of nodal displacements, v^e is element volume for unit ρ^e, V is the available volume of material, and $\rho^e_{\max}$ is the design variable upper bound. While the ultimate goal is to drive towards a binary 0-1 solution, the optimization problem is relaxed to a continuous optimization problem in which ρ may vary between 0 and $\rho_{\max}$ (with $\rho_{\max} = 1$ indicating solid material) so that efficient gradient based optimizers may be used. There is, however, a penalization applied to intermediate volume fraction elements so that they are deemed inefficient, ultimately driving the solution towards 0-1 (Bendsøe, 1989; Rozvany et al., 1992).

There are a number of well-known challenges in solving the topology optimization problem, including manufacturability of designs and numerical instabilities of solution mesh dependence and checkerboard patterns (Sigmund and Petersson, 1998). An effi-

cient, and physically meaningful approach to addressing these issues is to prescribing a minimum length scale below which features may not appear. While several options exist, such as imposing length scale control through constraints (Poulsen, 2003), a popular technique for imposing minimum length scale is through the Heaviside Projection Method (HPM) (Guest et al. 2004) where independent design variables are projected onto the physical (finite element) space over the prescribed length scale. The details are not provided here, but the general form is seen in Eq. 1.2. Variables are often located at the nodes of the finite element mesh, and if a nodal design variable is "turned on", it will project material in a specified $r_{\min}$ around the nodal point. All nodal variables have the ability to be "on" or "off", giving the algorithm the capacity to create custom geometries. Figure 1.1 is an image of the Heaviside Projection Method as seen from the element perspective. All of the ϕ within the specified $r_{\min}$ can project material to the element. By way of the Heaviside function in Eq. 1.2, even if a nodal variable indicates it barely "wants" to project material, the Heaviside function will project the material fully. This function, Eq. 1.2, helps create a crisp solid void boundary to the topology.

As seen in Fig. 1.1, the starred element determines whether it is solid or void based on whether the circular nodal variables within the specified minimum radius, $r_{\min}$ project material. The continuous approximation to the Heaviside function is seen in Eq. 1.2 and visually in Fig. 1.2:

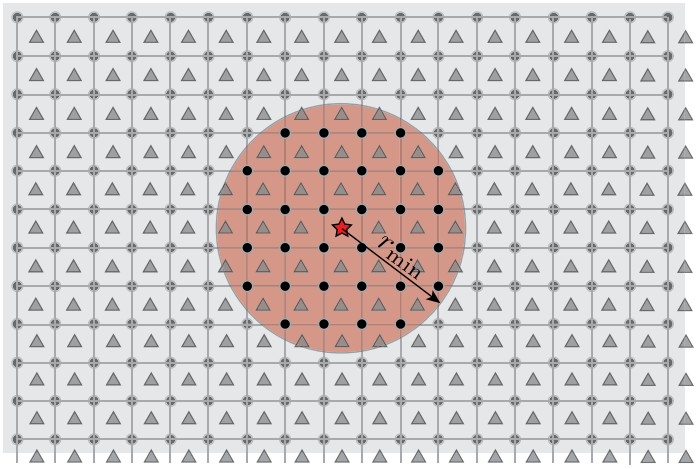

Figure 1.1: The stared element can have material projected onto it by any nodal ϕ within the radius $r_{\min}$

$$\rho^e = H(\mu^e(\phi)) = 1 - e^{-\mu^e(\phi)\beta} + \mu^e(\phi)e^{-\beta} \tag{1.2}$$

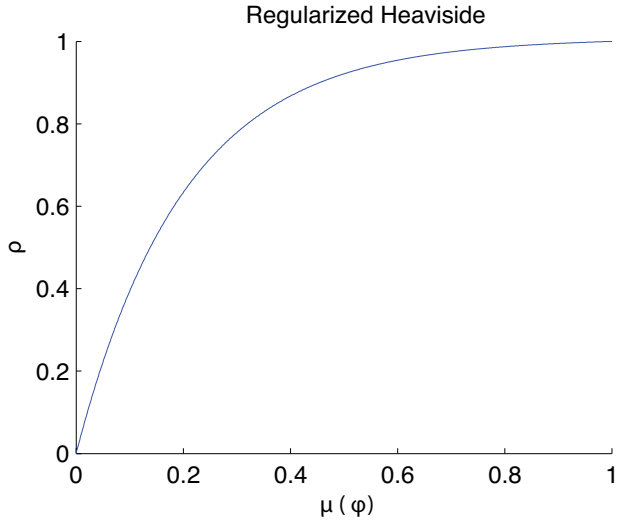

Figure 1.2: Projection of ϕ to ρ to achieve minimum length scale control.

where μ^e is the linearly decaying weighted average of the design variables within the minimum allowable radius, $r_{\min}$, and β is the Heaviside exponent. As β approaches

infinity, the continuous approximation to the Heaviside function (Eq. 1.2 approaches the discontinuous true Heaviside function). As such, it is desired to perform the optimization with as large of β as possible. This will give a solution with minimal fading on the boundary. However, when the Heaviside parameter, β, becomes very large, the optimization problem becomes highly nonlinear, creating an optimization problem which may be hard for the gradient-based optimizer to solve (Guest et al., 2011).

A typical solution for a simply supported beam is seen in Fig. 1.3c where the volume fraction is set to 60%. The solution is first obtained for the case of no length scale control and then for a minimum radius of 2.4. As can be seen by the simple comparison, the projection scheme for length scale control not only allows for control over the minimum feature size, but also eliminates such issues as checkerboard solutions, as seen in Fig. 1.3b.

Other topology optimization researchers use a similar method to achieve a minimum length scale, where a projection of elemental design variables onto the physical space creates the same minimum allowable feature size (Bendsøe and Sigmund, 2003b).

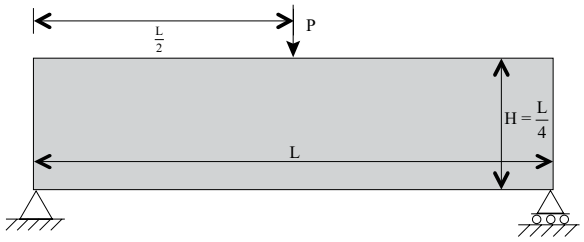

a Simply Supported Beam Definition

b Simply Supported Beam Solution, no length scale control

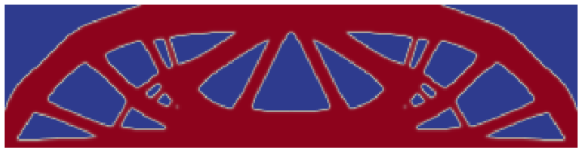

c Simply Supported Beam Solution, $r_{\min} = 2.4$

Figure 1.3: Simply Supported Beam Definition and Solutions for volume fraction of 60% on a $320 * 80$ mesh

1.2 Additive Manufacturing Background

As stated above, additive manufacturing is a layer-by-layer manufacturing method which builds parts from the bottom up. The first AM technology, Stereolithography (SLA), was patented by Chuck Hull and brought to market in 1986 through his newly formed company, 3D Systems. SLA is a liquid bath 3D printing technique in which a thin layer of photopolymer is selectively cured by an ultraviolet light. Upon curing one layer, the base print plate sinks another small amount into the liquid polymer bath and the selective curing is performed again – this process repeats until the part is completely formed. To this day, SLA has the best available print resolution of any

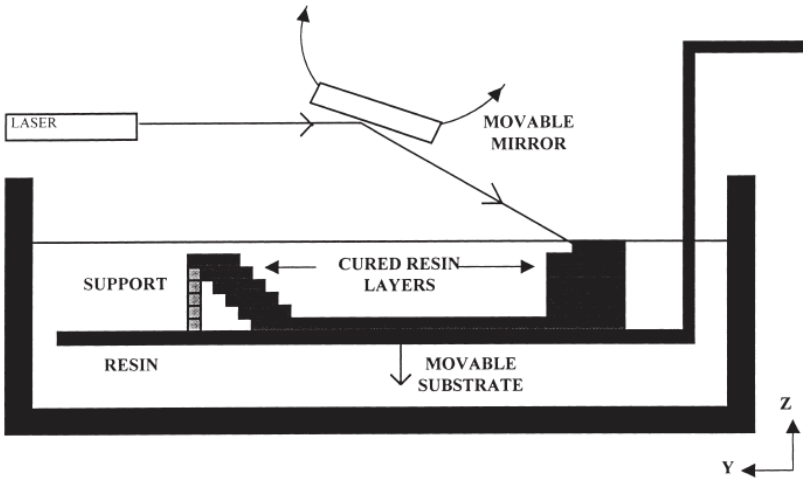

Figure 1.4: Schematic of stereolithography AM process (Pham and Gault, 1998)

AM technology on the market. Interestingly, recent advancements in 3D printing have allowed for the use of photopolymer to be placed through a print head instead of selectively cured in a polymer bath. This allows for the use of multiple material, a topic which will be explored in depth in Chapter 2.

Probably the most common additive technology currently on the market, Fused Deposition Modeling (trademark of Stratasys), or more generally Fused Filament Fabrication (FFF), was commercialized in 1990 by S. Scott Crump, the founder of Stratasys. In this technology, a plastic filament is heated and extruded through a print head and subsequently is selectively deposited in a layer-by-layer fashion to create the final part. There are a number of materials available for this method including PLA, ABS, polycarbonate, and ULTEM, to name a few.

Of great interest are powder-bed 3D printing methods. This technology creates physical parts through melting or sintering of powdered material in a layer-by-layer

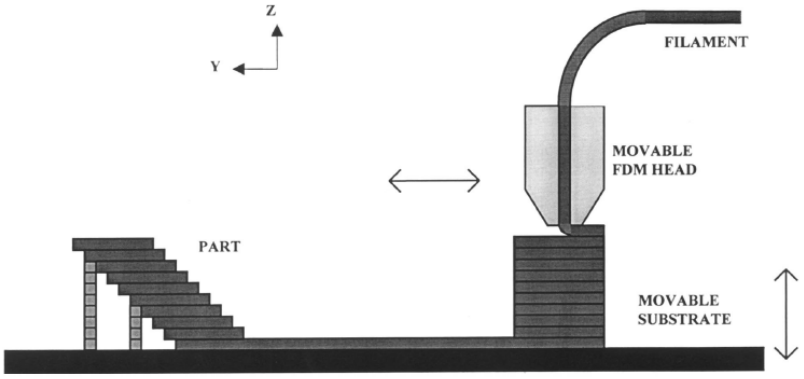

Figure 1.5: Schematic of Fused Deposition Modeling AM Process (Pham and Gault, 1998)

fashion. A number of materials may be used in this process, including polymers and metals. In the case of polymers, the material solidified together by Selective Laser Sintering (SLS), while in the case of metals, the solid material is formed by Selective Laser Melting (SLM). Often SLS and SLM are used interchangeably, however sintering and melting are fundamentally two separate processes. With the advancement of metal SLM technology, the ability to create 'end-use' metallic parts is becoming a reality, allowing for more complex design and ultimately weight savings in many parts. This is of particular interest to the automotive and aerospace industries, where weight reduction equals significant monetary savings.

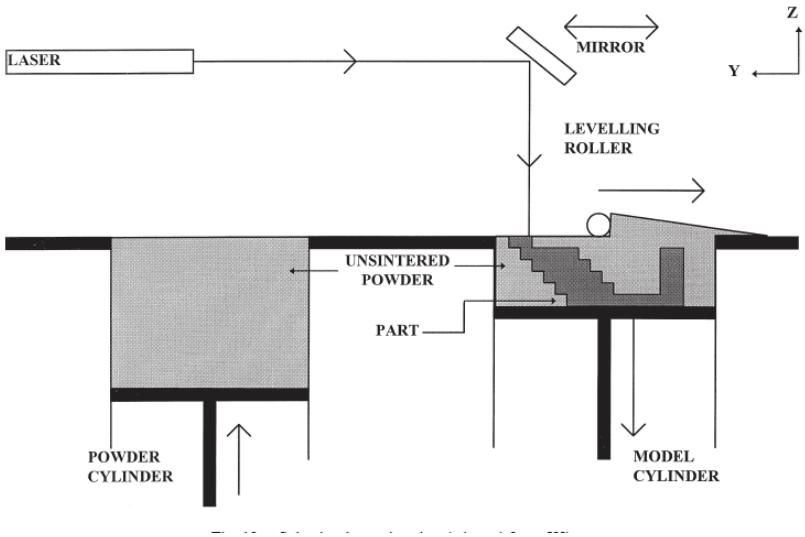

Figure 1.6: Schematic of Selective Laser Sintering AM Process (Pham and Gault, 1998)

1.3 Topology Optimization In Additive Manufacturing Overview

Due to the relative infancy of both topology optimization and additive manufacturing, there is limited literature on the combined use of these technologies. In the past few years, however, a few research groups across many disciplines have discovered this technology and exploited for application to manufacturing and medicine.

In light of the ability of AM to manufacture almost any complex topology, researchers have come to the realization that topology optimization can and should serve as the design tool for these structures. The ability to simply specify the problem in terms of loads, boundary conditions, design domain an other necessary design considerations, in many cases allows for design never realized before. The designs are

not only manufacturable, but have optimal performance in comparison to traditional designs. Some have investigated the use of ground structure optimization techniques – in which a truss ground structure is specified within the design domain and the cross-sectional areas of the truss are optimized - to exploit the design freedoms of AM (Smith et al., 2013). In this study, the authors verified the optimality of the solutions by printing and testing the parts. Interestingly, they found some geometrical discrepancies between the optimized solution and the printed representation. This reinforces the necessity to properly account for and incorporate the manufacturing process limitations and variability into the topology optimization formulation so that there is no disconnect from design to print. Others have investigated the general idea of combining topology optimization and additive manufacturing to take advantage of potential weight savings (Emmelmann et al., 2011; Villalpando et al., 2014), and for product family design, exploiting the customizability enabled by additive manufacturing (Lei et al., 2014).

Support material, required for a number of AM technologies, is necessary to ensure the manufacturability of all topologies. For certain techniques, the material is different from that of the structural part and may be dissolved away in a chemical bath, while in other printing methods, the support material is the same as that of the structural part and must be removed by grinding or etching in a post print process. It has been found that the support material is critical in minimizing geometric distortions and in dissipating energy away from the location of the print-head or laser location in

the case of selective laser melting technology. Interestingly, a number of researchers have investigated harnessing optimization for the design and minimization of AM support structure. Brackett proposes, yet does not execute, a method to eliminate the need for support material all-together by taking advantage of the maximum printable overhang angle which requires no support (Brackett et al., 2011a). In this way, the final topologies would be restricted to overhang angles less than this experimentally determined angle. However, it should be noted that there is a significant disconnect between the proposed constraint and the desired effect. The lack of solutions leaves doubt as to whether the algorithm will work at all. Similarly, while not performing a formal optimization, Cloots manipulated the printing parameters to both maximize the achievable overhang angle and minimize the need for support material altogether (Cloots et al., 2013). Krol proposes a method aimed at minimizing the material use for support material in SLM methods using fractal patterns (Krol et al., 2012). With a similar end goal, Strano proposes a method to minimize the use of material using a cellular support structure (Strano et al., 2013). Finally, Paul investigated the part orientation in relation to support material and found that the best orientation for part quality also resulted in the greatest use of support material, underscoring some of the tradeoffs in support material minimization (Paul and Anand, 2014).

Also fairly prevalent in recent literature is the use of topology optimization in conjunction with additive manufacturing for medical application, notably tissue scaffolds. Some have optimized for the multi functionality required by tissue scaffolds

(Almeida and Brtolo, 2013; Dias et al., 2014). There scaffolds must hold a structural load while having enough porosity for fluid to flow through the material. This area has also been explored in the topology optimization community (Challis et al., 2010, 2012; Chen et al., 2011; Guest and Prévost, 2006, 2007). While not using topology optimization explicitly, Rainer obtained the principal stress trajectories for a particular part and subsequently oriented the sparse-fill in the direction of these trajectories as opposed to the default horizontal and vertical grid-like infill pattern (Rainer et al., 2012).

1.4 Dissertation Scope and Aims

This dissertation aims to create topology optimization algorithms which design for particular additive manufacturing methods. In terms of scope, manufacturing science will not be investigated as part of this work. Instead the focus will be on developing topology optimization algorithms with enough generality to apply to plethora of additive manufacturing design problems. Also, heuristics are generally avoided, with the methods instead based on incorporating manufacturing processes and material properties into the optimization formulation.

Chapter 2 will focus on formulating an algorithm to design for a printer with multi-material capabilities. The algorithm will be exemplified through the design of multi-material compliant mechanisms. Chapter 3 will focus on designing parts

that require no sacrificial support material in the build process. This algorithm applies to almost all printing technologies, but herein will focus on SLM 3D printers. Finally, Chapter 4 will present a method for optimizing for the placement of discrete objects within a 3D printed part. The algorithm not only allows for the placement of objects, but accounts for the stress-dependent material properties often exhibited in 3D-printed parts.

Chapter 2

Multiple-Material Topology Optimization of Compliant Mechanisms Created Via PolyJet 3D Printing

2.1 PolyJet 3D Printing

PolyJet 3D printing is one of the only AM processes capable of utilizing stiff and flexible material phases within a single build, making it uniquely qualified for manufacturing complex, multi-material compliant mechanisms. PolyJet 3D printing is an AM material jetting process, wherein droplets of liquid photopolymer are deposited

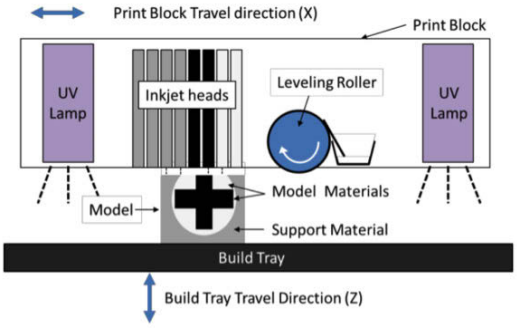

Figure 2.1: Representation of direct 3D PolyJet printing process.

directly onto an elevator substrate via a series of inkjet printheads (Obj, 2009). As the material is deposited, two ultraviolet (UV) lamps cure the photopolymer in multiple passes. Each subsequent layer is jetted on top of the previous one. A representation of this process can be seen in Fig. 2.1.

The PolyJet process offers a high resolution print, with a layer thickness of 16-30 microns and an in-plane resolution of 42 microns. In addition, the PolyJet process offers one significant and unique advantage among modern additive manufacturing process: the PolyJet process is capable of depositing two different materials on a pixel-by-pixel basis. One material is a rigid, white plastic-like material (VeroWhite+), while the other is an elastomeric, flexible black material (TangoBlack+). The two materials can be combined in various ratios to create nine gradient material blends with properties ranging along the continuum of the two extremes.

2.2 Compliant Mechanisms

Howell defines compliant mechanisms as those which utilize the deformation of flexible members to successfully transfer motion, force, and energy (Howell, 2013). This is in direct contrast to traditional mechanisms that rely on movable joints in order to perform their function. Compliant mechanisms are encountered on a daily basis in the forms of binder clips, paper clips, and various compliant latches. In addition to the various man-made examples, nature also makes use of compliant mechanisms, with many living organisms displaying parts that are both strong and flexible (Vogel, 1995). Advantages of compliant mechanisms include part consolidation, improved mechanism robustness, and miniaturization as friction dominates at small scales. However, as the design of compliant mechanisms increases in complexity, traditional manufacturing methods become infeasible. This drives the authors' overall goal of integrating design optimization with additive manufacturing (AM) methods, with a particular focus herein on the design and fabrication of compliant mechanisms.

While there are many examples of single-material compliant mechanisms present in everyday life, man-made, multi-material compliant mechanisms are rare. This is because manufacturing complexity increases significantly with the introduction of additional material phases. However, there is potential to drastically increase performance by producing multi-material compliant mechanisms. For example, Aguirre and Frecker make a strong case for the need of multi-material compliant mechanisms in the medical field (Aguirre and Frecker, 2010). By including both a stiff and flexible

material phase in the design of contact-aided compliant mechanism forceps for natural orifice translumenal endoscopic surgery, the authors were able to achieve larger total jaw openings and blocked forces. This improved mechanism performance has the potential to directly impact the success rate of the surgery. However, Aguirre and Frecker's design was guided by their intuitive understanding of how forceps should look.

A few example compliant mechanisms are shown in Fig. 2.2. Presented here are tweezers, pliers and a gripping wrench mechanism. As can be seen, the mechanisms do not have any explicit hinges, instead attaining motion through bending of the compliant hinges.

This chapter takes a more systematic design approach based on topology optimization to leverage multi-material AM processes. By including multiple material phases such as these in the design of compliant mechanisms, the maximum deflection of the mechanism can potentially be improved, while potentially decreasing the likelihood of fatigue failure at the structure's joint-like sections.

2.2.1 Manufacturing of Multi-Material Compliant Mechanisms

While literature has offered some discussion regarding how to optimize the design of multiple material compliant mechanisms, there has been little content detailing

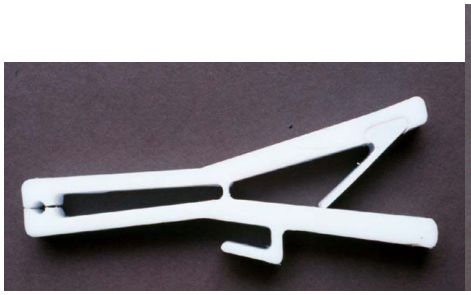

a Tweezers

b Pliers

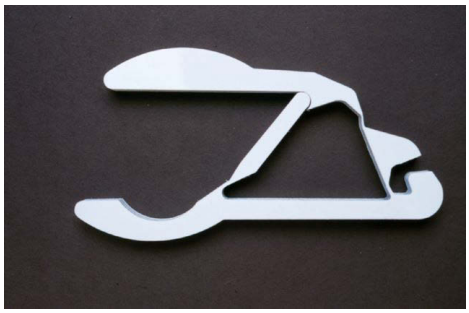

c Gripper

Figure 2.2: Example compliant mechanisms. Motion is attained through deformation of the hinges. From (BYU, 2014).

their actual fabrication. The few instances of literature pertaining to the fabrication of multiple material compliant mechanisms will be discussed herein, but it is important to note that none of the objects fabricated have been subjected to structural optimization. Following a review of the literature, it is concluded that there is no prior work where multiple material compliant mechanisms have been designed, optimized, and subsequently fabricated.

One of the more prevalent examples of the manufacturing of multiple-material compliant mechanisms is from Bailey and Rajagopalan. They discuss the design and manufacturing of a biomimetic leg that operates under the principle of heterogeneous material compliance (Bailey et al., 1999; Rajagopalan et al., 2001). While the final design is not driven by the concept of optimization, the authors specifically address the process of multi-material. They adapt the process of Shape Deposition Manufacturing (SDM) to allow for the creation of flexible joints while maintaining stiff members for the rest of the leg shape. SDM involves the deposition of material in layers, followed by machining in order to form the material layer into the desired shape (in this way it is like a combination of additive manufacturing and traditional CNC machining). Because the process offers continuous access to the part interior, specialized subpieces can be embedded during creation. In this case, the authors embedded separate flexible joints in their biomimetic leg.

Several authors have also investigated the use of multi-material molding (MMM) for the creation of multiple material compliant mechanisms (Bejgerowski et al., 2010,

2011; Gouker et al., 2006). MMM is a process whereby the various materials in the final part are created volumetrically, as opposed to the layer-by-layer methods of both AM and SDM. While there are several variations on the process, the general MMM flow involves the creation of a one material phase being molded separately and then being inserted into a mold for the second stage material phase. Filling this second stage mold will embed the first material phase within the part.

For the fabrication of small-scale multiple material compliant mechanisms, there are two examples that are derivations of the MMM process. Rajkowski proposes a prototyping process that uses a curable rigid polymer as well as a curable, flexible silicone as the two material phases (Rajkowski et al., 2009). By placing the material phases down in bulk and using a mask to cure only the desired sections of the part, the author offers a quick, inexpensive solution for the fabrication of multiple-material mechanisms on the millimeter scale. Vogtmann proposes a process whereby the negative space for the flexible material phase is cut from a bulk piece of the rigid phase (Vogtmann et al., 2011). The flexible material is deposited, cured, and planed, before the desired mechanism profile is cut from the bulk material.

While the above processes have been shown to successfully create multiple material compliant mechanisms, they all also have limitations when considering complexity and distributed compliance of the final pieces. The examples presented are relatively geometrically simple when compared to traditional results of multiple-material optimization, and thus were all manufacturable. However, these processes do not scale

well. As the complexity of topology and multi-material distribution increases, the processes will require significantly more user interaction and time investment to create the necessary mechanisms. In addition, the presented examples all rely on the principle of lumped compliance, where the flexible material phase is implemented at the location that would traditionally be represented by a revolute joint. These processes would be ill-prepared to manufacture mechanisms based on distributed compliance, where the flexible material phases would be more interspersed among the rigid material.

2.2.2 Potential For Compliant Mechanism Design Through Topology Optimization

Topology optimization will serve as an excellent design tool for compliant mechanisms. To tackle the design problem, the general compliant mechanism design domain is defined (with applied forces, supports, and desired responses) and material is systematically distributed (added or removed) throughout the domain in a manner that minimizes (or maximizes) the defined objective function within a prescribed set of design constraints – usually a material volume constraint. This results in the effective and efficient use of material within the part. The use of the topology optimization approach as applied to the design of compliant mechanisms can be traced back to work by Sigmund, as well as by Frecker and coauthors (Frecker et al., 1997; Sigmund, 1997).

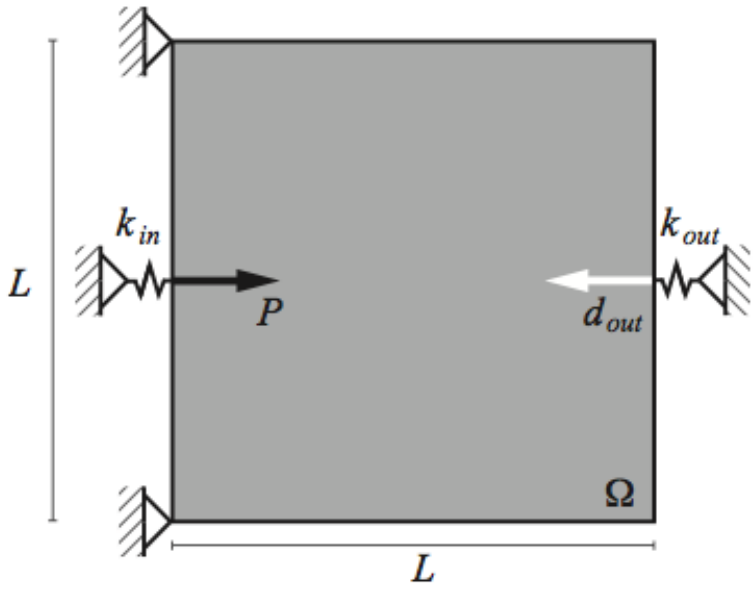

Figure 2.3: Design domain and loading for inverter case study.

In order to demonstrate the utility of the presented optimization and printing method, the authors consider the well-established example of a force inverter compliant mechanism. This case study was initially demonstrated in Sigmund (1997) and has become one of the benchmark problems in topology optimization. As seen in Fig. 2.3 the design domain for the mechanism is square, with the displacements at the top and bottom points on the left side of the design domain fixed. An input force is applied to the left hand-side of the space, along with an input spring constant value. A reaction force and spring constant are also applied to the right hand side of the space. The objective of the problem is to maximize the work done on the output spring. If the ratio of k_{out} to k_{in} is larger, greater force transfer to the output location is targeted. Conversely, the ratio of k_{out} to k_{in} is smaller, greater displacement of the output location is targeted.

It should be noted that the analysis used in the topology optimization was limited to the assumption of small displacements, and thus linear elastic analysis. This can be achieved by using a small magnitude of the applied load. As load magnitude and resulting motion increases, literature has shown that the assumption of linear analysis at best underestimates motion of the final topology and, at worst, may miss a failure mode (Bruns and Tortorelli, 2001; Buhl et al., 2000). However, the creation of these optimized pieces should still offer a useful point of comparison between 2-phase and 3-phase results, even though the experimental deflection values of each specimen under (relatively) large loads may differ from any predicted theoretical values.

Topology optimization for the design of compliant inverters which may be manufactured with AM is well studied. However, as the next section will show, the general field of topology optimization in AM is incredibly varied, with researchers using different finite element (FE) representations and optimization algorithms according to the context of the particular problem, as well as personal preference.

2.2.3 Topology Optimization in Additive Manufacturing

While little to no work has yet been done regarding the manufacturing of optimized, multi-material compliant mechanisms via AM (to be discussed further in the Section 2.2.3), several researchers have investigated the use of AM as a means of real-

izing topology-optimized parts, including small scale material microstructures (e.g., (Andreassen et al., 2014; Challis et al., 2010, 2012)). The 'free complexity' inherent in the AM process makes it ideal for the realization of final optimized parts. While there are several topology optimization groups looking at manufacturing processes, the following section seeks to elucidate the larger hubs specializing in manufacturing research that have also pursued design optimization.

At Loughborough University, work has been performed to assist in the design of optimized artifacts while specifically considering the necessary manufacturing constraints provided by AM. Brackett and coauthors recently offered an overview of some of the largest perceived opportunities in this sector, including the importance of mesh resolution, support material constraints, and adaptations of the Solid Isotropic Material with Penalization (SIMP) material interpolation for lattice-based and multiple-material structures (Brackett et al., 2011a). On the utilization of multiple-material topology optimization, they specifically mention the abilities of the PolyJet process and offer an example of how a designer could map the various blends onto the densities produced by the SIMP. They also acknowledge challenges, however, such as maintaining a formal sensitivity analysis and the need for experiments to ensure a reasonable mapping scheme, and that the constitutive relations in SIMP and the blended material may not be consistent. Brackett also proposed a dithering optimization method based on stress analysis for the creation of functionally graded lattice structures within a part (Brackett et al., 2011b). Aremu and coauthors in-

vestigated the suitability of Bi-Directional Structural Optimization (BESO) for AM, and extended the BESO strategy to include adaptive meshing around the boundaries (Aremu et al., 2011), similar to topology optimization strategies proposed by (Guest and Smith Genut, 2010a; Maute and Ramm, 1995; Stainko, 2006) for enhancing computational efficiency.

At the Georgia Institute of Technology, emphasis has been placed on the development of cellular structure design, optimization, and analysis techniques for application to AM. Wang and Rosen developed a methodology for the design of conformal cellular truss structures that could easily be translated to AM parts, and later automated the design and synthesis of these structures through a truss sizing optimization and application to mechanism structures (Wang and Rosen, 2006, 2001; Wang et al., 2005). Graf developed a Size Matching and Scaling (SMS) approach, which utilizes a unit cell library consisting of different truss arrangements optimized to support particular loading conditions. He subsequently offers a comparison of the SMS approach against the Particle Swarm Optimization method and least-squares minimization optimization method (Chu et al., 2010; Graf et al., 2009) and found that the SMS method could offer performance comparable to the results of these other two algorithms, while significantly decreasing the computation time due to the non-iterative nature of SMS. Finally, Rosen introduced a formal framework for the concept of Design for Additive Manufacturing, based on the process-structure-property-behavior framework from material science (Chu et al., 2008; Rosen, 2007). He demonstrated

the use and applicability of this framework through the design of a size-optimized lattice structure to support a cover plate.

At the University of Southern California, Chen adapted Rosen's framework to assist in the design of cellular structures that offer specific compliant performance. He developed a CAD tool to design a mesostructure allowing for heterogeneous material properties within an AM printed part, in essence creating functionally graded materials from a single material (Chen and Wang, 2008; Li et al., 2009). Maheshwaraa, Bourell, and Seepersad, at the University of Texas at Austin, used truss ground structure optimization for investigating the use of lattice structures in the creation of deployable skins manufactured via AM (Maheshwaraa et al., 2007).

Obviously the body of work discussed above is incredibly varied. There are researchers investigating the manufacture of optimized single-material structures in AM, researchers who are developing manufacturing rules related to single-material optimization in AM, and researchers who are investigating how multi-material optimization could generally be implemented in AM. However, in the above investigation, there were no examples of authors attempting to develop a process for the optimization and subsequent fabrication and testing of multi-material compliant mechanisms, while also incorporating the manufacturing constraints and advantages of the PolyJet printing process. It is this process that we seek to develop in our work, starting with the initial results presented herein.

2.2.4 Theoretical Representation of Multiple Materials in Topology Optimization

In order to apply topology optimization to the PolyJet process, an appropriate scheme for representing and choosing among the multiple candidate materials decided upon. While some potential schemes have already been touched upon in the review of AM optimization (such as optimality criteria, BESO, and genetic algorithms) there are yet other multi-material representations that might also prove applicable to the realm of PolyJet printing.

In the typical representation outline in Chapter 1, the design domain is discretized into a series of elements or pixels (voxels in 3D) and each element is assigned a pseudo-density, or volume fraction. These pseudo-densities are used to interpolate between two phases of material: solid and void. The SIMP penalization parameter, η will help force the pseudo-densities to 0 or 1. Additionally, by introducing a second pseudo-density term to each pixel, it is possible to further interpolate between three material phases: one stiff, one flexible, and one void (Bendsøe and Sigmund, 1999). This idea may be further extended by introducing an additional pseudo-density variable to each pixel accounting for each additional material phase that is available. This method has been shown to perform reliably, but relies on a large number of design variables, as each additional material introduces additional design variables on the order of the number of pixels in the design space (e.g. four non-zero material options creates four

times as many design variables).

A few have attempted to design multi-material compliant mechanisms. Notably, Saxena tackled the multi-material compliant mechanism problem by discretizing the domain with frame elements and using a genetic algorithm with rounding to assign available material phase values to the frame members (Saxena, 2002, 2005). As discussed, however, stochastic search approaches such as genetic algorithms become intractable for large-scale optimization problems such as continuum-based topology optimization.

2.2.5 Context

The study presented in this chapter demonstrates a start-to-finish process for the realization of optimized, multi-material compliant mechanisms. This represents an important first step in unlocking the design potential of the multi-material PolyJet process. A SIMP and projection-based optimization method (Section 2.3.2) is applied to the design of a compliant force inverter, a well-known compliant mechanism case-study. Results from experimentally testing the printed multi-material optimized structures are provided in Section 2.6. Additionally, a second test problem is presented in section 2.5.2 to demonstrate the flexibility of the method to design for other compliant mechanisms. Concluding remarks are offered in Section 2.7.

2.3 Process for Design and Manufacturing of 3-Phase Compliant Mechanisms

This section discusses the optimization approach that was implemented to design optimized compliant mechanisms. Section 2.3.2 discusses the multivariate SIMP optimization method, and how it is applied to multiple material optimization. In addition, Section 2.3.1 will discuss the logic behind the selection of this approach.

2.3.1 Determination of Compliant Mechanism Design Process Suitable for PolyJet Printing

As stated above, we chose to use a continuum approach to the compliant mechanism design problem. Continuum representation offers the potential for a free-form representation of topology. It is worth noting that a hybrid representation might be able to balance the speed of the discrete representation with the resolution of the continuum method. While such hybrid approaches generally exist in literature, such as a truss-continuum model simultaneously optimized to place steel and concrete materials (Amir and Sigmund, 2013; Gaynor et al., 2013; Yang et al., 2014), there do not appear to be any hybrid representations being used in conjunction with multiple material AM at this time.

The authors have instead chosen to pursue a continuum representation, due in part

to the quality of its resolution as well as the way in which a continuum representation aligns with the PolyJet process's method of printing. When printing, the PolyJet process utilizes a series of multi-colored bitmaps that are sent to the printer. Each bitmap represents a single slice of the printed part, with multiple colors used in each slice to denote the material to be deposited. While the ability does not currently exist, the authors hope to eventually be able to use the image outputs from 2D topology optimization as a direct bitmap slice input to the printer. In this way, translating the topology optimization output to an Standard Tessellation Language (STL) file will become unnecessary and the process of manufacturing optimized multi-material compliant mechanisms will become more streamlined.

It was decided to use a gradient-based optimization algorithm to solve this problem, due to it's ability to handle optimization problems with thousands to millions of design variables while remaining efficient. There have, however, been many people who chose to use a stochastic search optimization algorithm. Stochastic algorithms, such as genetic algorithms and particle-swarm optimization, randomly sample the design space and are thus capable of handling discrete formulations and facilitating escape from low performance local minima. They have been used in a wide range of applications, including manufacturing processes to optimize system design and order policy (Carlo et al., 2012), system identification to obtain model parameters (Deuser et al., 2013; Pang and Kishawy, 2012), identification of manufacturing process parameters (Keshavarz Panahi et al., 2013), assembly system reconfiguration planning

(Bryan et al., 2013), sheet roll forming (Park and Anh, 2012) and folding (Leng et al., 2013), and shape optimization of orienting devices (Hofmann et al., 2013). Stochastic search algorithms, however, can be computationally expensive and may break down in high dimension spaces such as those of continuum topology optimization. Although strategic dimension control algorithms have been proposed for such cases (e.g., (Guest and Smith Genut, 2010b)), gradient-based optimization methods are much better suited to handle the many design variables inherent in a continuum representation. In this preliminary study, the Method of Moving Asymptotes (MMA) will be utilized as the optimizer (Svanberg, 1987).

2.3.2 Optimization Approach 1: Multiphase SIMP Method

Previously, Bendsøe and Sigmund (1999) proposed a multiphase topology optimization method in which three phase solutions were possible. This formulation used two sets of design variables. The first set of design variables ρ_1 are used in determining the optimal topology of the compliant mechanism, while the second set of design variables ρ_2 are used for selecting the material at each location within the topology. The resulting material stiffness of an element is then given as

$$E^e = \rho_1(\phi_1)^\eta \Big[\rho_2(\phi_2)^\eta E_1 + [1 - \rho_2(\phi_2)^\eta] E_2\Big] \tag{2.1}$$

where E_1 and E_2 are Young's modulus of the first and second phases, respectively. As can be seen in Eq. (2.1), the modulus E^e of each element is a function of both ρ (and their corresponding independent design variables ϕ_1 and ϕ_2). If $\phi_1 = 0$, then the element takes on a modulus of 0. If $\phi_1 = 1$ and $\phi_2 = 0$, then $E^e = E_1$, and when $\phi_1 = 1$ and $\phi_2 = 1$, $E^e = E_2$.

Embedded in this formulation is the Heaviside Projection Method (HPM) (Guest et al., 2004). HPM uses independent design variables ϕ that are projected onto the ρ space using regularized Heaviside functions in a manner that enables direct control over the minimum length scale of designed features. This is meant to mimic the AM manufacturing process as material is computationally 'deposited' into the design domain in a circular shape with radius $r_{\min}$, the resolution length scale of the liquid droplets (Guest, 2009b; Guest et al., 2011). Note, however, that the length scale $r_{\min}$ used in the examples is chosen much larger than the smallest achievable droplet so as to design simple structures that may better elucidate the benefits of using multiple materials.

While most work has focused on controlling length scale on solid-void structures, controlling length scale on each material phase in three-phase (or more) topology optimization remains a challenge. Using Eq. (2.1), the designer has control over features sizes but does not have rigorous control on the length scale of the individual material phases within the feature. While rapid phase variation within the member is not possible, prescribed length scale may become violated when ϕ_2 variables located

outside of the member take on non-zero values, allowing thin bands of material to form on the member edges.

As stated previously, the Method of Moving Asymptotes (MMA) is used as the optimizer (Svanberg, 1987), and full algorithmic details of coupling HPM and MMA are available in (Guest et al., 2011). It should also be noted that controlling minimum length scale circumvents the aforementioned numerical instabilities of solution mesh dependence and checkerboard patterns.

2.3.3 Optimization Approach 2: Combinatorial SIMP Method

In this section, we develop an alternative material interpolation scheme to that of Bendsøe. The difference in material distribution control will be apparent in solutions presented in Sections 2.5.1 and 2.5.2.

2.3.3.1 Unique Material Model Development

As stated above, Bendsøe developed a topology optimization material model in which the optimizer chooses both the final topology and the distribution of material phases. It is desired to develop a slightly different material model in order to obtain more control over the material distribution within the final topology. As such, a model was developed by first solving a different problem: obtaining discrete bar sizes

for truss optimization problems. Traditionally, gradient based truss optimization yields solutions with truss members of any number of sizes. However, it is highly desirable to have the final solution pick from only a 'database' of prefabricated sizes, since, when constructing a truss structure, custom size truss member sizes have a cost premium. This problem is fully explained in the appendix (A). The development is quite extensive but the details are necessary to establish a proper background to the proposed multi-material model.

In integer programming, the discrete truss problem has been fully investigated and explained.This new method which utilizes the advantages of continuous design variables, but forces the solutions to preselected discrete values, may be adapted for other problems in which the engineer may need to choose between a number of candidate materials. As will be seen in a later section (Sec. 2.3.3, instead of having a combination of ΔA at each point in space, the algorithm is reformulated to have a ΔE at each point in space. This is more appropriate for the multi-material additive manufacturing method in which different modulus materials may be deposited in the design domain.

2.3.3.2 Material Model Adaptation to Polyjet

Based on the integer programming discrete truss optimization covered in A, a new approach proposed here involves a combination of design variables in a SIMP scheme to produce multi-material topologies. The idea is that each phase contributes to a

total Young's modulus for an element. The base modulus is the modulus of the most compliant phase (typically void), and each phase i has the capability of adding a discrete magnitude ΔE_i of stiffness. For the case of equal increments ΔE in Young's modulus between the phases, this may be written as follows:

$$E = \sum_{i=1}^{n} \rho(\phi)_i^{\eta_i} \Delta E \tag{2.2}$$

where n is the number of dependent design variables ρ per element. To achieve a three phase solution containing voids ($E = 0$), stiff material ($E = E_{\text{stiff}}$), and complaint phase (e.g., $E = 0.5E_{\text{stiff}}$), two elemental design variables per element are required and $\Delta E = 0.5E$stiff. An element is then assigned the stiff phase when $\rho_1 = \rho_2 = 1$, compliant phase when ρ_1 or ρ_2 are equal to 1, and void when $\rho_1 = \rho_2 = 0$. Parameter η_i is the SIMP exponent on design variable i and is needed to drive the design variables to 0 or 1, and ultimately the modulus of an element, to the allowable magnitudes. It is generally good practice to make the η_i slightly offset to prevent sensitivities from being equal during the first iteration.

Again we embed HPM in this formulation, making ϕ_i the independent optimization variables that are projected onto finite element space. An interesting advantage here is that each design variable simultaneously indicates material existence and phase selection. This ultimately provides slightly different length scale control over the phases in the design. Specifically, if stiff phase appears near a member edge, it can be shown that it will achieve a minimum thickness (diameter) of $2r_{\min}$. We

have also observed this on the interior of thick members (of width larger than $2r_{\min}$), although this cannot be mathematically guaranteed. Disadvantages are that the designer does not have control over the minimum length scale of the compliant phase within a member (as before), and at present the algorithm requires the materials to have equal increments in stiffness (ΔE). We note the latter may be quite appropriate for the multi-material Polyjet process.

2.4 Optimization: Compliant mechanism formulations

In the case of the inverter problem, a common benchmark in topology optimization, the goal is to maximize negative displacement (minimize displacement) at an output port under a given load F at an input port. This is expressed mathematically in general as follows:

$$\begin{aligned} \min_{\phi} \quad & \boldsymbol{L}^T \boldsymbol{d} \\ \text{subject to:} \quad & \boldsymbol{K}(\phi)\boldsymbol{d} = \boldsymbol{F} \\ & \sum_{e \in \Omega} \rho^e(\phi) v^e \leq V \\ & 0 \leq \phi^e \leq 1 \quad \forall\, i \in \Omega \end{aligned} \tag{2.3}$$

where $\boldsymbol{d}$ are the nodal displacements, the unit vector $\boldsymbol{L}$ extracts the output port

degree-of-freedom, $\boldsymbol{K}$ is the global stiffness matrix, V is the allowable volume of material, v^e is the elemental volume, and $\boldsymbol{\phi}$ is the independent design variable vector, described below. All examples were solved using a uniform distribution of material as the initial guess.

2.4.1 Robust Topology Optimization Formulation

When using topology optimization to design compliant mechanisms it is well-known that solutions may contain one-node hinges, a situation where two solid elements are connected only at a corner node. One node hinges allow for lumped compliance and the performance of such elements is overestimated with low-order finite elements. Obviously, if a one-node hinge were printed, it would instantaneously fail due to the stress concentration at a point. While projection methods enable control of a minimum feature size, it was discussed in the original work (Guest et al., 2004) that design variables could theoretically deposit two tangent circles, which would manifest in a one-node hinge. A number of researchers have specifically tackled the one-node hinge issue in the context of the compliant inverter. Sigmund (2009), for example, simultaneously optimized an eroded and dilated version of the topology to mimic over- and under-etching, respectively. This led to a min-max formulation, with the idea that over-etching would lead to a disconnected structure, and thus zero performance, if one-node hinges were present. While the method successfully eliminates one-node hinges from designs, an actual 'blue-print' design, which is passed to the

manufacturer, is not clearly identified. A number of other authors have tackled the issue by using Monte Carlo simulation to represent manufacturing uncertainties in the context of projection schemes (Jansen et al., 2013; Schevenels et al., 2011) and level set methods (Luo et al., 2008).

This chapter adopts the same basic idea as Sigmund, employing a min-max formulation that simultaneously optimizes a larger projection and smaller projection of the same design variables. For this chapter, however, we consider a minimum length scale $r_{\min}$ set by the user to represent the expected radius of the droplet, and then vary that droplet size by directly varying the radius r used in projection. This introduces two additional length scales, defined as:

$$\begin{aligned} r_{\text{minlarge}} &= r_{\min} + \Delta r \\ r_{\text{minsmall}} &= r_{\min} - \Delta r \end{aligned} \tag{2.4}$$

where Δr is the variation in length scale, and is currently set equal to the height of a standard element within the domain. However, with more knowledge of the variability in droplet size for a particular additive manufacturing method, the Δr may truly represent the variability in the printing process. The resulting min-max compliant mechanism optimization formulation then takes on the form:

$$
\begin{aligned}
\min_{\boldsymbol{\phi}} \quad & \max\left\{\boldsymbol{L}^T\boldsymbol{d}_{(r_{minsmall})}, \boldsymbol{L}^T\boldsymbol{d}_{(r_{minlarge})}\right\} \\
\text{subject to:} \quad & \boldsymbol{K}(\rho(\phi)_{(r_{minsmall})})\boldsymbol{d}_{(r_{minsmall})} = \boldsymbol{F} \\
& \boldsymbol{K}(\rho(\phi)_{(r_{minlarge})})\boldsymbol{d}_{(r_{minlarge})} = \boldsymbol{F} \\
& \sum_{e\in\Omega} \rho(\phi)^e_{r_{min}} v^e \leq V \\
& 0 \leq \phi_i \leq 1 \quad \forall\, i \in \Omega
\end{aligned}
\tag{2.5}
$$

While the formulation in Eq. (2.5) is nearly identical to Sigmund (2009), there is a subtle difference in achieving the geometric perturbation: Sigmund's dilate and erode variations actually simulate over-depositing and over-etching, which may represent different manufacturing processes and lead to different concavities of the material interface, while Eq. (2.5) simulates only the deposition process and the idea of an inkjet droplet being larger and smaller than anticipated. Though subtle, we feel the latter more accurately reflects the AM process. A continuation scheme on the β Heaviside parameter is used to achieve a quality solution. The β for r_{minlarge} is started at 0 and increased by 1 each continuation step. Alternatively, the β for the r_{minsmall} is fixed at a magnitude of 2. The results found in this chapter performed 11 continuation steps with 60 MMA optimization iterations for each continuation step. As our focus is on the multi-material aspect of these designs, the finer details of this robust topology optimization formulation and algorithm tuning are not explored here.

2.5 Compliant Mechanism Topology-Optimized Solutions

The robust compliant mechanism topology optimization formulation (Eq. 2.5) is tested on both the aforementioned compliant inverter design problem and the micro gripper problem (Sec. 2.5.2).

2.5.1 Force Inverter Topology-Optimized Solutions

The compliant inverter is first solved using only two phases, solid and void, as in traditional topology optimization. Additionally, a non-robust solution is provided to demonstrate the one-node hinge issue (Fig. 2.4). The robust formulation is used with a length scale variation of 0.9 units to ensure the existence of reasonable hinges in the final topology. This, and all following examples, use a 30% total allowable volume fraction, a 240 x 120 finite element mesh (utilizing symmetry), and begin with a uniform distribution of material as the initial guess.

The resulting two-phase solution is shown in Fig. 2.5. The topology is near binary (solid-void), does not exhibit any one-node hinges as those seen in Fig. 2.4, and satisfies the length scale prescribed by the designer.

We now examine the three-phase solutions, with one material phase being void, the second being compliant, and the third being stiff, where the stiffness ratio of stiff to compliant material is 2:1. Figure 2.6 displays the solution using the combinatorial

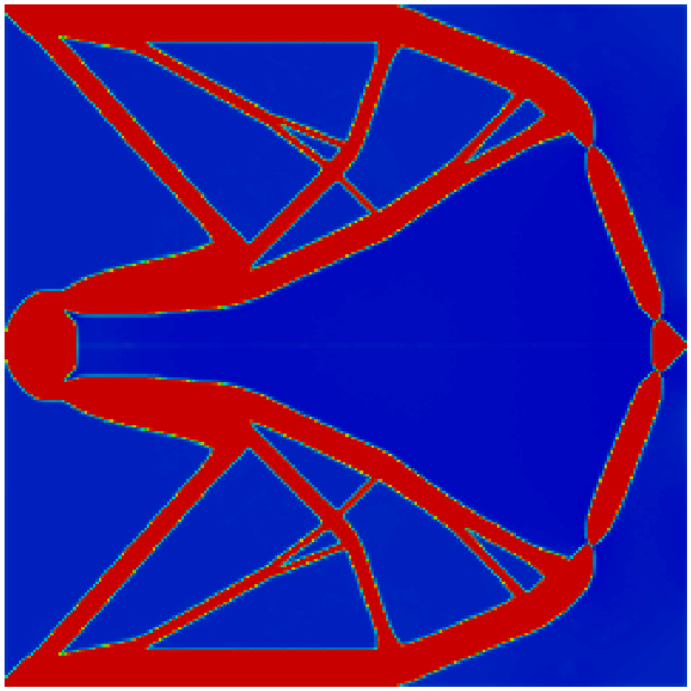

Figure 2.4: 2-phase (solid-void) inverter result found using non-robust topology optimization approach. 240 element by 120 element mesh with $r_{\min} = 1.6$ elements widths.

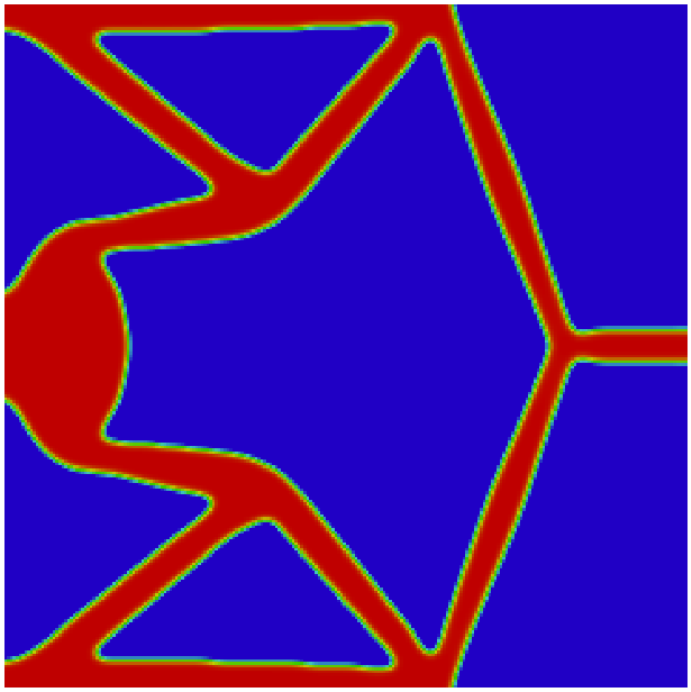

Figure 2.5: 2-phase (solid-void) inverter result found using the robust SIMP approach.

SIMP scheme. The result aligns with intuition: the algorithm places the stiff phase in the bar-like members to enable efficient force transfer and places the compliant phase in a hinge-like region. Note that all features have a length scale of least $2r_{\min}$, including the hinge-feature, meaning length scale is satisfied and one-node hinges are eliminated by using the robust formulation. Notice that the solution has compliant hinges at both ends of the inclined members (near the bottom and top domain boundaries).

The compliant inverter is also solved using the Bendsøe and Sigmund multiphase approach with the robust formulation Eq. 2.5 to prevent one-node hinges. As can be seen in Fig. 2.7, the phase distribution is more complex looking than that of

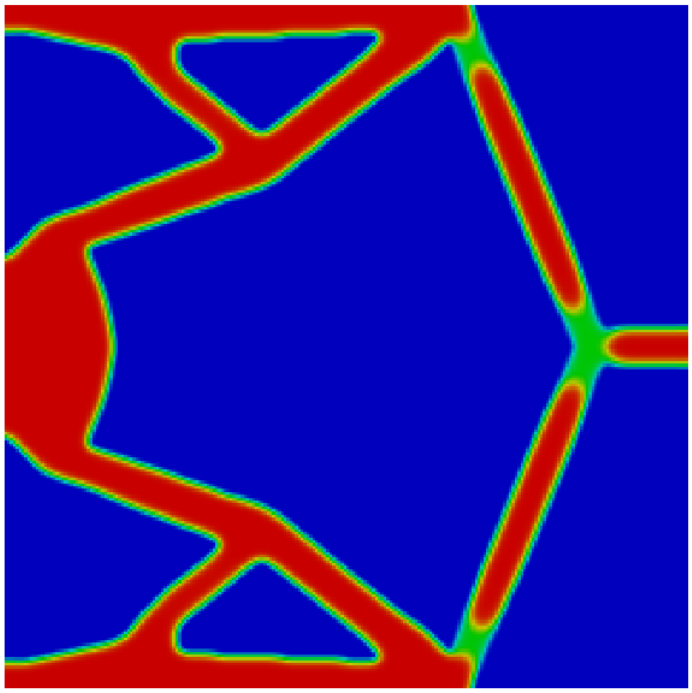

Figure 2.6: 3-phase inverter result found using the robust combinatorial SIMP approach (2:1 stiffness ratios).

the multivariate SIMP approach seen in Fig. 2.6. This is due to the fact that the topology (ρ_1) and material (ρ_2) projections, are performed separately in this approach, and are then combined to generate topology. This leads to the tapering of stiff material in the load transfer members near the output port and, although the entire structural member satisfies length scale of $2r_{\min}$, the individual phases do not. This is a subtle, but important difference between the two multi-material approaches. As in the combinatorial SIMP approach, the stiff material is concentrated in the load-carrying members, while the compliant material is concentrated in the hinge regions. This solution also uses a small volume of complaint material to create a tapered, hinge-like feature near the applied load.

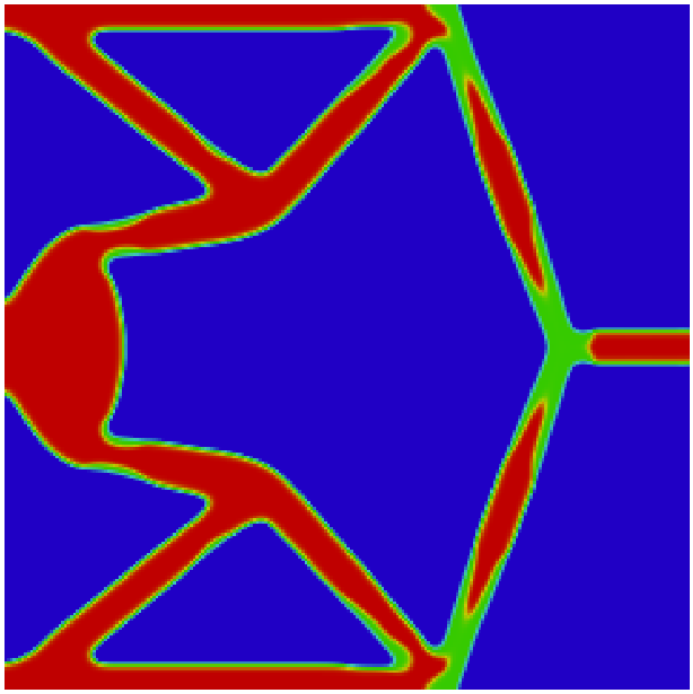

Figure 2.7: 3-phase inverter result found using the robust, multiphase SIMP approach.

2.5.2 Micro Gripper

To further exhibit the capabilities of this new compliant mechanism design method, the presented algorithm is tested on the micro-gripper test problem. The design is similar to that of the force inverter in that the domain is fixed on the bottom and top of the lefthand side while a force is applied to the midpoint on the same side. Now, instead of targeting a force or displacement inversion, a more typical displacement is targeted. On the righthand side of the domain two solid sections are specified as the interaction surface of the gripping mechanism. The maximum displacement, d_{out}, is targeted at the output port locations seen in the following problem definition (Eq. 2.6 and Fig. 2.8):

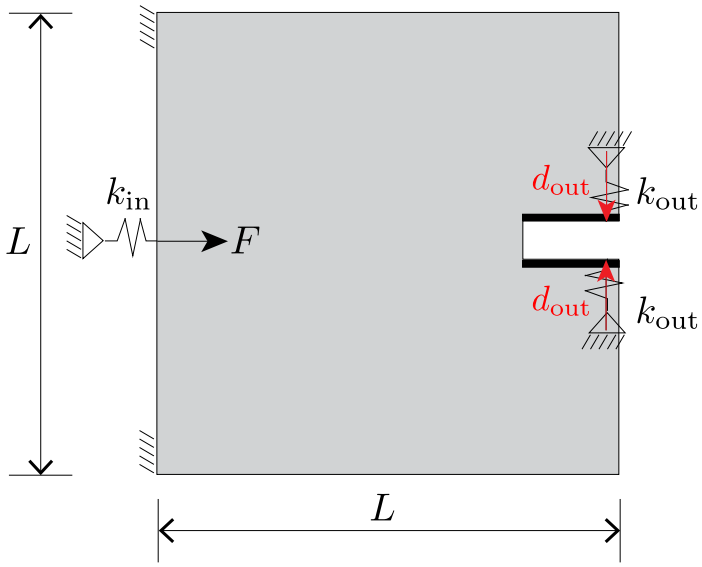

Figure 2.8: Micro gripper problem definition

$$
\begin{aligned}
\min_{\boldsymbol{\phi}} \quad & \max\left\{\boldsymbol{L}^T\boldsymbol{d}_{\text{out}(r_{minsmall})}, \boldsymbol{L}^T\boldsymbol{d}_{\text{out}(r_{minlarge})}\right\} \\
\text{subject to:} \quad & \boldsymbol{K}(\rho(\phi)_{(r_{minsmall})})\boldsymbol{d}_{\text{out}(r_{minsmall})} = \boldsymbol{F} \\
& \boldsymbol{K}(\rho(\phi)_{(r_{minlarge})})\boldsymbol{d}_{\text{out}(r_{minlarge})} = \boldsymbol{F} \\
& \sum_{e\in\Omega} \rho(\phi)^e_{r_{min}} v^e \leq V \\
& 0 \leq \phi_i \leq 1 \quad \forall\, i \in \Omega
\end{aligned}
\tag{2.6}
$$

Solutions are presented for the micro-gripper for 2-phase (Fig. 2.9) along with two solutions for the three phase including the Combinatorial SIMP solution seen in Fig. 2.10 and the multiphase SIMP approach seen in Fig. 2.9. All three of the micro-gripper solutions use the robust topology optimization formulation seen in Eq. 2.5 with a 30% volume fraction.

Interestingly the two 3-phase solutions do not have the same general shape. It

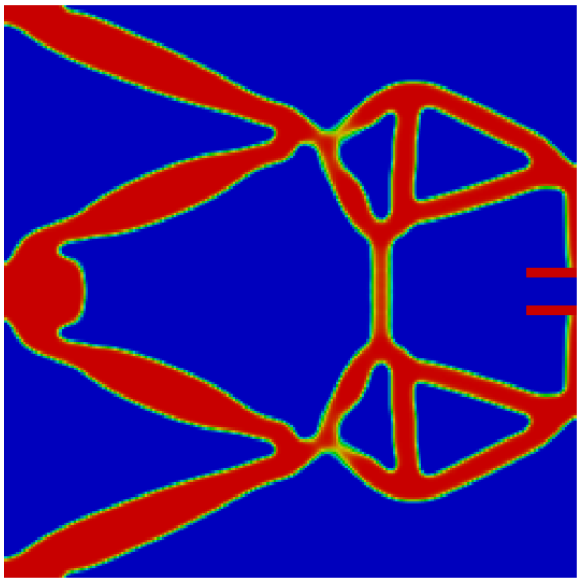

Figure 2.9: 2-phase (solid-void) inverter result found using the robust SIMP approach.

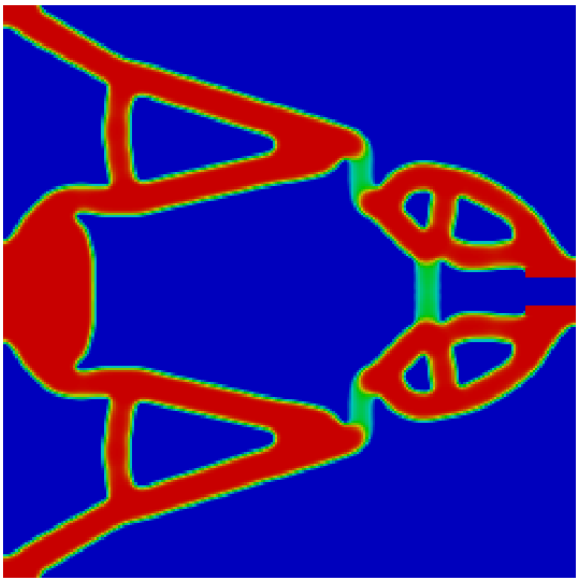

Figure 2.10: 3-phase inverter result found using the robust Combinatorial SIMP approach.

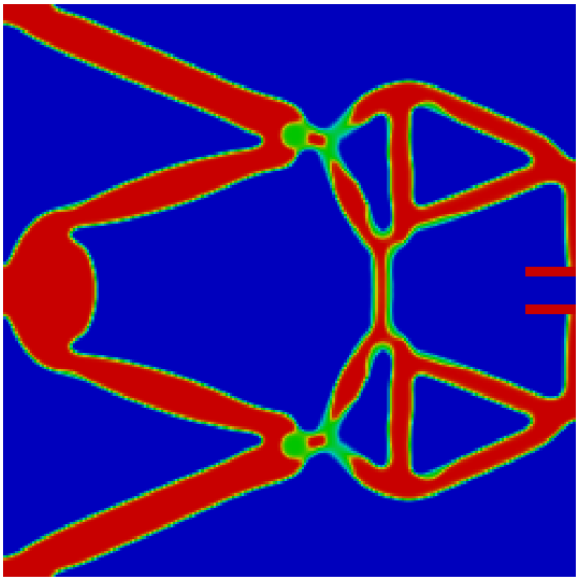

Figure 2.11: 3-phase inverter result found using the robust, multiphase SIMP approach.

is likely that the solutions are due to the relatively high non-linearity of the design problem are both in fairly good local minima. However, the multiphase SIMP formulation generally allows for more complex final solutions, so it may be that the altered topologies are dictated by the material models.

2.6 Mechanical Testing

Both the 2-phase and 3-phase inverters were printed on an Objet Connex 350. The stiff material was VeroWhite+ and the flexible material was RGD8530. Each inverter was printed to fill a 12 x 12 cm bounding box, with a thickness of 3.175 mm. An additional structure was added to each compliant mechanism in order to provide a location for the necessary force to be applied, as well as to ensure a cantilevered

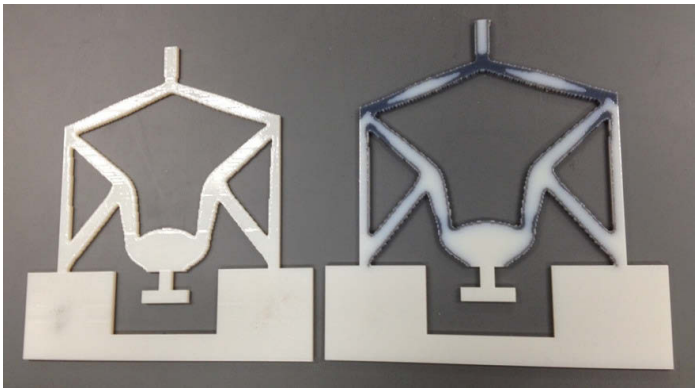

Figure 2.12: 3-phase inverter result found using the robust, multiphase SIMP approach.

fixation at the appropriate point on the structure. The final printed specimens can be seen in Fig. 2.12.

Each inverter was actuated by applying a 9.65 kg load at the "T" shaped attachment at the bottom of mechanism. The output tip location was marked before and after application of the load. The resulting mechanism motion is shown in Fig. 2.13. The 2-phase inverter tip deflected 1.33 mm while the 3-phase inverters deflected 1.95 mm and 2.45 mm for the combinatorial SIMP and multiphase SIMP approach respectively. Notably, this is a performance improvement of 84% for the multiphase SIMP case and an improvement of 46% for the combinatorial SIMP approach. Although we were expecting the multiphase SIMP approach to outperform the combinatorial, as it is less restrictive on the length scale of the individual material phases within a member, the actual magnitude of difference is more than expected, and confirms the 'details' of the design are important. This difference could also be amplified by the fact that the experimental set-up did not exactly match the assumption used in the

optimization, as there were no springs applied to the output and input ports. Looking at the multiphase SIMP (Fig. 2.7) and combinatorial SIMP (Fig. 2.6) solutions, we see a thin compliant, border around all stiff regions. This border is likely not optimal, but instead an artifact of using small values for the β Heaviside parameter associated with the projection scheme. This fading effect can be mitigated by simply using larger values of β (see (Guest et al., 2011) for full discussion), though this was not done here.

To demonstrate the ultimate potential of the PolyJet process's array of materials, an additional optimization was performed using a stiffness ratio of 20:1 between the two non-void candidate materials. This ratio is intended to more closely resemble the stiffness difference between the stiff VeroWhite+ material and TangoBlack+, the most elastomeric material offered by the Objet process. The optimized topology is shown in Fig. 2.14 using the robust, multiphase SIMP approach.

The TangoBlack+ and VeroWhite+ inverter achieved a deflection of 11.58 mm with only 2.75 kg of applied load, as shown in Fig. 2.15. This is almost nine times larger in displacement and more than three times less in load, or an improvement in efficiency of over 30. It is important to note that modulus of elasticity information for TangoBlack+ has yet to be published by the manufacturer or by independent researchers, and so the performance of the printed specimen has the potential to differ significantly from the performance predicted by the optimization algorithm (since the stiffness ratio is purely an estimation). However, it nevertheless demonstrates the

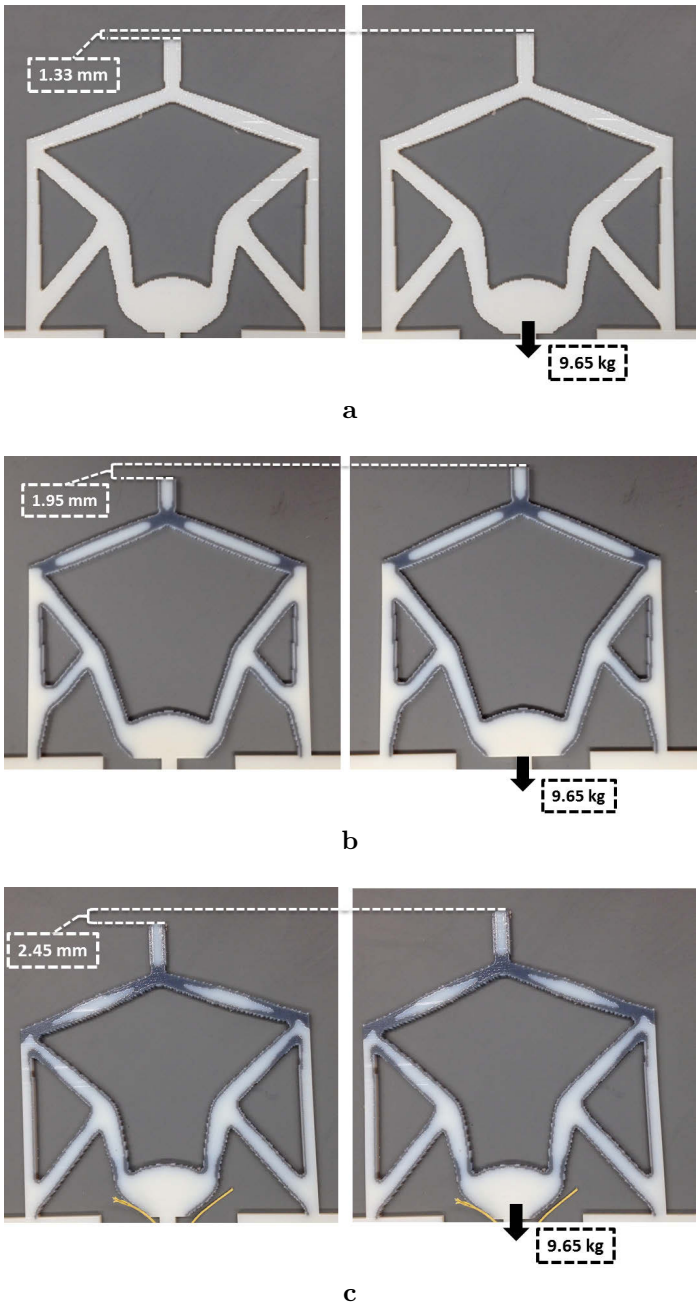

Figure 2.13: Deflection of a) 2-phase inverter (Fig. 2.5), b) 3-phase combinatorial SIMP inverter (Fig. 2.6), and (c) 3-phase multiphase SIMP inverter (Fig. 2.7) (all under 9.65 kg applied load)

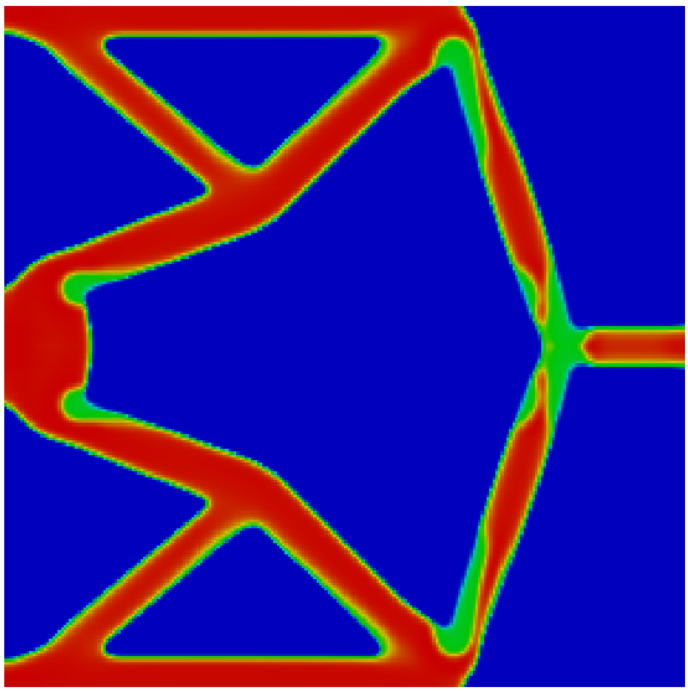

Figure 2.14: 3-phase inverter topology found using the robust, multiphase SIMP approach (20:1 stiffness ratio).

dramatic displacement improvements that might be achieved when using the most elastomeric material for the PolyJet process.

It is also interesting to note the double curvature present in the deformation seen in Fig. 2.15. This is forced through the robust topology optimization method. In the process of eliminating the one-node hinge design normally found for compliant inverter domains, the algorithm produces a structure with distributed compliance. While the lumped compliance present in the solution of a non-robust formulation will have better theoretical performance than the distributed compliance of the robust solution, the actual lumped compliance inverter would fail instantly due to the stress concentration at the one node hinge. Furthermore, achieving distributed compliance

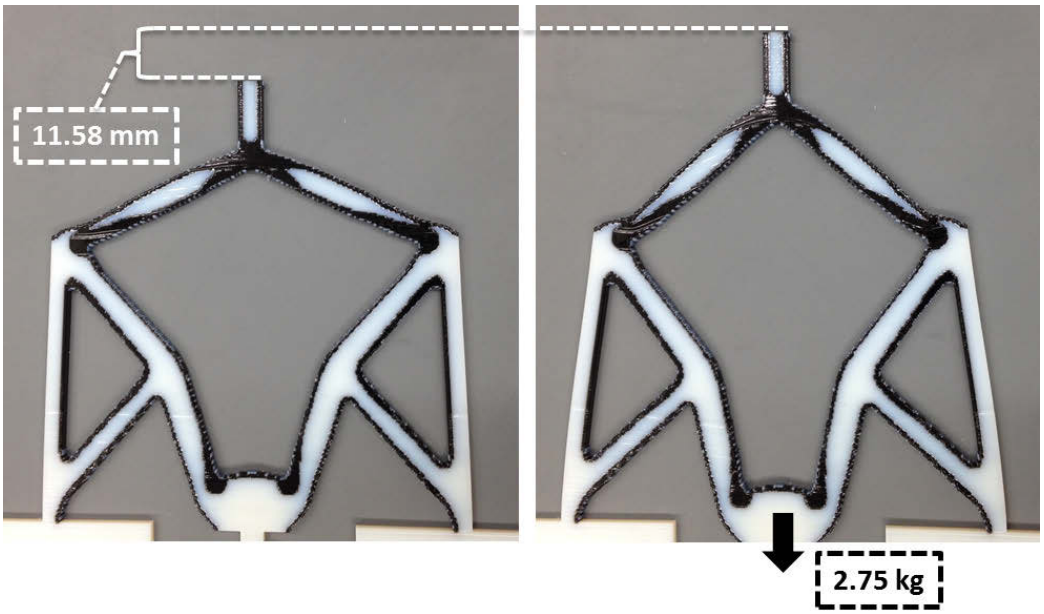

Figure 2.15: Deflection of 3-phase inverter with TangoBlack+ material (under 2.75 kg of applied load).

is fundamental to the original assumption of compliant mechanisms - compliance through material deformation of the structure.

2.7 Conclusions and Recommendations for Future Work

In this chapter, the authors have presented a preliminary study into the development of a start-to-finish process for the design and manufacture of optimized, multi-material compliant mechanisms. The previous literature was reviewed in order to determine an appropriate compliant mechanism design and optimization approach, taking care to consider the unique opportunities afforded by multi-material PolyJet

printing. A robust topology optimization algorithm, modified from Sigmund (2009), was used in combination with a combinatorial SIMP approach and multiphase SIMP approach to design manufacturable, multi-material topologies. Experimental results of the compliant force inverter problem show that the addition of a second non-zero candidate material with stiffness of approximately one-half the base phase increases the deflection (and efficiency) of the compliant inverter by as much as 84%, and by nearly a factor of 30 when the second non-zero phase is TangoBlack+.

From a manufacturing point of view, future work will first focus on independently quantifying the material properties of all the PolyJet materials (with a focus on TangoBlack+) in order to provide a more accurate comparison between the numerical and experimental results. Second, additional candidate materials will be introduced into the optimization routine to create optimized inverters with more material phases. The effect of smoothing the boundaries of each material phase, so as to remove any undesirable stress concentrations that may be present because of the pixelated nature of the final printed specimen, will also be examined. Finally, efforts will be placed on quantifying the printing limitations of the PolyJet process, so that manufacturing limitations might be included in the topology optimization algorithm.

From a topology optimization point of view, it is desired to extend the combinatorial SIMP approach such that the formulation works for non-uniform ΔE. Also, work must be done to develop better continuation methods such that fewer continuation steps are necessary - currently the algorithm must take many such steps, which results

in high computational cost. Additionally, a more physically based method should be developed for the over and under deposition of material. This should be based on the actual statistics of the manufacturing process. However, it should be noted that the current robust topology optimization scheme works extremely well.

Chapter 3

Topology Optimization for Additive Manufacturing: Considering Maximum Overhang Constraints

3.1 Introduction

Additive manufacturing, while seemingly a free-form manufacturing technique, does have a few design limitations. These include the exclusion of internal voids and the need for sacrificial support material in many situations. With respect to the internal voids: they cannot be manufactured since the support material in the voids

must be dissolved away in the case of Fused Deposition Modeling (FDM) (FDM, 2014) and the powder must be able to be removed in the case of Selective Laser Melting (SLM). When enclosed in a void, the material simply cannot be removed. This chapter will focus on designing AM components to eliminate the need for support material. Both polymer based processes such as FDM and powder metal based processes such as SLM require support material in order to manufacture certain parts. In the case of FDM, there is often a soluble support material which can easily be removed in a post-print liquid bath. As for metal support material, the process is a bit more complicated, as the support metal must be chipped or ground off the part after the printing process. Often if this material is in an internal location of the part, it may be difficult, if not impossible to remove, therefore not allowing for the expected further weight reduction from removal of sacrificial material.

3.1.1 Selective Laser Melting (SLM)

Metal support material is essential for many reasons identified by Hussein et al. (2013). These include ease of part removal, anchorage to platform during build process, preventing the toppling of thin-walled sections during the powder wiper process, and preventing the curling and distortion from melting and solidifying process. Vandenbroucke and Kruth (2007) goes into depth on the curling and distortion topic. Mercelis and Kruth (2006) details the consequences of residual stresses due to the heating and cooling phenomenon, particularly pointing to issues of warpage and cracks

.

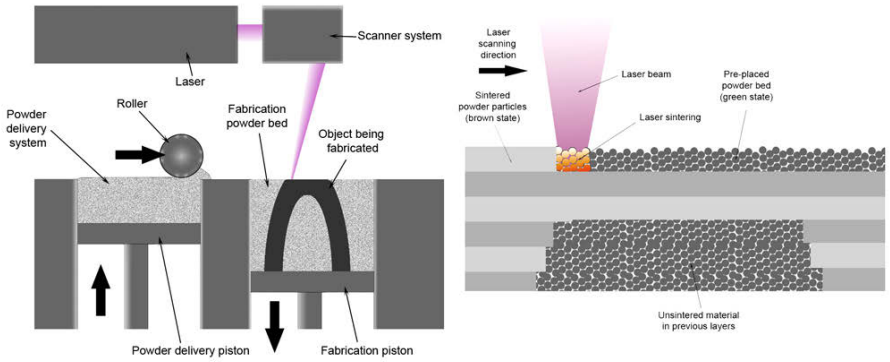

Figure 3.1: Selective Laser Melting Schematic.

Taking into consideration the warpage, toppling, cracking and other such issues, several researchers have identified the maximum printable overhang angle at which a part may be printed without requiring sacrificial support material. Notably, Thomas identified 45° as the typical maximum achievable overhang angle (Thomas, 2009) for SLM methods. Xu et al. (2012) identified the issue in bioprinting applications, where going past the max angle resulted in failure due to moment imbalance and droplet impact-induced crash, and proposed a scaffold free printing process which limited the overhang angle. Recently, Brackett et al. (2011a) identified the overhang problem and suggested using topology optimization with a heuristic penalization scheme imposed to make angles greater than the maximum allowable very expensive (Brackett et al., 2011a). It should be noted that the proposed algorithm was not implemented, so the success is untested. Alternatively, Hussein et al. proposed using low volume lattices as support material in order to reduce the volume of material used in the print process

(Hussein et al., 2013). Others have also suggested strategies to minimize and eliminate support material (Cloots et al., 2013; Mumtaz et al., 2011).

3.1.2 Geometry control in topology optimization

The objective is to develop a topology optimization algorithm that yields solutions which do not violate the maximum overhang angle constraint. Obviously, when the maximum overhang angle constraint is imposed, the compliance values will be as good or worse than those of typical minimum compliance topology optimization (almost always worse). As far as can be seen, no authors have successfully tackled this problem. As stated above, Brackett suggested a penalty function method, but never produced results with the proposed scheme. There has, however, been work in the area of geometry control. To date, geometry control in topology optimization is primarily limited to minimum feature size (minimum lengthscale), however there have been several attempts at maximum length scale (Carstensen and Guest, 2014; Guest, 2009a). Additionally, Guest and Zhu optimized for topologies manufacturable by a milling process (Guest and Zhu, 2012). Others have looked at discrete object placement in topologies (Guest, 2011; Ha and Guest, 2014). Gaynor et. al optimized considering the capabilities of a multi-material 3D printer to produce multi-material compliant mechanisms (Gaynor et al., 2014).

3.2 Optimization Formulation

As previously stated, within the realm of topology optimization, the minimum compliance (maximum stiffness) optimization problem is the most common. The component stiffness is a function of the material distribution within a design domain. Each design domain is discritized into a number of finite elements and each element density, ρ, is chosen to be either a void ($\rho = 0$) or solid material ($\rho = 1$). To allow the use of gradient based optimizers, the binary 0/1 density is relaxed to allow intermediate densities to vary from 0 to 1. While the ρ are allowed to continuously vary between 0 and 1, the end goal is still to drive to a binary 0/1 solution. This is usually achieved though the SIMP penalization (Bendsøe, 1989; Rozvany et al., 1992). In this scheme the problem remains continuous, however intermediate densities are penalized with an exponent therefore deeming them as artificially inefficient and driving towards a 0/1 solution. This chapter uses an alternate to the SIMP penalization: the RAMP interpolation scheme (Stolpe and Svanberg, 2001). Switching to RAMP is seen to improve convergence as it has non-zero sensitivities when design variables equal zero.

The minimum compliance (maximum stiffness) optimization formulation takes on the following form, seen in Eq. (3.1).

$$\begin{aligned} \min_{\boldsymbol{\psi}} \quad & f(\boldsymbol{\psi}) = \boldsymbol{F}^T \boldsymbol{d} \\ \text{subject to:} \quad & \boldsymbol{K}(\boldsymbol{\psi})\boldsymbol{d} = \boldsymbol{F} \\ & \sum_{e \in 1} \rho(\boldsymbol{\psi})^e v^e \leq V \\ & 0 \leq \psi^e \leq \psi^e_{\max} = 1 \quad \forall\, e \in \Omega \end{aligned} \tag{3.1}$$

where $\boldsymbol{\psi}$ is the vector of nodal design variables, v^e is the elemental volume, V is the total allowable volume, and Ω is the design domain.

Here, there is only one explicit constraint, the volume constraint. The minimum length scale and overhang constraint are imposed through projection routines. Essentially, the variables are passed through a continuous projection function that imposes a constraint through its non-linearity. By imposing the constraints through a projection instead of an explicit constraint, the solution to the defined optimization problem automatically satisfies the desired constraints. Alternatively, the overhang constraint could be imposed as a penalty function. As mentioned before, this was proposed by(Brackett et al., 2011a), in which he proposed a heuristic penalization scheme on overhangs which violate the maximum allowable angle. Yet another potential way – and likely better way – to impose the overhang constraint is through modeling the actual printing process and subsequently limiting the curling or deformation. While it is desirable to do this, the authors are still formulating potential optimization schemes to incorporate the physical phenomena of the printing process into the optimization formulation.

3.2.1 Maximum Overhang Control

As stated above, the engineer would like to eliminate the need for sacrificial support material during the additive manufacturing build process. By stipulating that the built part must not possess an overhang angle greater than the maximum observed achievable overhang, the need for support material is completely eliminated, thus ensuring that all material used is for an efficient structural purpose. By producing these new solutions, post processing costs can be cut significantly by eliminating the need to machine out the support material post build - in the case of SLM, support material may not be accessible for a post build removal process, therefore adding unnecessary weight to the structure. According to work done by Thomas (2009), the usual maximum achievable overhang for SLM printed parts is approximately 45 degrees. It is therefore the focus of this chapter to develop an algorithm to design AM parts to have a maximum overhang of 45 degrees. However, while 45° may be the "rule of thumb," the following framework is general enough to optimize for a number of angles. Figure 3.2 illustrates different allowable overhang angles, including allowable overhang angles of 26°, 45°, and 63° in Fig. 3.2a, Fig. 3.2b, and Fig. 3.2b, respectively. The blue region indicates a feature already printed, while the green region indicates the maximum printable overhang angle without requiring sacrificial support material in the build process.

As in the case of imposing the minimum lengthscale constraint, the maximum overhang constraint is imposed through a projection of design variables to another

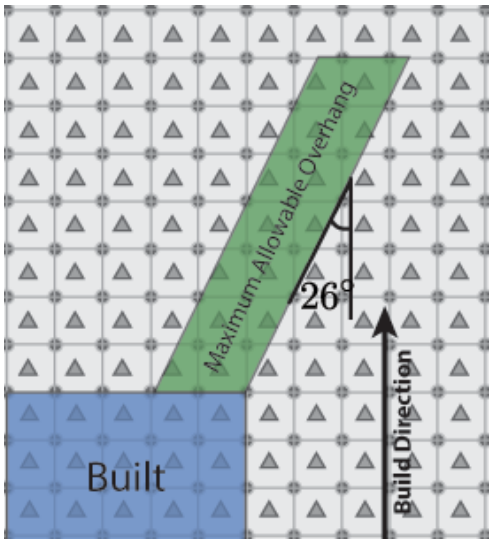

a 26 degrees

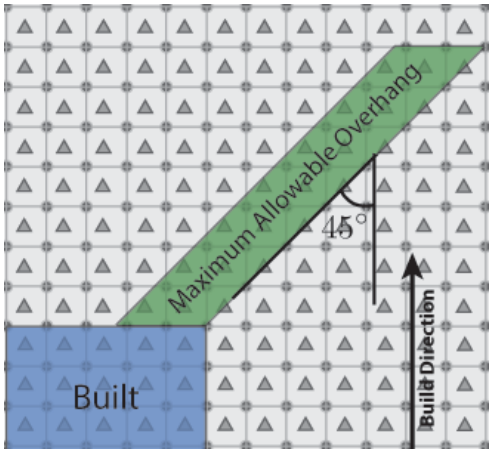

b 45 degrees

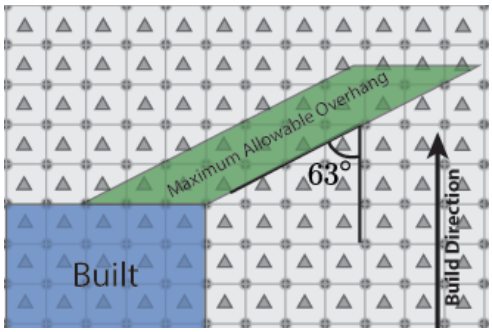

c 63 degrees

Figure 3.2: Overhang constraints: Allowable overhang angles from elemental (physical) perspective. The blue region is imagined to be built already while the green region indicates the maximum angle at which features may be created without requiring support material.

set of variables. Therefore, instead of the usual $\boldsymbol{\phi} \rightarrow \boldsymbol{\rho}$, we now have a $\boldsymbol{\psi} \rightarrow \boldsymbol{\phi} \rightarrow \boldsymbol{\rho}$, where the maximum overhang constraint is imposed in the projection of $\boldsymbol{\psi}$ to $\boldsymbol{\phi}$ and the minimum length scale is imposed, as usual, in the projection of $\boldsymbol{\phi}$ to the physical space, $\boldsymbol{\rho}$.

In the usual minimum compliance with HPM for lengthscale control, the design variables are $\boldsymbol{\phi}$. It is important to note that the design variables are now $\boldsymbol{\psi}$, and not the usual $\boldsymbol{\phi}$. The design variables, $\boldsymbol{\psi}$, first have to be projected to $\boldsymbol{\phi}$ before the $\boldsymbol{\phi}$ can be projected to form the physical space $\boldsymbol{\rho}$. At each point, the ϕ must check whether its existence is "allowed." If the ϕ is adequately supported, it is allowed to exist. Conversely, if it is not adequately supported, it is not allowed to exist. This strict rule is achieved through a multiplication scheme in which the local design variable, ψ is multiplied by an average of the below supporting ϕ passed through a thresholding Heaviside filter to obtain ϕ_S. This is seen in Eq. (3.2). In this scheme, the $\boldsymbol{\psi}$ turn into $\boldsymbol{\phi}$ in a looping scheme starting from the first row on the build place and moving up row by row.

$$\phi^i = \psi^i \phi_S^i \tag{3.2}$$

The following table (Table 3.2.1) helps clarify how this rule works for all of the possible combinations of ψ and ϕ_S. As can be seen, ϕ will only exist when it is supported ($\phi_S = 1$) and the local design variable (ψ) indicates the desire to project material at this location in the design domain ($\psi = 1$). In this case $\phi = \psi\phi_S = 1 * 1 =$

1. All other cases will result in no projected material.

ψ	ϕ_S	ϕ
0	0	0
0	1	0
1	0	0
1	1	1

To determine the ϕ_S for each ψ, the algorithm scans below each ψ location at an angle of $\pm$ the maximum achievable overhang. This is seen in Figs. 3.3. Here, there are three different overhang angles. It is noted that there are discrete jumps in the allowable overhang angle due to the discrete location of and number of nodes within the wedges. However, with an adequate number of ϕ within the within the $1.5r_{\min}$ wedge, a great number of maximum overhang angles can be achieved. It should also be noted that the $1.5r_{\min}$ is used as a general rule of thumb, however any value less than $2r_{\min}$ will work in this framework.

To determine whether $\phi_S = 1$ (indicating it is fully supporting the above ψ), the minimally fully supported condition must be defined. This occurs when the ϕ along one of the two straight edges of the wedge all equal 1. When these $\phi = 1$, they will project material to create a feature exhibiting the maximum allowable angle. For example, for the 45° case in Fig. 3.3b, the maximum overhang case would be for material projected along either of the two angles sides. A side has four ϕ while the entire "wedge" has 38 ϕ. Therefore, in order for the green ψ to be supported, the

average of the below ϕ must be at least $\frac{4}{38} = 0.105$. This simple calculation is shown in Equation 3.3. We will call this the threshold support value, T.

$$T = \phi_{\text{edge}}/\phi_{\text{wedge}} \tag{3.3}$$

To enforce that a certain fraction indicates full support, the average of the ϕ in the wedge are passed through a thresholding Heaviside function such that any fraction above the calculated threshold will be projected to around one, indicating full support, and any fraction below will be projected to around zero, indicating an unsupported case. The thresholding Heaviside function, borrowed from Jansen's robust topology optimization paper (Jansen et al., 2013), serves as a way of mapping the average of the supporting ϕ to a variable ϕ_S. The averaging operator is designated as μ_{av} and is simply the arithmetic mean of the supporting ϕ. This average is mapped to ϕ_S through Eq. (3.4):

$$\phi_{\text{S}} = H_T(\phi_{\text{in support wedge}}) = \frac{\tanh(\beta_2 T) + \tanh(\beta_2(\mu_{\text{av}}(\phi_{\text{in support wedge}}) - T))}{\tanh(\beta_2 T) + \tanh(\beta_2(1-T))} \tag{3.4}$$

where β_2 is the Heaviside exponent and T is the threshold value. As β_2 approaches infinity, the smooth Heaviside approximation approaches the true discontinuous Heaviside function. It is clearly seen in the plot when ϕ_S will be a "supporting" or "unsupporting" case. When the average of supporting ϕ is below the threshold, then

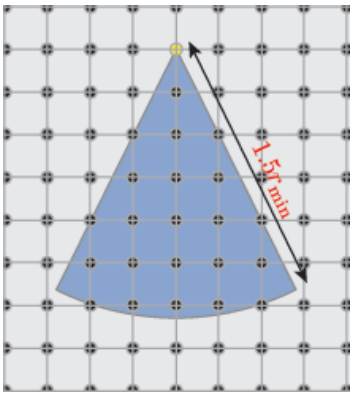

a 26 degrees

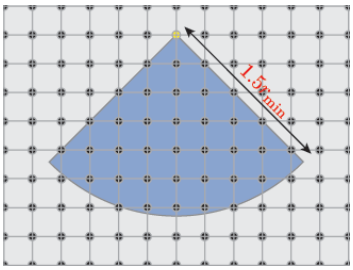

b 45 degrees

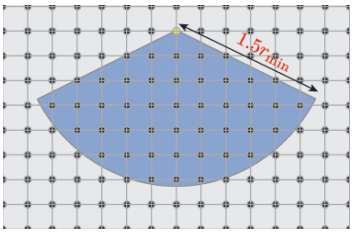

c 63 degrees

Figure 3.3: Overhang constraint: scanning range below ϕ for various overhang angles

$\phi_S \approx 0$. Conversely, when the average of supporting ϕ is above the threshold, then $\phi_S \approx 1$, allowing the ϕ above to equal 1. The thresholding Heaviside function is seen in Fig. 3.4.

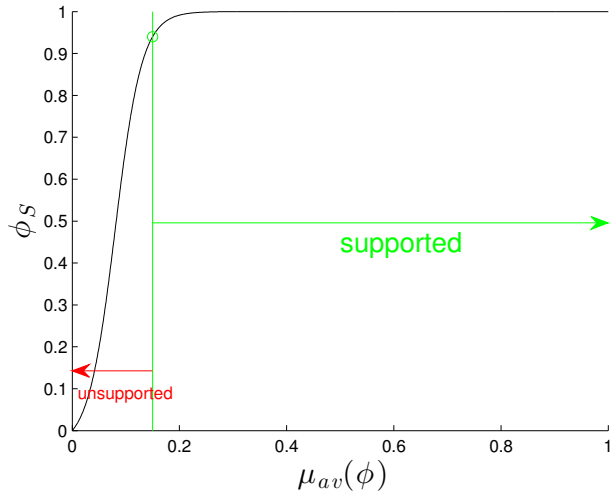

Figure 3.4: Thresholding Heaviside with threshold, T = 0.15.

3.2.2 Derivatives and Implementation

While the optimization formulation is now more complicated looking than the typical minimum compliance with HPM for lengthscale control, it still possesses a differentiable objective and constraint function. This problem is implemented using the gradient based Method of Moving Asymptotes (MMA) optimizer (Svanberg, 1987). Many other gradient based optimization methods may work fine, however MMA is the established industry standard.

3.2.2.1 Derivatives

As in the case of minimum compliance topology optimization with only the Heaviside projection method, the derivatives are straightforward. The usual derivatives when using HPM are seen in Eq. (3.5), where the derivative are a simple differentiation of the objective function, f with respect to ϕ.

$$\begin{aligned}\frac{\partial f}{\partial \phi} &= \frac{\partial f}{\partial \rho}\frac{\partial \rho}{\partial \phi} \\ &= \frac{\partial f}{\partial \rho}\left(\beta e^{-\beta \mu^e(\phi)} + e^{-\beta}\right)\frac{\partial \mu^e(\phi)}{\partial \phi}\end{aligned} \tag{3.5}$$

With the addition of the maximum overhang constraint, the derivatives require just one additional term, $\frac{\partial \phi}{\partial \psi}$. This is due to the double layer of projections. The derivatives take on the form seen in Eq. (3.6)

$$\begin{aligned}\frac{\partial f}{\partial \psi} &= \frac{\partial f}{\partial \rho}\frac{\partial \rho}{\partial \phi}\frac{\partial \phi}{\partial \psi} \\ &= \frac{\partial f}{\partial \rho}\frac{\partial \rho}{\partial \phi}\left(\frac{\partial \psi}{\partial \psi}\phi_S + \psi\frac{\partial \phi_S}{\partial \psi}\right) \\ &= \frac{\partial f}{\partial \rho}\frac{\partial \rho}{\partial \phi}\left(\phi_S + \psi\frac{\partial \phi_S}{\partial \psi}\right)\end{aligned} \tag{3.6}$$

While the derivatives may look complicated, implementation is relatively simple and all constraints will be efficiently imposed through projection methods such that any solution will naturally satisfy the desired design constraints (no need for penalty methods).

3.2.2.2 Implementation

With the addition of the extra Heaviside function and the strict $\phi^i = \psi^i \phi_S^i$ rule, the optimization problem becomes highly nonlinear. Adding to this nonlinearity, it is seen through implementation that $\beta = 35$ and $\beta_2 = 20$ are required to accurately impose the overhang constraint. To help account for this extreme nonlinearity and to stabilize the optimization convergence a continuation scheme is implemented. The continuation is applied to the RAMP exponent, η. As η increases, the intermediate volume fraction material becomes less and less efficient, helping the algorithm converge to a 0-1 solution. As with many topology optimization algorithms, the continuation schemes are necessary to help guide the optimization closer to the global minimum. If the RAMP penalty parameter is set too high from the onset, the optimization problem would be highly nonlinear and extremely susceptible to local minima.

3.3 Solutions

The algorithm is tested on two typical topology optimization problems, the simply supported beam seen in Fig. 3.5 and the cantilever beam seen in Fig. 3.6 where the grey region indicates the design domain. All problems are run for a volume constraint of 60°, a minimum radius of 2.4 on a mesh size of 160x80. The solutions for the simply supported beam case are run using this 160x80 mesh but take advantage of symmetry to obtain 320x80 solutions.

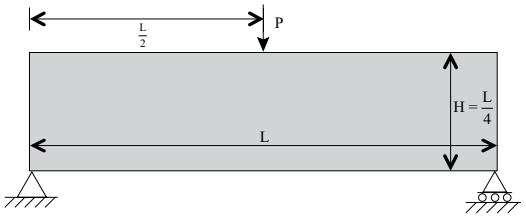

Figure 3.5: Simply supported beam definition.

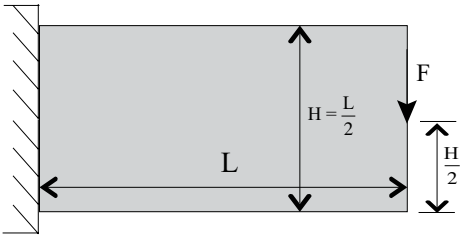

Figure 3.6: Cantilever beam definition.

First, solutions for the usual minimum compliance subject to only the minimum lengthscale control are presented (Fig. 3.7 and Fig. 3.8). These solutions are widely known and are shown for comparison purposes. Red indicates solid while blue indicates void.

If it is imagined that the structures must be build from the bottom up, then these conventional solutions violate the 45° maximum allowable overhang and would require support structures during the build process. This violation is highlighted in Fig. 3.7b and Fig. 3.8b, where the green lines indicate an overhang angle of less than 45° while the yellow lines indicate a violation of the overhang constraint, with an overhang angle of greater than 45°.

Now, the same MBB beam and cantilever beam problems are optimized using the maximum overhang optimization formulation. This algorithm will not allow material

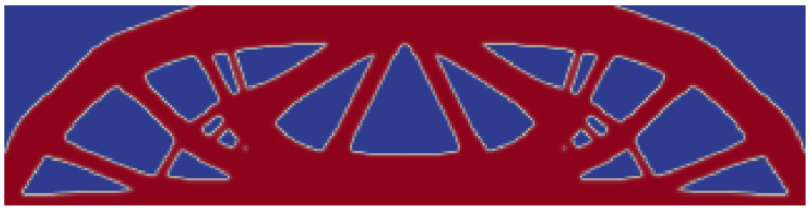

a Simply supported beam solution: no maximum angle constraint.

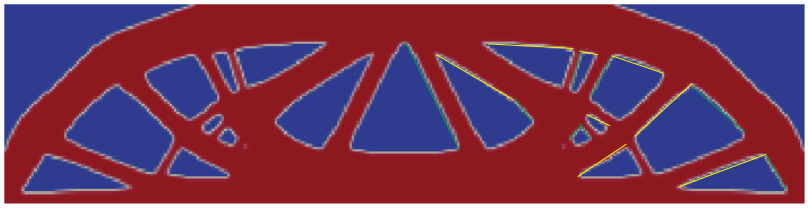

b Green indicates allowable overhang while yellow indicates a violation of the overhang rule.

Figure 3.7: Minimum compliance solution to MBB beam problem with no overhang constraint.

to exist unless it is adequately supported at an angle of 45° or less from vertical. The first test case will be for a part built from bottom up as seen in the following image, where the build plate designates the location of the first layer of material and the arrow indicates the direction of the build.

As can be seen in the solution for the MBB beam subject to the overhang constraint (Fig. 3.10b), every part of the topology is supported by material at an angle of ±45°. There are no yellow lines in Fig 3.10b, indicating a great agreement with the imposed constraint.

The cantilever problem was also solved subject to the 45° maximum overhang constraint. Again, the part will be built from bottom up, as indicated in Fig. 3.11.

As can be seen in Fig 3.12b, all of the overhangs in the solution adhere to the imposed overhang constraint. There was, however a small issue with the solution

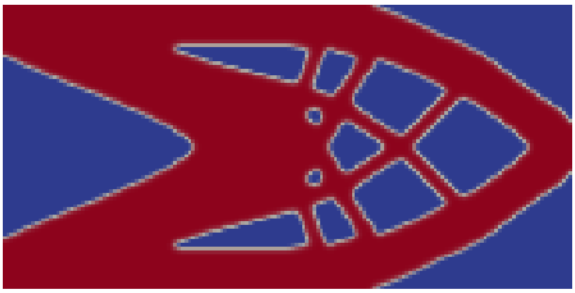

a Cantilever beam solution: no maximum angle constraint.

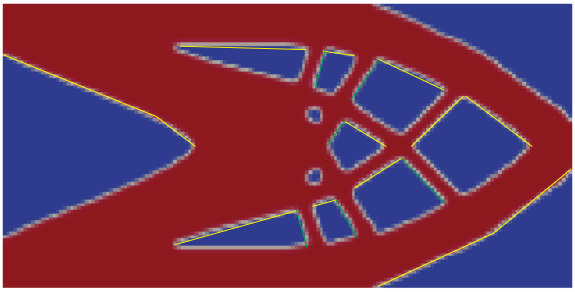

b Green indicates allowable overhang while yellow indicates a violation of the overhang rule.

Figure 3.8: Minimum compliance solution to cantilever beam problem with no overhang constraint.

convergence as there are a number of intermediate volume fraction regions. These can likely be fixed through further iteration or by imposing a higher η penalty in the RAMP material penalization method. To help solve this issue, a smarter continuation scheme should be developed. It is necessary to increase the β_2 parameter as much as possible without simultaneously making the optimization problem too nonlinear to solve for a feasible solution.

Also of concern is the choosing of the threshold parameter, T. As stated before, the value must be adjusted such that when there are an adequate number of supporting ϕ, the algorithm will allow the ϕ_S to be one. The algorithm is fairly sensitive to this

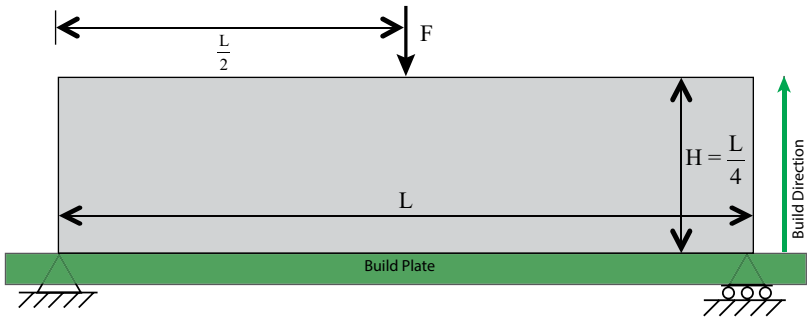

Figure 3.9: Upward build direction

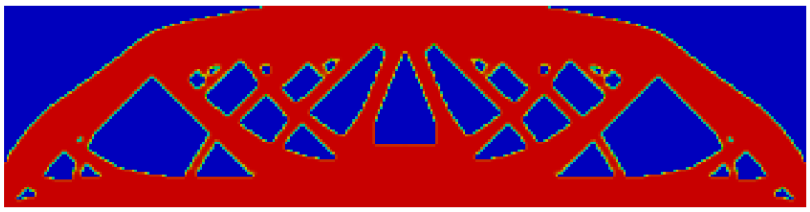

a Simply supported beam solution: 45 deg maximum angle constraint.

b Green indicates allowable overhang while yellow indicates a violation of the overhang rule.

Figure 3.10: Minimum compliance solution to MBB beam problem with 45 deg overhang constraint.

value T, as changing the value by too much can impose an inaccurate angle constraint.

3.3.1 Solutions Built From Different Direction

When producing a part, the engineer must choose the best orientation to obtain the best performing part. It will be seen what the optimal geometry of the part varied significantly when the part is built in a different orientation. As shown in Fig. 3.13,

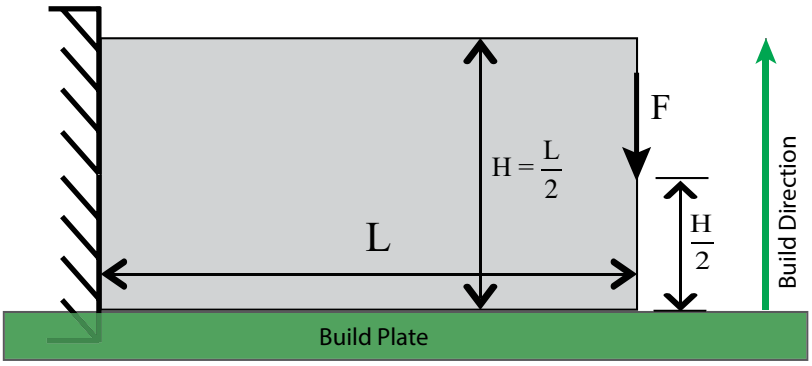

Figure 3.11: Upward build direction

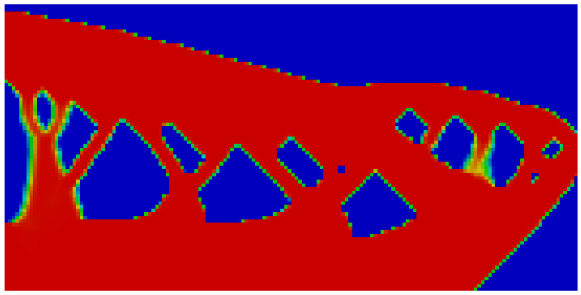

a Cantilever beam solution: 45 deg. maximum angle constraint.

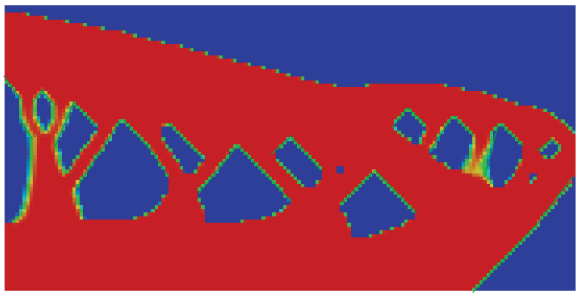

b Green indicates allowable overhang while yellow indicates a violation of the overhang rule.

Figure 3.12: Minimum compliance solution to cantilever beam problem with 45 deg overhang constraint.

the simply support beam will now be built in a downward fashion.

The solution adheres to the overhang constraint very well. It can be seen that the 'holes' are inserted into the domain with 45° overhangs when viewing the part from

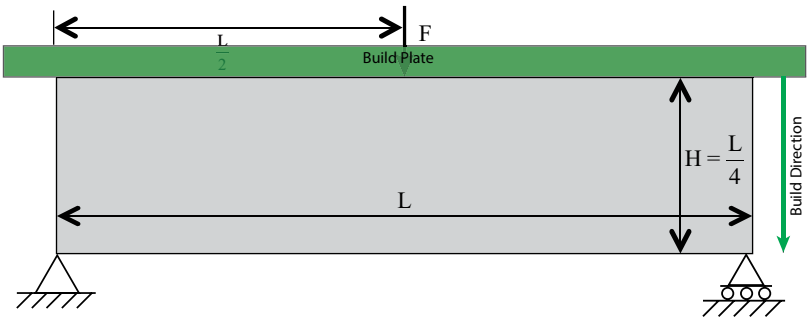

Figure 3.13: Downward build direction

an upside-down point of view. Likewise, the nearly horizontal overhangs present in the minimum compliance with no overhang constraint (Fig. 3.7) are now allowed, as the part is built from the opposite direction as the part in Fig. 3.10.

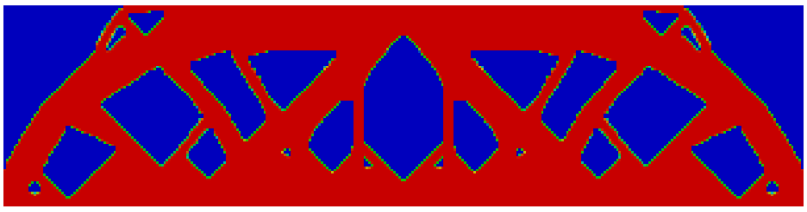

a MBB beam build down.

b Green indicates allowable overhang while yellow indicates a violation of the overhang rule.

Figure 3.14: Minimum compliance solution to MBB beam problem with 45 deg overhang constraint for downward build.

Of particular interest in this solution, Fig. 3.14, is the small truss-like structure on the top right and left of the domain. The algorithm determines how to build this small truss structure to create a much larger feature in the typical stress trajectory

location. Hence, the algorithm is trying to match the traditional minimum compliance with no overhang constraint solution as close as possible while still following the new overhang rule.

3.3.2 Solutions for various allowable overhang angles

To further exhibit the flexibility of this algorithm, it is now tested on angles greater than and less than 45°. Certain printing methods, especially FDM and photopolymer type techniques will not be able to achieve as large of an overhang angle without requiring support material. Of course it depends on each particular printer. For example, the Stratasys UPrint cannot achieve much overhang at all while the Stratasys Fortus 400MC is seen to be able to achieve an overhang angle of the typical 45° without requiring support material (For, 2015; UPr, 2015).

First, the simply supported beam problem will be solved for a maximum allowable overhang angle of 26°. As is expected and see in the solution in Fig. 3.15, this alters the final solution drastically.

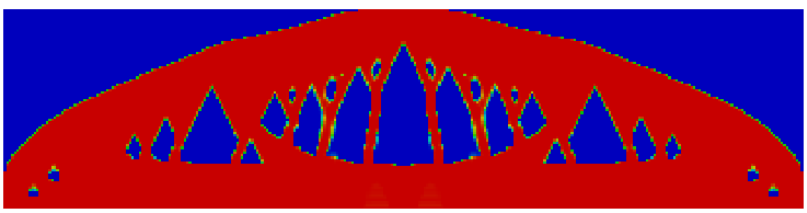

Figure 3.15: Upward built simply supported beam for 26 degree overhang.

Next, the algorithm is tested on overhang angles greater than the typical 45°. There are not many printers or printing technologies capable of this overhang angle, however it is prudent to test the algorithm on a number of angles to verify its robustness. Unfortunately, the solution for the simply supported beam with an allowable overhang angle of 63° does not fully follow the overhang rule and contains regions of fading material where the optimization algorithm has determined a solution that technically satisfies the projection-imposed constraint. While not a desirable solution, it highlights the need for fairly significant parameter tuning to impose the constraint accurately. It is likely that a better solution can be produced by increasing β from 35 to around 50+. This change, as always, comes with an increased nonlinearity in the optimization problem.

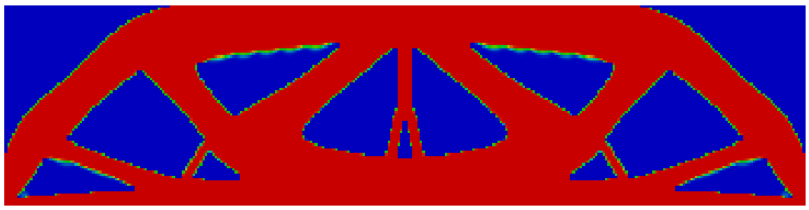

Figure 3.16: Upward built simply supported beam for 63 degree overhang.

Finally, the algorithm is tested with combination of a non-standard angle combined with a different build direction. To exemplify this, the algorithm is tested on the simply supported beam problem with an allowable overhang angle of 26° built from bottom down.

As seen in Fig. 3.17, the solution follows the overhang rule very well, although there are some regions of intermediate volume fraction material. This material can

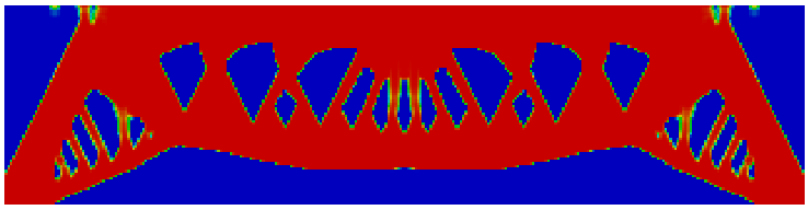

Figure 3.17: Downward built simply supported beam for 26 degree overhang.

likely be eliminated with a few more iterations of the optimization algorithm and are not of deep concern.

The solution is extremely interesting, as the topology is so altered by the imposition of the overhang angle constraint that material does not exist on the bottom of the domain, as is typical for the simply supported beam problem. However, the force flow does appear to follow the main stress trajectories.

3.4 Other details

3.4.1 Initial distribution of material, ρ

The initial guess for all problems solved in this chapter is an even distribution of ψ. Due to the thresholding Heaviside function, this did not yield an even distribution of material, ρ, as the initial guess. While this is non-standard for topology optimization problem, we believe it to be acceptable and suitable for this problem. With the initial guess, the material is biased towards the location the build plate. The initial distribution is essentially accounting for the fact that material must "grow" from the

build plate out to for any feature at the opposite side of the domain to exist.

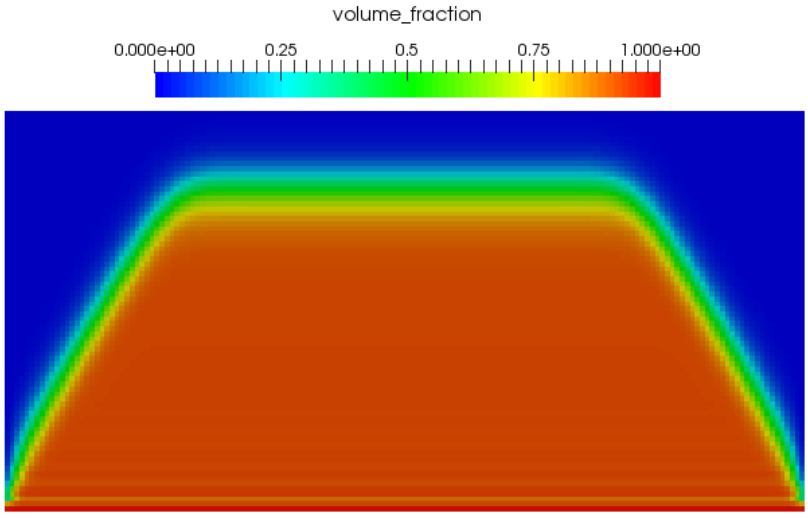

Figure 3.18: Initial Distribution of Material for 60% Volume Fraction

3.4.2 MMA parameter manipulation for convergence improvement

To help convergence, the move limits of the MMA optimizer were manipulated such that they were scaled by the magnitude of $\frac{\partial \rho}{\partial \phi}$. The asymptote increase parameter was inversely scaled with $\frac{\partial \rho}{\partial \phi}$. Likewise when there was fluctuation of a design variable, the asymptote decrease parameter was scaled such that higher values of $\frac{\partial \rho}{\partial \phi}$ resulted in greater tightening of the asymptotes.

3.5 Conclusion

This chapter proposes using topology optimization for the design of additively manufactured components which contain overhangs only up to the maximum achievable overhang. By limiting the overhangs to achievable angles, sacrificial support material is eliminated from the design process, saving time and money. The proposed method borrows ideas from previous projection methods by adding the constraint through use of an additional projection. In this way, the overhang constraint is imposed without adding an explicit constraint to the optimization problem.

Examples cases are shown for both the MBB beam problem and the cantilever beam problem. Traditional topology optimization solutions to these problems possess many violations of the overhang constraint. When the overhang constraint is imposed, the solutions are seen to possessed little or no violations, verifying that the constraint was properly imposed through the aforementioned projection scheme. To further verify the algorithm's robustness, it is applied to variations on the design problem including differing the build direction and the overhang angle. These solutions are drastically different from both the typical minimum compliance with no overhang solutions and the solutions for the 45° overhang with a bottom-up build direction.

One pitfall of the proposed algorithm is the extreme nonlinearity. As the overhang constraint may alter the optimal topology fairly drastically, it is not surprising that the optimization problem must be highly nonlinear. While more difficult to solve, when care is taken to adopt smart continuation schemes, the optimizer can drive

towards converged solutions. Another issue is the great increase in computational effort required to produce this solutions. Despite being coded in an efficient manner, the calculation of sensitivities proved to be extremely expensive – much more so than the solving of the finite element problem. Potential computational time savings may be possible by coding the algorithm in a more powerful language such as Fortran – MATLAB proved to be sluggish.

In the future, it would be great to have the ability for the optimizer to not only produce manufacturable solutions adhering to the overhang constraint, but have the optimizer chose the build direction. As seen in the solutions, the build direction has a drastic impact on the final optimal topology for particular design problems. Another direction which may be explored in the future is the use of more physics based methodologies to impose the constraint. Obviously it is seen that 45° is the typical achievable overhang angle, but this is through experience. If an algorithm could be developed which incorporates the material properties and the printing process into the optimization, the algorithm would be able to determine the actual achievable overhang angle based on such things as curling and cracking of the part during the build process. Currently, none of these phenomenons are incorporated into the model.

Still, the algorithms prove promising, with excellent solutions produced despite some issues identifying the best continuation method. Future tuning of topology optimization parameters and MMA parameters is bound to produce even better solutions.

Chapter 4

Hybrid Truss-Continuum Meshes and Bilinear material models

4.1 Introduction

In development, but not yet mainstream, are additive manufacturing methods that may print both a material but also place discrete prefabricated objects during the build process to produce unique composite parts. These new parts may have an stiffener, or actuator placed to improve performance or give the ability of actuated motion in printed parts. In this section, an algorithm is developed to design for composite material which contain discrete objects within a material matrix. The material is assumed to be stress dependent, where it may possess properties such that it has a much greater elastic modulus in compression than in tension. Likewise,

the discrete objects may also have stress-dependent material properties.

4.1.1 Discrete Object Placement Additive Manufacturing Processes

The DREAMS Lab (Design, Research, and Education for Additive Manufacturing Systems Lab) at Virginia Tech is developing techniques for embedding discrete objects within the printing process (Meisel et al., 2014). By not only printing solid parts, but integrating prefabbed components, the printed part becomes more complex but potentially offers capabilities not possible with purely printed features. When considering such a system, it will be desirable to optimize both the location of these discrete actuation objects and the overall topology of the printed part (Meisel et al., 2014). A schematic of the placement of a discrete object within the printing process is seen in Fig. 4.1.

As a first step towards this complex design problem, a hybrid truss-continuum approach is developed. As will be seen types. As the 3D printing process is still in development at DREAMS, we turn instead to reinforced concrete design in civil engineering structures. Reinforced concrete design shares similar aspects to the embedded object idea in that the concrete phase is monolithic and the steel rebar is a discrete object, typically coming in straight sections, that is embedded in the concrete phase. Potential extension of the proposed approach to embedded objects in

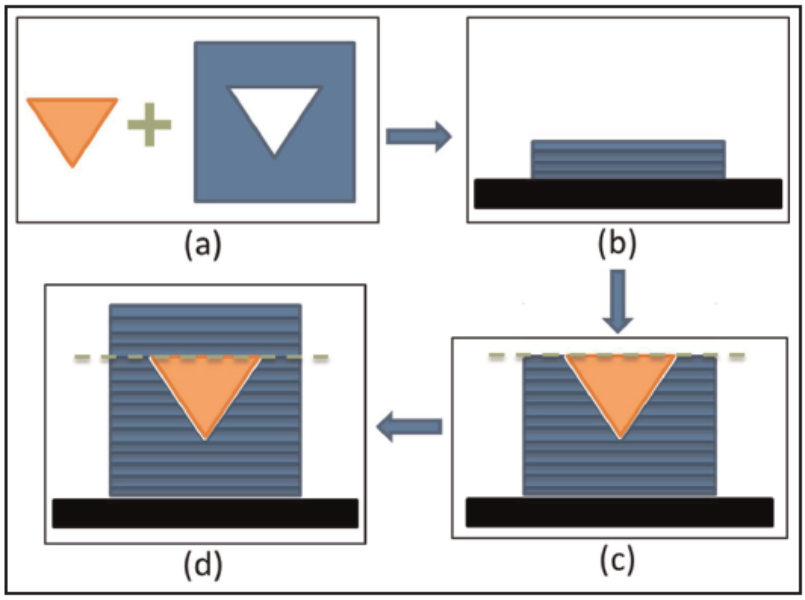

Figure 4.1: Embedding process for a general shape (triangle shown here) (Meisel et al., 2014)

additive manufacturing would be straightforward, as will be discussed. Additionally, the proposed topology optimization approach herein is capable of handling stress-dependent, anisotropic constitutive relations. Although targeted towards the stress-dependent behavior of concrete, the algorithm may likewise be useful for addressing the anisotropies exhibited by 3D printed materials, where the orientation of the properties are dictated by the build direction of the part (Riddick et al., 2012).

4.1.2 Introduction and Background to Strut and Tie Concrete Design

We begin with a brief review of reinforced concrete design by strut-and-tie modeling, before developing the hybrid topology optimization algorithm and results. Reinforced concrete is a complex composite material that continues to challenge those researchers attempting to describe its behavior with mechanics-based models. In the late 1800s, Wilhem Ritter and Emil Mörsch developed a rational engineering approach to circumvent these analysis complexities. The idea was to assume a cracked reinforced concrete beam behaves like a truss. This truss analogy, known today as a strut-and-tie model, provides a convenient visualization of force flow and identifies required reinforcing steel locations that can be used to design and detail a concrete member.

A drawback of early concrete truss models was the arbitrary nature with which they could be formulated, and the lack of scientific theory to support the practically-minded idea developed by Ritter and Mörsch. The scientific support for cracked reinforced concrete truss models came several decades later with research by Marti, who established a technical foundation for the truss model concept by relating truss behavior to a lower bound plasticity theory (Marti, 1980). Marti and others concluded that an optimum concrete truss model could be achieved by locating the compressive struts and tension ties coincident with the elastic stress trajectories in a member,

and that higher ductility and improved structural performance at an ultimate limit state could be achieved with a stiffer truss. The engineering judgment required to obtain an accurate truss model was viewed as a drawback of the design approach, and Marti recommended future research on computational tools that could automate the identification of viable strut-and-tie geometries.

The momentum from Marti's work, in combination with experimental and analytical work by Collins and Mitchell on truss models for shear and torsion (Collins and Mitchell, 1980), led to a groundbreaking set of design guidelines for truss models proposed by Jörg Schlaich and his colleagues at the University of Stuttgart (Schlaich et al., 1987). Schlaich states that the stiffest truss model is the one that will produce the safest load-deformation response because limiting truss deflection prevents large plastic deformations in the concrete. Maximizing stiffness correlates mathematically to minimizing reinforcing steel's elastic strain energy. However, Schlaich admits that selecting the optimum truss model may be difficult with the energy criterion, requiring "engineering intuition" that has contributed to past structural failures.

Reinforced concrete design guidelines employing strut-and-tie models were introduced into the Canadian Concrete Design Code in 1984 (CSA, 1984), followed by European practice (Eur, 1993), the American Association of State Highway and Transportation Officials (AASHTO) Load and Resistance Factor Design (LRFD) bridge code (Ame, 1994), and finally the American Concrete Institute (ACI) building code (ACI, 2002). The method's widespread use is currently stymied though by a lack of

mechanics-based tools for identifying the force flow and visualizing the truss shape needed in design.

It is the goal of the research described in this manuscript to create a new automated tool for visualizing the flow of forces in reinforced concrete and prestressed concrete structural members. The approach couples truss and continuum topology optimization methodologies to create a hybrid routine that leads to strut-and-tie solutions consistent with Schlaich's hypothesis that placing reinforcing steel consistent with the stiffest truss results in superior structural performance over traditional designs, i.e., reduced crack widths and improved capacity. Force paths (topologies) can be identified and studied for any general concrete domain and with any loading and boundary conditions, and the tensile forces in the reinforcing steel are readily available to a designer for sizing. With the force paths defined, a designer may then apply existing code-based strut-and-tie design provisions to evaluate ductility and ultimate strength. An introduction to truss and continuum topology optimization from the perspective of reinforced concrete design is provided in the next section, followed by step-by-step implementation of the hybrid truss-continuum topology optimization approach, the first such hybrid algorithm to our knowledge. The manuscript concludes with examples of force flow topologies for a concrete beam, a hammerhead pier, a deep beam with a cutout, and a prestressed concrete block.

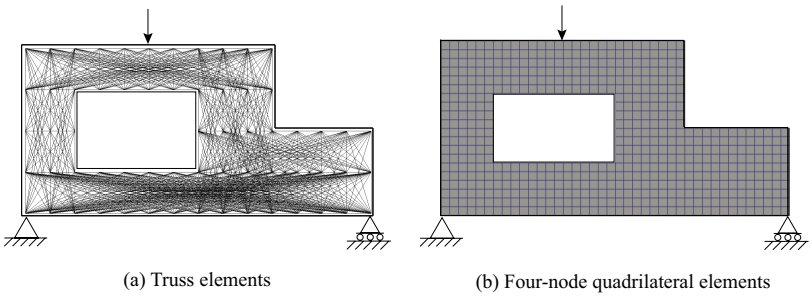

Figure 4.2: Example of a topology optimization design domain with hole discretized using (a) truss elements and (b) four-node quadrilateral elements.

4.2 Topology optimization background and formulation

Recent advances in optimization algorithms, and specifically growth in the field of topology optimization, have led to a new family of methods for identifying reinforced concrete truss models consistent with the rules outlined by Schlaich for optimal performance in service and at an ultimate limit state. In topology optimization, the design domain (structural component) is discretized with structural elements, typically truss or continuum (solid) elements, with the goal of identifying the "concentration" of material in each element (Fig. 4.2). Elements receiving little or no material by the optimizer at convergence are deemed structurally insignificant and removed from the structural domain in post-processing (Bendsøe and Sigmund, 2003a; Ohsaki and Swan, 2002).

Following the guidelines of Schlaich, the objective is to design a truss topology with maximal stiffness. This may be equivalently formulated as a minimum compliance

problem where the goal is to minimize the external work done by the applied loads (and strain energy stored in the structure) for a limited volume of material, expressed in general as follows:

$$\begin{aligned} \min_{\boldsymbol{\rho}} \quad & f(\boldsymbol{\rho}) = \boldsymbol{F}^T \boldsymbol{d} \\ \text{subject to:} \quad & \boldsymbol{K}(\boldsymbol{\rho})\boldsymbol{d} = \boldsymbol{F} \\ & \sum_{e \in 1} \rho^e v^e \leq V \\ & 0 \leq \rho^e \leq \rho^e_{\max} \quad \forall\, e \in \Omega \end{aligned} \tag{4.1}$$

where design variable vector ρ is the encoding of the material concentration (the structural design), ρ^e is material concentration in element e (e.g., the cross-sectional area of truss element e), $\boldsymbol{F}$ are the applied nodal loads, $\boldsymbol{d}$ are the nodal displacements, v^e is element volume for unit ρ^e (element length for truss structures), V is the available volume of material, and $\rho^e_{\max}$ is the design variable upper bound. The global stiffness matrix $\boldsymbol{K}$ is assembled ($\boldsymbol{A}_e$) from element stiffness matrices $\boldsymbol{K}^e$ as follows:

$$K(\rho) = \underset{e \in \Omega}{\boldsymbol{A}} \boldsymbol{K}^e(\rho^e) \quad , \quad \boldsymbol{K}^e(\rho^e) = \left((\rho^e)^\eta + \rho^e_{\min}\right)\boldsymbol{K}^e_0 \tag{4.2}$$

where $\boldsymbol{K}^e_0$ is the element stiffness matrix for unit ρ^e, $\rho^e_{\min}$ is a small positive number to maintain positive definiteness of the global stiffness matrix, and the exponent parameter $\eta \geq 1$ is an optional penalty term that may be used to drive solutions to the design variable bounds (Bendsøe, 1989). This penalization approach is known as

the Solid Isotropic Material with Penalization (SIMP) method and is widely used in the topology optimization community.

The optimization problem in Eq. 4.1 is solved using gradient-based optimizers, chosen as the Method of Moving Asymptotes (MMA) (Svanberg, 1987) in this work. Such optimizers are guided by design sensitivities, or derivatives with respect to the design variables. Minimum compliance sensitivities may be found using the adjoint method or direct differentiation, and take the well-known form of the elemental strain energies:

$$\frac{\partial f}{\partial \rho^e} = -\eta(\rho^e)^{\eta-1}\boldsymbol{d}^{eT}\boldsymbol{K}_0^e\boldsymbol{d}^e \tag{4.3}$$

where $\boldsymbol{d}^e$ is the elemental displacement vector of element e. The reader is referred to Arora (1997) and Bendsøe and Sigmund (2003a) for sensitivity analysis background.

4.2.1 Truss topology optimization

Truss topology optimization begins with a densely meshed domain, referred to as a ground structure (Fig. 4.2a), and cross-sectional areas are then optimized. Following convergence, members having (near-)zero area are removed to identify the final optimal topology and corresponding distribution of cross-sectional areas (e.g., (Bendsøe et al., 1994)). Following this approach, Biondini et al. (1999) and Ali and White (2001) solved minimum compliance formulations using mathematical programming

to develop concrete truss models consistent with the elastic stress trajectories in a general concrete domain. Ali demonstrated with nonlinear finite element modeling to collapse of short reinforced concrete cantilevers that ultimate strength increases as truss stiffness increases, an important result supporting Schlaich's hypothesis that was later confirmed with experimental results by Kuchma et al. (2008).

In typical truss topology optimization, the cross-sectional areas ρ^e are considered un-penalized continuous variables ($\eta = 1$) with relaxed upper bound $\rho^e_{\max}$. Under these conditions, it can be shown that minimum compliance optimization yields a topology of uniform strain energy density and thus a uniformly stressed design (Bendsøe et al., 1994). This means the target volume V specified by the designer is arbitrary and cross-sectional areas may be uniformly scaled to satisfy a stress constraint, such as the reinforcing steel yield stress. This may be extended to the case where truss members have different properties in tension and compression (Achtziger, 1996; Rozvany, 1996).

The minimum compliance topology optimization truss is illustrated for a reinforced concrete deep beam shown in Fig. 4.3. The topologies are overlaid on experimental testing data indicating crack paths, and therefore principal tension trajectories, for this beam. The traditional truss model and reinforcing layout places steel near the bottom of the deep beam (Fig. 4.3a), which is an optimal location at midspan but is less efficient at providing resistance to principal tension near the supports where wide diagonal cracks may develop under load as shown. The mini-

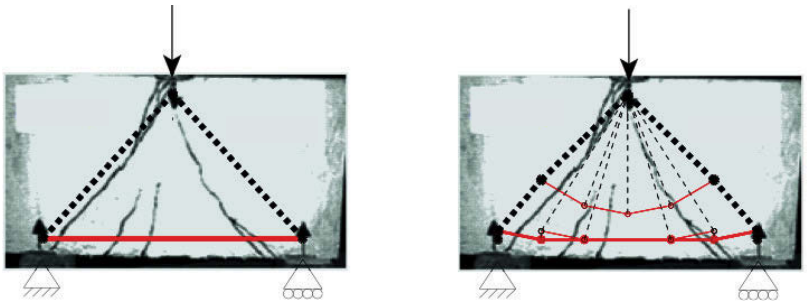

(a) Traditional concrete truss model

(b) Minimum compliance truss model

Figure 4.3: Compare (a) traditional concrete truss model and (b) minimum compliance truss model derived with topology optimization. Black dashed lines represent compression carried by the concrete, red solid lines represent tension carried by the reinforcing steel. Experimental results provided in the background are from Nagarajan and Pillai (2008).

mum compliance truss model (Fig. 4.3b) helps the designer understand where the cracks will form, in this case showing that inclined steel reinforcement (red tension ties in Fig. 4.3b) should be provided to bridge and therefore better resist the principal tension cracks.

One of the drawbacks of truss topology optimization is that solutions are dependent on the ground structure chosen by the designer. This includes nodal locations and element connectivity, as the designer has essentially restricted potential force paths a priori. Using a very fine mesh with small nodal spacing and extensive element connectivity (e.g., connecting every node together as shown in Fig. 4.2a) offers the most design freedom and allows topologies to approximate curved trajectories (Fig. 4.3b). By using a coarser mesh and/or simpler connectivity, the designer restricts the design space and subsequently global optima will underperform those found with

more refined ground structures- i.e., they will have higher compliance and hence lower stiffness. The advantage of using coarse meshes, however, is that optimal topologies are typically less complex and thus easier to construct. This tradeoff between stiffness and constructability will be revisited in the examples section.

4.2.2 Continuum topology optimization

Continuum topology optimization offers an alternative free-form approach to visual force flow. The domain is discretized with finite elements (four node quadrilateral elements in Fig. 4.2b) and the goal is to determine whether or not an element contains material, i.e., is a solid ($\rho^e = \rho^e_{\max} = 1$) or a void ($\rho^e = 0$). The resulting connectivity of the solid elements defines the optimized structure. In the application to reinforced concrete force visualization, the solid phase represents load-carrying material (concrete or steel), while the void phase in the continuum model indicates locations of "background" concrete that is not part of the force model.

To enable use with gradient-based optimizers, the binary (solid-void) condition on ρ^e in is relaxed and solutions are steered towards 0-1 distributions using the SIMP penalty term $\eta > 1$ in Eq. 4.2 (e.g., $\eta = 3$). It is well known that this approach leads to numerical instabilities of checkerboard patterns and solution mesh dependency if the design space is not restricted to prevent them (see Sigmund and Peterson 1998 for review). These issues are circumvented herein by imposing a minimum length scale (minimum thickness) on load-carrying members. This not only numerically stabilizes

the formulation, but has the added benefit of providing the designer a tool for influencing constructability as requiring larger features tends to produce more simpler topologies. Minimum length scales can be imposed on a topology using an efficient projection-based algorithm (Guest, 2009a,b; Guest et al., 2004) where an auxiliary variable field ϕ serves as the independent optimization variable and is mapped onto the finite element space to determine the topology, meaning finite element variables ρ are a function of ϕ. This mapping is rigorously constructed such that the minimum length scale of designed topological features is naturally controlled at negligible added computational cost. The reader is referred to Guest et al. (2011) for details on numerical implementation of the algorithm.

Several researchers have explored the use of continuum topology optimization as a tool for reinforced concrete analysis and design. Liang et al. (2000) implemented a heuristic plane stress topology optimization approach, commonly referred to as Evolutionary Structural Optimization (ESO), to derive concrete truss model shapes for common cases including a deep beam and a corbel. Kwak and Noh (2006) and Leu et al. (2006) employ similar ESO-based algorithms. Bruggi (2009) solves 2D and 3D strut-and-tie design problems using a gradient-based topology optimization algorithm with heuristic sensitivity filtering to improve solution efficiency, while Victoria et al. (2011) use a heuristic optimality criterion updating scheme allowing different moduli for tension and compression phases. More recently, Amir and Bogomolny (2011) use material-specific elasto-plastic models to specifically enhance reinforced concrete

performance at an ultimate limit state.

The primary advantage of the continuum approach is the free-form design evolution that identifies high-performance topologies consistent with the force path in a structural component. Unlike truss topology optimization, where the designer selects node locations and element orientations of the force flow model a priori, it is the optimizer itself that identifies these locations and orientations in continuum topology optimization. Disadvantages are that the tension regions are not defined as discrete bars, requiring post-processing of the continuum results to produce truss representations in order to size concrete reinforcement. Continuum topologies, as they are generated in a free-form manner, are also typically more complex and therefore may be more difficult to construct than those found directly using truss topology optimization. As will be shown, the geometric restriction methods (minimum length scale) discussed previously provide a means for controlling this complexity.

4.2.3 Examples of topology optimization force visualization for reinforced concrete

A traditional linear elastic topology optimization approach is demonstrated for several reinforced concrete design examples. These examples will provide baseline solutions that can be compared to the hybrid model results discussed later in the manuscript. For the truss topologies, solid red lines represent tension (steel) ties and

dashed black lines represent the compressive struts (as in Fig. 4.3). Line thickness is proportional to axial force and therefore the required cross-sectional area for the steel tension ties. In the continuum representations, the solid black features represent the force flow topology, i.e., the load-carrying concrete and steel ties. A single isotropic, linear elastic material model is assumed for both the concrete and the steel. Continuum examples use four-node quadrilateral plane stress elements. Domain dimensions and loads are given in relative (unitless) measures.

4.2.3.1 Simply-supported beam

The design domain for a reinforced concrete beam with a point load is shown in Fig. 4.4a, along with a typical strut-and-tie model in Fig. 4.4b. The topology optimized truss and continuum models are shown in Fig. 4.4c and 4.4d respectively, with the truss solution achieving a uniformly stressed state as expected. These solutions illustrate that the maximum elastic stiffness (minimum compliance) can be achieved by placing the reinforcing steel orthogonal to the compressive stress trajectories. This design philosophy is similar to the practice of providing inclined shear stirrups to bridge diagonal cracks (G., 1992).

As previously mentioned, one of the disadvantages of the truss approach is that solutions are mesh dependent. In selecting a ground structure, the designer limits the potential force flow paths a priori. Fig. 4.5, for example, shows three different ground structures containing a number of nodes ranging from 10 (coarse) to 85 (fine) in a

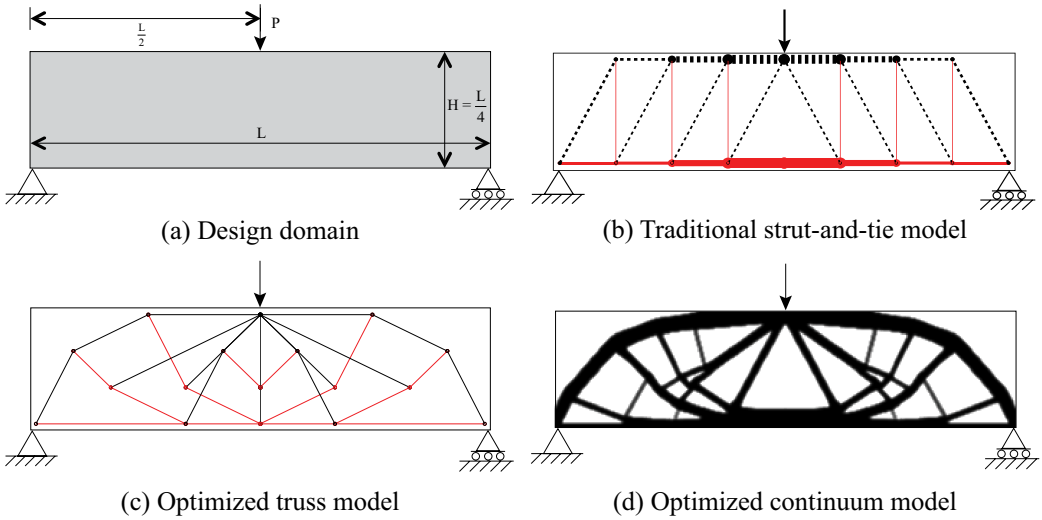

Figure 4.4: Force visualization for a reinforced concrete simply-supported beam with topology optimization. In the truss models, the solid red lines indicate tension (steel) members and black dashed lines compression members, with line thickness indicating relative axial force.

lattice format. The optimized topology found using the fine ground structure closely resembles the principal stress trajectories and consequently offers a compliance that is 22% lower and estimated volume of required steel that is 14% lower than solution found using the coarse mesh. The tradeoff, however, is constructability, as the simpler topology is likely easier to construct. Ultimately, the decision is left to the designer to balance the cost of material and labor, while topology optimization offers a tool for exploring the design space.

4.2.3.2 Deep beam with a cutout

Reinforced concrete designs can be readily obtained with topology optimization for complex domains such as the deep beam with openings example shown in Fig. 4.6a.

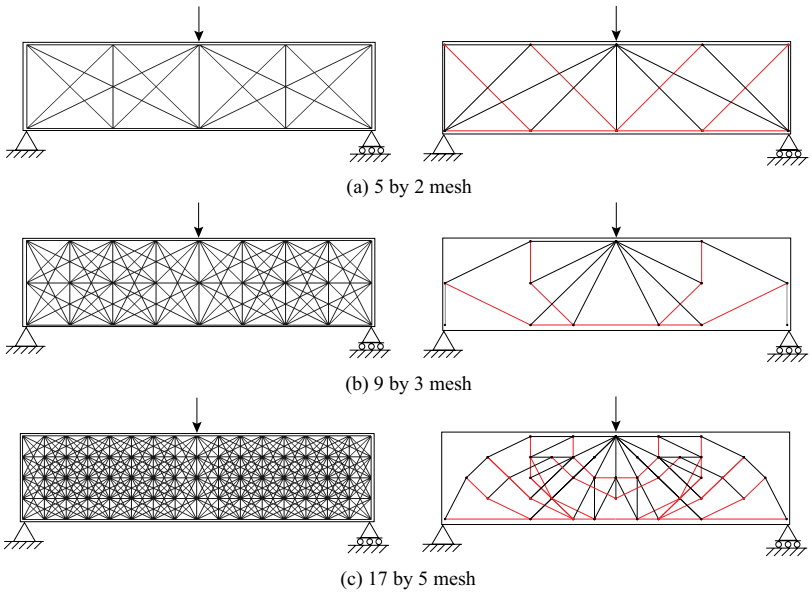

Figure 4.5: Truss solutions using different ground structures having normalized compliances of (a) 1.000, (b) 0.792, and (c) 0.779. Although truss solutions are mesh dependent, topology optimization allows the designer to explore the tradeoffs between constructability and truss stiffness. The number of nodes in the lattice mesh are shown under each image.

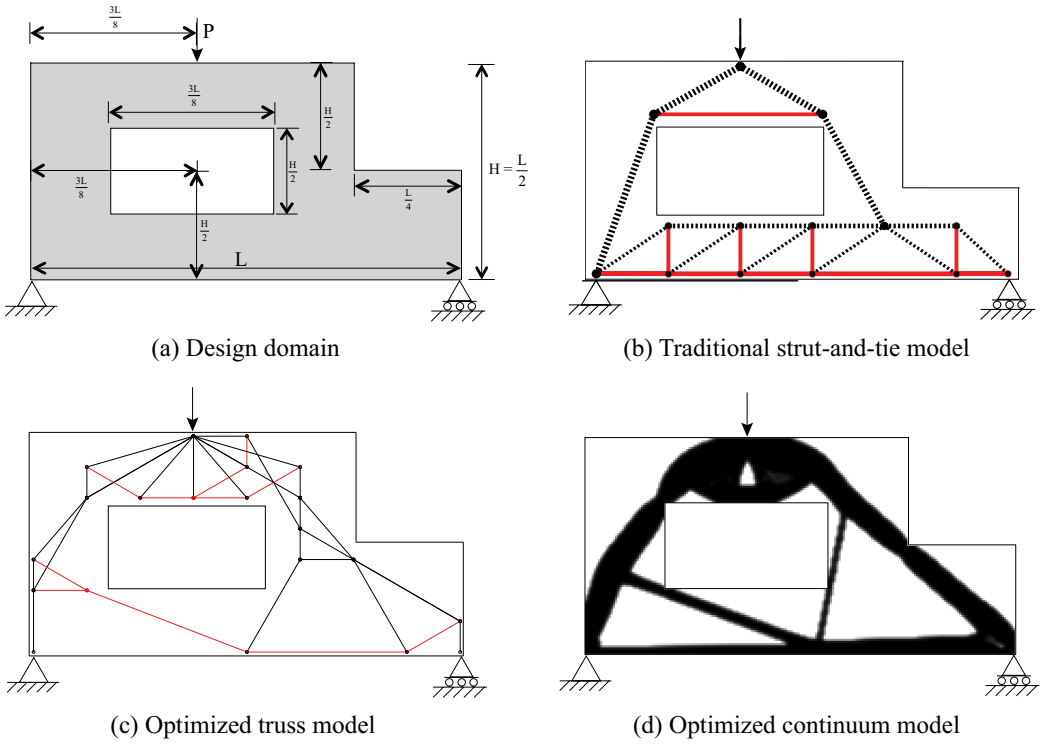

Figure 4.6: Design of deep beam with cutout via topology optimization

The minimum compliance design in this case results in a reinforcing layout that does not require stirrups in the confined space under the hole, simplifying construction. Also, Fig. 4.6c and 4.6d show that there is tension in the lower left corner of the beam, below the cutout, which could result in splitting cracks from the corner of the hole to the edge of the beam. A designer might miss this potentially detrimental behavior with a traditional strut-and-tie solution (Fig. 4.6b). A drawback of the truss solution (Fig. 4.6c) is the lack of reinforcement over the left support where tensile stresses may develop due to bearing this will be revisited with the hybrid model.

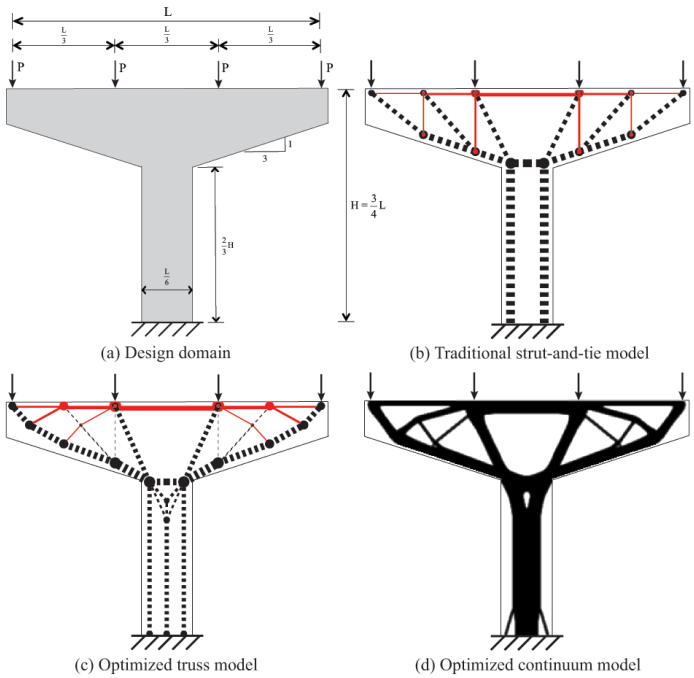

Figure 4.7: Design of hammerhead pier supporting four girder lines with topology optimization

4.2.3.3 Hammerhead bridge pier

A hammerhead bridge pier is typically designed with the truss model shown in Fig. 4.7b. Vertical shear stirrups are spaced evenly across the pier cap with a top mat of reinforcing steel to controlling cracking at the girder bearing line. The minimum compliance truss and continuum models in Fig. 4.7c and Fig. 4.7d demonstrate that for the loading case considered the shear stirrups do not coincide with the internal tensile force trajectories and instead draped reinforcing steel or post-tensioning would be a more appropriate design solution.

Fig. 4.8 illustrates the potential benefits of imposing minimum length scale on the continuum structural members. Increasing the required minimum strut-and-tie

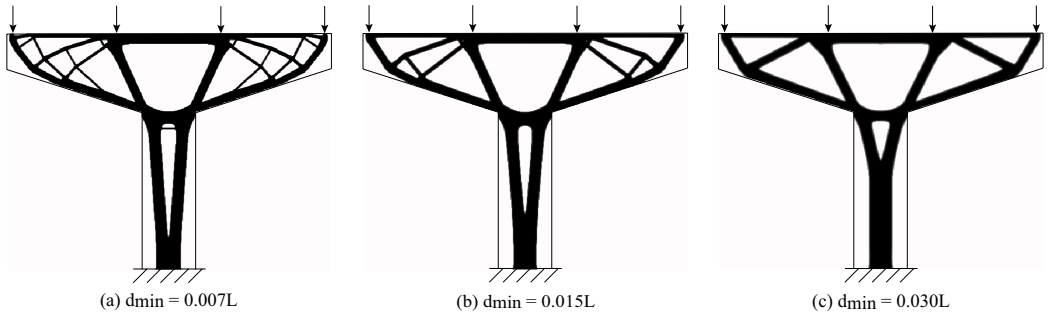

Figure 4.8: Hammerhead pier example solved using continuum topology optimization with different minimum prescribed length scales (diameter $\boldsymbol{d}_{\min}$). Larger length scales reduce efficiency but also complexity.

thicknesses simplifies the topology and reduces the number of designed steel ties from four draped (Fig. 4.8a) to three (nearly) straight (Fig. 4.8b) to two straight (Fig. 4.8c) ties in each half of the pier. With direct control over the length scale, a designer may generate a suite of solutions where structural performance and constructability are balanced.

4.3 Motivation for a hybrid truss-continuum topology model

The results presented in the previous section are consistent with those reported in the literature. Optimized topologies largely follow the principal stress trajectories even for complex domains treated in Biondini et al. (1999), Ali and White (2001), and Bruggi (2009). While solutions found using truss and continuum topology optimization follow these general trends, there are distinct differences in terms of solution

stiffness, as quantified by the objective function, and constructability between the two approaches.

The free-form nature of continuum topology optimization is evident as the presented force trajectories may take any shape, have varying thickness, and/or connect with other members at any angle. In this sense, the optimizer selects both the locations of the 'nodes' of the force transfer topology and also the corresponding flow paths. This design freedom enhances solution efficiency but may produce solutions that are less practical from a construction point of view (even with length scale control), potentially negating any cost saving from solution efficiency. This is in contrast to the truss approach, which restricts the design space by requiring loads to flow in straight paths along predefined candidate orientations. Truss models therefore underperform continuum solutions, but likely improve constructability as steel rebar and strands may be placed in straight segments.

A key limitation of both topology optimization approaches as presented is the assumption of isotropic, linear elastic constitutive models. This assumption means that traditional topology optimization approaches to reinforced concrete design may miss transverse tensile stresses that develop in the concrete phase due to load spreading, an outcome that is observed even when algorithms are implemented that use different moduli for the tension and compressive materials (Victoria et al., 2011). In some design settings, for example prestressed concrete, this missing treatment of orthotropy may lead to invalid strut-only solutions that falsely indicate that steel reinforcement

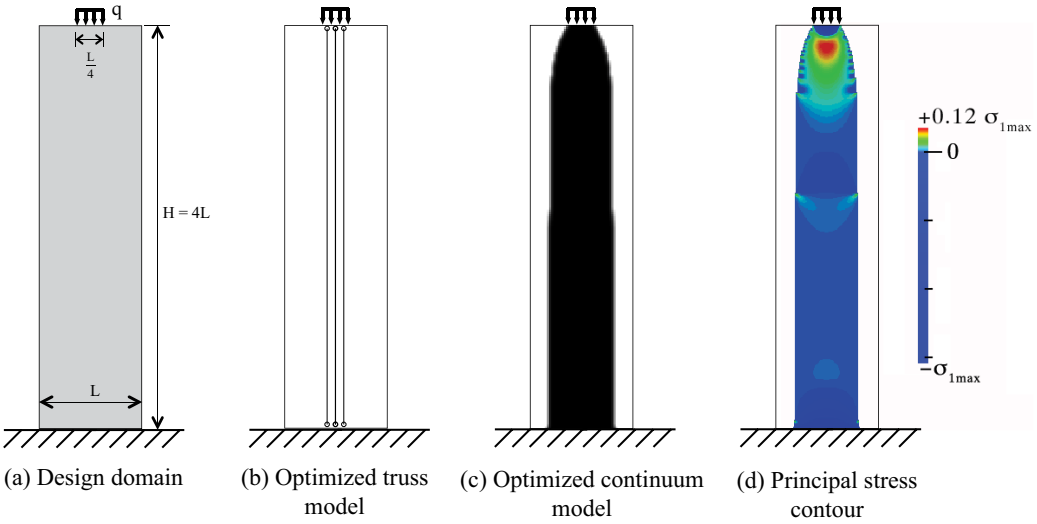

Figure 4.9: Compression block example illustrating strut-only solutions: (a) load and boundary conditions, (b) truss optimization producing three vertical struts, and (c) continuum optimization producing a single large strut. Strut-only solutions fail to capture tensile stresses due to force spreading, which is clearly seen in (d) the maximum principal stress plot for solution (c).

is not needed. Fig. 4.9 illustrates this shortcoming for a concrete block subjected to a compressive load solved with truss (Fig. 4.9b) and continuum topology optimization (Fig. 4.9c) for minimum compliance. The topologies indicate a strictly compressive load path, failing to capture load spreading that will create transverse tensile stresses in the concrete phase as shown by the principal stress plot in Fig. 4.9d (only major stresses shown, as all minor stresses are compressive). A similar instance is seen over the left support in the topology optimized truss solution for the deep beam with cut-out (Fig. 4.6c).

Overcoming this limitation requires breaking from traditional linear elastic topology optimization methodologies. We propose herein a bilinear hybrid approach. The idea is that tension members are implemented as truss elements in the optimization

formulation, resulting in reinforcing steel design that is straight, simply placed, and easily sized. Continuum elements form force paths consistent with the elastic stress trajectories and couple with the tensile truss members to carry compression in the concrete. This separation of the compressive and tensile load carrying elements allows different moduli to be used for the different materials, and more importantly, is shown to capture force-spreading that results in tensile stresses orthogonal to compression struts, i.e., splitting stresses near a prestressing steel anchorage. The details of this hybrid approach are presented in the next section.

4.4 Hybrid Truss-Continuum Strut-and-Tie Models

A new force visualization approach is proposed that utilizes a hybrid truss-continuum design domain to address the identified shortcomings in the prevision section, specifically the inability of the topology solutions to simulate force spreading and the cumbersome post-processing required to size reinforcing steel with continuum solutions. In the hybrid approach, first postulated in Guest et al. (2011), the steel phase is modeled using truss elements with high tensile stiffness and zero compressive stiffness, while the concrete phase is modeled using continuum elements with high compressive stiffness and low tensile stiffness. The hybrid formulation therefore requires tension load paths to be carried with steel truss members and compressive load paths to be

carried with continuum concrete members. This not only captures force-spreading as will be shown, but also leverages the desirable properties of both topology optimization approaches: load-carrying concrete continuum may take any shape, as it need not be constructed, while steel reinforcement is placed in straight segments. To our knowledge, this is the first truss-continuum hybrid approach in topology optimization.

4.4.1 Hybrid mesh

The hybrid mesh is achieved by embedding a truss ground structure into a continuum finite element mesh. The design domain Ω is discretized with a lattice mesh of nodes and the continuum mesh Ω_t uses every node, while the truss mesh t is more sparse with members connected at every few nodes in order to reduce complexity of the final steel configuration. This is seen below in Fig. 4.10 where there are 12 continuum elements in each direction, but the truss elements are connected every four nodes (grey continuum elements, black truss elements). Force transfer between the meshes occurs at the shared nodes, and a nonslip condition for the steel reinforcement is assumed. This relative node spacing of four to one was selected to approximately match the truss and continuum ground structures in the preceding examples. As previously discussed, using a denser truss ground structure (skipping fewer continuum nodes) would likely lead to more complex reinforcement patterns, while coarser truss ground structures would likely produce simpler patterns. It is not recommended, however, that the truss node spacing be less than the continuum node spacing as this

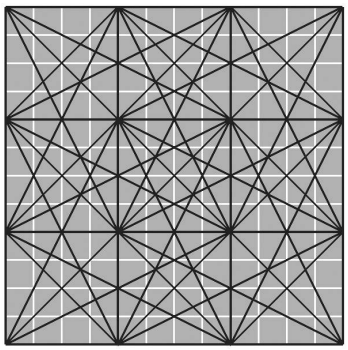

Figure 4.10: Interaction between continuum (four node quadrilaterals) and truss domains

would require compression truss elements to have nonzero stiffness.

4.4.2 Material models

The bilinear stress-strain relations for the steel and concrete are shown in Fig. 4.11. Young's moduli for the steel are assumed 200 GPa (29,000 ksi) in tension and zero in compression, while moduli for the concrete are assumed 24.9 GPa (3,600 ksi) in compression and 2.0 GPa (290 ksi) in tension. A nonzero tensile stiffness is used for the concrete to prevent singularities in the global stiffness matrix. Such singularities would otherwise arise at nodes that are not connected to truss elements and that are located in regions achieving a state of tensile stress.

As truss members carry only axial forces, the bilinear constitutive steel model is straightforward to implement. Denoting the truss elemental design variables (cross-sectional areas) as $\boldsymbol{\rho}_t$, the element stiffness matrix of a truss element $\boldsymbol{K}_t^e$ is now stated as follows:

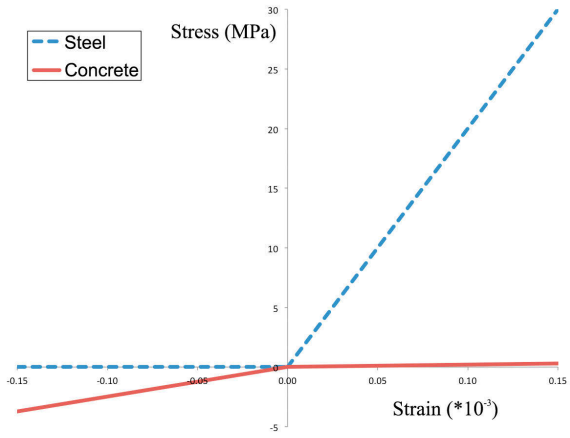

Figure 4.11: Stress-strain relationships for the continuum concrete and truss steel models.

$$\boldsymbol{K}_t^e\left(\rho_t^e, \boldsymbol{\sigma}_t^e\right) = \left(\rho_t^e\right)^{\eta_t} \boldsymbol{K}_{0,t}^e\left(E_t(\boldsymbol{\sigma}_t^e)\right) \tag{4.4}$$

where E_t is the Young's modulus of truss element and dependent on the sign of the elemental (axial) stress σ_t^e (Fig. 4.11), and $\boldsymbol{K}_{0,t}^e$ is the truss element stiffness matrix for unit ρ_t^e.

For the concrete continuum elements, an orthotropic constitutive model is adapted from the bilinear elastic portion of a model proposed by Darwin and Pecknold (1977). The model combines the different Young's moduli as a function of the principal normal stresses and orientation of the principal stress plane. This rotational dependence is key to capturing force spreading and gives preference over existing isotropic stress-dependent stiffness tensors proposed in literature (e.g., (Cai, 2011)).

Denoting the continuum elemental design variables (volume fractions) as $\boldsymbol{\rho}_c$, the element stiffness matrix of a continuum element $\boldsymbol{K}_t^e$ is now stated as

$$\begin{aligned} \boldsymbol{K}_c^e\big(\rho_c^e, \boldsymbol{\sigma}_c^e\big) &= \Big(\big(\rho_c^e\big)^{\eta_t} + \rho_{\min}^e\Big)\boldsymbol{K}_{0,c}^e\big(\boldsymbol{D}(\boldsymbol{\sigma}_c^e)\big) \\ &= \Big(\big(\rho_c^e\big)^{\eta_t} + \rho_{\min}^e\Big)\int \boldsymbol{B}^{eT}\boldsymbol{D}(\boldsymbol{\sigma}_c^e)\boldsymbol{B}^e\, dV \end{aligned} \tag{4.5}$$

where $\boldsymbol{D}$ is the (stress-dependent) constitutive stiffness tensor relating continuum stresses $\boldsymbol{\sigma}_c$ and strains ϵ, and $\boldsymbol{B}^e$ is the elemental component of the standard strain displacement tensor ($\boldsymbol{\epsilon} = \boldsymbol{B}\boldsymbol{d}$). Note the constitutive stiffness tensor $\boldsymbol{D}$ is defined as follows for an isotropic material with Young's modulus E and Poisson's ratio ν:

$$\boldsymbol{D}_{\text{iso}} = \frac{E}{1-\nu^2}\begin{bmatrix} 1 & \nu & 0 \\ \nu & 1 & 0 \\ 0 & 0 & \frac{1-\nu}{2} \end{bmatrix} \tag{4.6}$$

The orthotropic material model of Darwin and Pecknold is stress-dependent and uses the following approximation for the stiffness tensor, denoted as $\boldsymbol{D}_p$ with the subscript 'p' indicating it is defined in the principal stress coordinate system:

$$\boldsymbol{D}_p = \begin{bmatrix} D_{11} & \nu_{\text{eff}} D_{11} D_{22} & 0 \\ \nu_{\text{eff}} D_{11} D_{22} & D_{22} & 0 \\ 0 & 0 & \frac{\left(D_{11}+D_{22}-\nu_{\text{eff}}\sqrt{D_{11}D_{22}}\right)}{4} \end{bmatrix} \tag{4.7}$$

where ν_{eff} is the effective, or smeared, Poisson's ratio, and D_{ij} terms are dependent on the principal normal stresses σ_{ci}, for $i = 1, 2$ as follows:

$$
\begin{aligned}
&D_{ii} = E_{ct}, \nu_i = \nu_{ct} \quad \text{for} \quad \sigma_{ci} > 0 \\
&D_{ii} = E_{cc}, \nu_i = \nu_{cc} \quad \text{for} \quad \sigma_{ci} < 0 \\
&D_{12} = D_{21} = \nu_{\text{eff}} \sqrt{D_{11} D_{22}} \\
&\nu_{\text{eff}} = \sqrt{\nu_1 \nu_2}
\end{aligned}
\tag{4.8}
$$

where E_{cc} and E_{ct} are the Young's modulus of the concrete in compression and tension, respectively, and ν_{cc} and ν_{ct} are the Poisson's ratio of the concrete in compression and tension, respectively. The compression Poisson's ratio of $\nu_{cc} = 0.2$ is used to compute the tensile Poisson's ratio from the following equation which is required to achieve symmetry of $\boldsymbol{D}_p$ (Darwin and Pecknold, 1977):

$$
\nu_{ct} = \nu_{cc} E_{ct} / E_{cc} \tag{4.9}
$$

This relation is deemed acceptable as the stiffness, and therefore load-carrying potential, of the concrete continuum system in tension is negligible.

The principal stresses σ_i in Eq. 4.8 and the orientation θ of the principal plane are computed in the standard manner

$$
\begin{aligned}
\sigma_{1,2} &= \frac{\sigma_x + \sigma_y}{2} \pm \sqrt{\left(\frac{\sigma_x + \sigma_y}{2}\right)^2 + \tau_{xy}^2} \\
\theta &= \frac{1}{2} \tan^{-1}\left(\frac{\sigma_x - \sigma_y}{2\tau_{xy}}\right)
\end{aligned}
\tag{4.10}
$$

where normal stresses σ_x and σ_y and shear stress τ_{xy} are all defined in the global

coordinate system.

The constitutive stiffness tensor in Eq. 4.7 defined in the principal coordinate system is then transformed to the global coordinate system using:

$$\boldsymbol{D} = \boldsymbol{Q}\boldsymbol{D}_p\boldsymbol{Q}^T \tag{4.11}$$

where the transformation tensor $\boldsymbol{Q}$ is defined as

$$\boldsymbol{Q} = \begin{bmatrix} \cos^2(\theta) & \sin^2(\theta) & 2\cos(\theta)sin(\theta) \\ \sin^2(\theta) & \cos^2(\theta) & -2\cos(\theta)sin(\theta) \\ -\cos(\theta)sin(\theta) & \cos(\theta)sin(\theta) & \cos^2(\theta) - \sin^2(\theta) \end{bmatrix} \tag{4.12}$$

4.4.3 Optimization formulation and solution algorithm

The hybrid minimum compliance problem can now be expressed as

$$\begin{aligned} \min_{\rho_t,\rho_c} \quad & f(\rho_t, \rho_c) = \boldsymbol{F}^T\boldsymbol{d} \\ \text{subject to:} \quad & \boldsymbol{K}(\boldsymbol{\rho}_t, \boldsymbol{\rho}_c, \boldsymbol{\sigma}_t, \boldsymbol{\sigma}_c)\boldsymbol{d} = \boldsymbol{F} \\ & \sum_{e\in\Omega_t} \rho_t^e v_t^e + \sum_{e\in\Omega_c} \rho_c^e v_c^e \leq V \\ & 0 \leq \rho_t^e \quad \forall\, e \in \Omega_t \\ & 0 \leq \rho_c^e \leq 1 \quad \forall\, e \in \Omega_c \end{aligned} \tag{4.13}$$

where ν_t^e and ν_c^e are the truss element lengths and continuum element volumes, respectively (as before), and the global stiffness matrix is assembled in the standard manner:

$$\boldsymbol{K}(\boldsymbol{\rho}_t, \boldsymbol{\rho}_c, \boldsymbol{\sigma}_t, \boldsymbol{\sigma}_c) = \underset{e \in \Omega_t}{\boldsymbol{A}} \boldsymbol{K}_t^e(\boldsymbol{\rho}_t^e, \boldsymbol{\sigma}_t^e) + \underset{e \in \Omega_c}{\boldsymbol{A}} \boldsymbol{K}_c^e(\boldsymbol{\rho}_c^e, \boldsymbol{\sigma}_c^e) \tag{4.14}$$

It should be noted that the standard projection scheme (Guest et al., 2011) is again used for the continuum elements and thus $\boldsymbol{\rho}_c$ remain a closed-form function of $\boldsymbol{\phi}$ as before. This detail is omitted for brevity.

One of the key aspects of this hybrid technique is that the concrete and steel "pull" from the same prescribed volume of material. Using this approach, if a structure sees only tension forces, the optimization process will yield a truss (steel) only structure. Likewise, if only compressive forces are present, a continuum (concrete) only structure will result, although this is unlikely due to the force spreading effect.

The equilibrium conditions are now governed by a nonlinear material model and thus require iterative numerical solution. However, they are bilinear elastic, meaning they are not load magnitude dependent and do not require load-stepping as in topology optimization for fully nonlinear material models such as in Swan and Kosaka (1997), Maute et al. (1998), and Amir and Bogomolny (2011). The approach taken here is to initialize the analysis iterative process with all elements being active and isotropic (no stress dependency) and updating the stiffnesses using the material models described above.

1. Initialize truss and continuum design variable fields $\boldsymbol{\rho}_t$ and $\boldsymbol{\rho}_c$ with uniform distribution of material (or random or educated guess).

2. Finite element analysis:

   (a) Solve linear elastic (stress-independent) problem $\boldsymbol{K}(\boldsymbol{\rho}_t, \boldsymbol{\rho}_c)\boldsymbol{d} = \boldsymbol{F}$ with truss elements having $E_t = 200$ GPa and all continuum elements being isotropic with $E_c = 24.9$ GPa (i.e., all elements at full stiffness).

   (b) Update truss element stiffness matrices according to Eq. 4.4

   (c) Update continuum element stiffness matrices according to Eq. (4.5, 4.7, 4.8, 4.9, 4.10, 4.11, 4.12).

   (d) Solve $\boldsymbol{K}(\boldsymbol{\rho}_t, \boldsymbol{\rho}_c, \boldsymbol{\sigma}_t, \boldsymbol{\sigma}_c)\boldsymbol{d} = \boldsymbol{F}$ with updated element stiffnesses.

   (e) If analysis converged, go to step 3; Else, go to step 2b.

3. Compute sensitivities using Eq. 4.3 and converged displacements and element stiffnesses from step (2).

4. Update the independent design variables using a gradient-based optimizer.

5. Check optimization convergence; if converged, stop; else go to step (2);

Convergence of the finite element analysis (Step 2e) is herein defined as less than 0.1% of truss elements changing between tension and compression states and the average change in orientation of the principal plane θ in non-void elements is less than 0.01 degree. Convergence was typically achieved in less than ten finite element iterations

in the presented examples. It should also be noted that the Young's moduli shown in Fig. 4.11 for each phase are piecewise linear and thus exhibit C^0, but not C^1, continuity. In gradient-based optimization, this typically requires interpolation between the piecewise states to achieve C^1 continuity. Interestingly, oscillatory behavior was not observed in either the analysis or optimization steps. This may be due to the fact that the design sensitivities (Eq. 4.3) are always negative, indicating that adding material always improves stiffness. Interpolation of Young's moduli, however, may be required for more challenging design problems where sensitivities may be positive or negative.

4.4.4 Hybrid strut-and-tie model results

The same examples presented above are solved using the new hybrid truss-continuum topology optimization approach using the embedded mesh scheme shown in Fig. 4.10. The compression block example (Fig. 4.9) highlights the capability of the model to capture force spreading. The optimal solution found using the hybrid topology optimization approach is shown in Fig. 4.12, where the white regions indicate non-load carrying concrete, the black region indicates (compression) load-carrying concrete, and lines indicate the steel ties. Under the compressive load (Fig. 4.12a), a single (large) compression strut is designed as before, however it is now reinforced with horizontal steel truss elements to capture principal tensile stresses that develop due to force spreading. This resembles splitting reinforcement that would be detailed in the

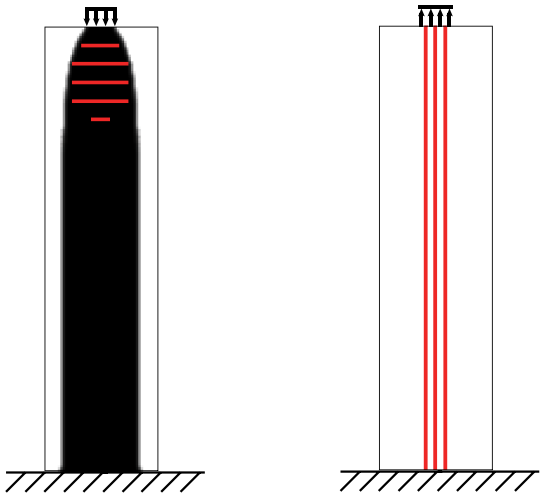

Figure 4.12: (a) Compression block solution found using the new hybrid topology optimization algorithm. The horizontal truss (steel) elements carry the tensile stresses due to force spreading seen in Fig. 4.9d. (b) Under a tensile applied load the algorithm produces a tie-only solution, illustrating that the hybrid scheme allocates material to tension (steel) and compression (concrete) constituents as needed.

local anchorage zone of a prestressing strand anchorage. It is also worth emphasizing that the volume constraint V is shared between the truss and continuum topologies in Problem (14). Fig. 4.12b highlights this idea: when the same structure is subjected to a tensile load the optimizer concentrates all available material in vertical steel ties, as the concrete does not play a role in force transfer.

Fig. 4.13 contains solutions to the previously explored examples found using the hybrid topology optimization algorithm. The compressive and tensile load paths are indicated by the continuum and truss topologies. The compressive load paths may take any angle, vary in thickness, and connect at any location, leveraging the free-form nature of continuum topology and the idea that these members are not explicitly constructed, but rather represent an idealized load path. The tension load

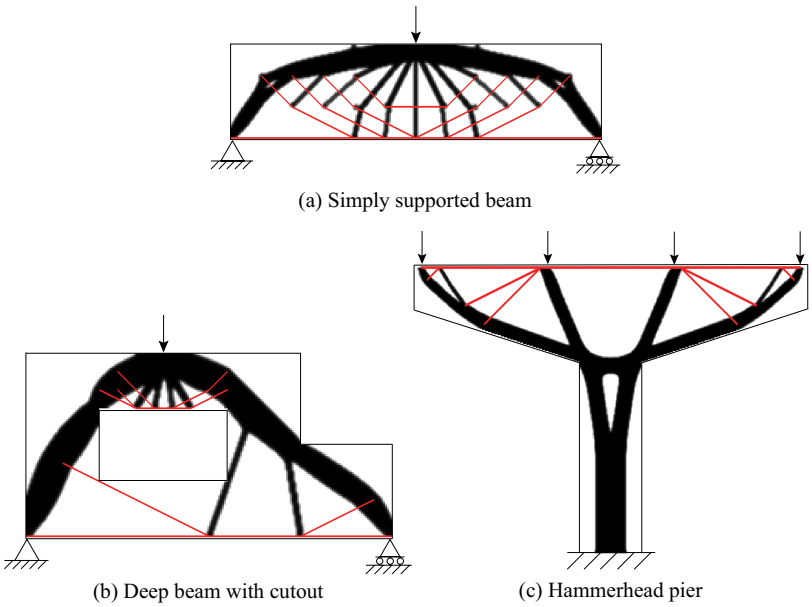

Figure 4.13: Optimized topologies found using the new hybrid optimization algorithm.

paths are straight and thus more accurately represent rebar and its placement. As truss members, they also allow for direct extraction of axial force and calculation of required cross-sectional areas in design.

The simply-supported beam (Fig. 4.13a) and hammerhead pier (Fig. 4.13c) solutions resemble a combination of the previously presented continuum-only and truss-only topology optimized solutions. The tension and compression load paths are orthogonal, with load transfer occurring at the end of the truss members, typically occurring in the interior of compressive struts. An interesting highlight of the deep beam with cutout solution (Fig. 4.13b) is the use of steel near the supports. In the truss-only topology optimization solution (Fig. 4.6c), unbraced compressive struts transfer load to the supports. In the hybrid model, lateral truss members are present

in the region of the support to pick up the tensile stresses that will develop due to force spreading at bearing. This more closely resembles the continuum solution (Fig. 4.6b), although an extra tie has been added to the lower right of the domain to pick up tensile stresses developing due to a change in thickness of the compression strut in this region

4.5 Strut-and-Tie Concluding Remarks

Topology optimization provides an effective and convenient methodology for obtaining a minimum compliance concrete truss model, i.e., a truss model where the strain energy is minimized, a generally agreed upon design guideline which is intended to minimize plastic deformation at an ultimate limit state. Experiments and nonlinear finite element modeling have confirmed that a minimum compliance concrete truss model can increase peak load and improve the load-deformation response of reinforced concrete members over traditional strut-and-tie designs. However, as only elastic stiffness is considered rigorously in the optimization formulation, a designer must still check ductility and strength requirements of the selected strut-and-tie model with existing code provisions. The minimum compliance design problem is efficiently solved using gradient-based optimizers with adjoint sensitivity analysis, enabling identification of models for complex domains, including members with holes. Results are shown to produce steel reinforcement patterns that are in line with the

principal tension elastic stress trajectories.

The advantages of truss topology optimization are that steel ties are discrete and straight, yielding realistic and constructible reinforcement patterns, and that axial force demand and therefore required steel cross-sectional areas come directly out of the analysis. The disadvantages are that the optimality is limited by the initial choice of ground structure, with simpler ground structures yielding simpler, but less efficient, topologies. Conversely, the free-form nature of continuum topology optimization typically enables discovery of solutions with higher efficiency. These solutions, however, tend to be more complex, potentially requiring curved rebar or rebar with varying thickness. The number of required ties, however, may be indirectly limited through the use of projection schemes for controlling minimum length scale as shown in the hammerhead pier design problem. Continuum solutions must also be post-processed to determine required steel areas. Neither truss or continuum topology optimization is capable of accounting for transverse tensile stresses that may develop in compression members due to force spreading.

The key contribution of this work is the development of a hybrid truss-continuum topology optimization methodology that can help designers understand the flow of forces in a reinforced concrete member and provide demand forces that can be used to size reinforcing steel. Bilinear material models are used to find tensile load paths represented by truss (steel) elements and compressive load paths by continuum (load-carrying concrete) elements. Rebar is therefore kept discrete and placed in straight

segments, with axial force demand directly output by the model, while the concrete load path is free to take any shape. An orthotropic bilinear material model is assumed for the concrete, requiring tensile principal stresses to be carried by the steel truss members. This is shown to capture force spreading phenomena that traditional topology optimization approaches miss, particularly at locations of concentrated forces, such as applied loads, bearing at supports, and prestressing anchorages.

With the ability to algorithmically focus natural tension and compression force flow in separate structural elements comes the potential to increase complexity of the design objectives beyond elastic stiffness and directly optimize for serviceability and strength in reinforced concrete. Very recently, Amir and Bogomolny (2011) have provided an excellent first step in this direction by optimizing for strength with elastoplastic continuum damage models. As shown, the proposed hybrid approach allows different constitutive models to be used for the steel and concrete, which could include different yield and hardening behaviors, and potentially be extended to design for ductility. The proposed approach may also be extended to other composite material systems with constituents having different properties in tension and compression.

4.6 Future Directions: Potential for Application to Additive Manufacturing

As can be seen from this algorithm, it can design for material which performs very well in either tension or compression. It also demonstrates great ability to design not only a continuous phase but a more discrete truss phase, which may mimic the placement of stiffeners or actuators in the printing process. This algorithm may be adapted in the future to design for additive manufacturing methods in which the material has an anisotropic grain-like structure. These types of built structures are especially prevalent in parts manufactured by Fused Deposition Modeling. Also, in the case of ceramic additive manufacturing, the stress-dependent concrete model - high modulus in compression and low modulus in tension - may be a good fit.

While 3D printers with the ability of placing discrete objects are not yet commercially available, it is prudent to develop design methods so that the technology may be fully exploited when it matures. There exists a great potential to create such objects as actuated prosthetics in a single build process allowing the for manufacture of a custom hand, foot, etc. This customizability is essential for such objects and is a perfect fit for additive manufacturing technology.

Chapter 5

Conclusions and Future Work

In the past chapters, a number of additive manufacturing design problems were presented and solved using topology optimization as the design engine. Contrary to popular belief, there are, in fact, limits on what can and cannot be printed. Each chapter considered one identified limitation or ability of a particular additive manufacturing technology or additive manufacturing in general. In the case of the multi-material 3D printer, a compliant mechanism was designed and printed and was found to perform much better than the typical single material compliant mechanism. In the second chapter, we explore the possibility of eliminating support material from additively manufactured parts by incorporating a maximum achievable non-supported overhang angle into the optimization formulation. The optimized topologies in some cases differed fairly drastically from the traditional topology optimization solutions, but showed good agreement with the imposed angle constraint. Finally, a method

was developed for an additive manufacturing technique that has yet become fully developed - the insertion of discrete objects during the printing process such that they are encapsulated in the 3D printed material matrix.

Looking forward, there are a number design considerations which have yet to be explored. When using topology optimization in 3D, It is common to obtain solutions that contain internal voids. Unfortunately, for many additive manufacturing methods such as FDM and SLM, internal voids are not ideal and can result in poor performance. In both cases, support material for FDM and non-melted metal powder for SLM in this internal void cannot be accessible post-print, therefore adding additional weight to the final built part. Therefore, future work should focus on producing topology optimization solutions which contain no internal pores, essentially always creating a way for the support material and metal powder to 'escape' the part.

Aside from the overhang constraint and the internal void constraint, additive manufacturing methods do possess many more obvious geometric constraints. It is for this precise reason that additive manufacturing and topology optimization pair so well. The primary unresolved issues with additively manufactured parts focus on the material characteristics. Since it is a relatively new technology, precise material properties are relatively unknown for parts manufactured in this layer-by-layer manner. It is highly unlikely that a part manufactured by both AM and by a more traditional method will have the same performance. Once these material properties are quantified, they can be incorporated into the topology optimization design formulation -

whether it's material anisotropy or stochasticity of the constitutive properties.

Related to the anisotropic nature of most material in additively manufactured parts, an area of interest is optimizing the part orientation during the build process. It may be the case that a part will have significantly better performance if built in a particular orientation, stemming from the almost wood-like grain apparent in many FDM manufactured parts. For example, if a tension test coupon is created via 3D printing, it is likely that if the strands of the part are oriented along the length of the coupon in the direction of the applied load as opposed to perpendicular, much greater performance metrics may be achieved. Some researchers have looked at picking the best orientation, however no rigorous optimization was applied to choose the best orientation.

Finally, attributing to the slow nature of additive manufacturing, it is proposed to use 3D printing to manufacture the mold for a cast part. In this way, many of the new design freedoms still exist, but the slow additive process will only have to be performed once. After making the mold, parts will be able to be manufactured in a small fraction of the AM required time. This design paradigm will require topology optimization formulations to essentially design the 'negative' of the designed part. By tackling this problem, the previous specialty part and high-tech only limitation of additive manufacturing will become a thing of the past, opening up the possibility of additive technologies to move towards mainstream consumer level parts.

Appendix A

A Gradient-based Approach to Truss Topology Optimization with Integer Design Variable Constraints

A.1 Introduction

Truss optimization has been around for more than twenty years and thus has been approached by a plethora of methods. As mentioned in an early work by Achtziger et al. (1992), truss optimization problems are typically formulated as a sizing optimization with the design domain "discretized" into an initial ground structure given

certain boundary conditions and loads. The optimization is formulated as a continuous optimization in which the design variables are the cross sectional areas of the truss members. Evenly distributing the material as the initial guess, the optimization then runs allowing the cross sectional areas to continuously vary from zero to some upper bound, yielding the optimal cross sectional area for each truss members. Bendsøe's review paper (Bendsøe et al., 1994) identifies some of the early methods used to optimize these continuous design variable ground structure problems.

Still, other methods did not operate on a fixed ground structure, but instead included the nodal location as design variables in addition to the cross sectional areas (Kirsch, 1989). Sigmund optimized truss structures to tailor for prescribed elastic properties (Sigmund, 1995). In this paper, the microstructures were optimized to match the theoretical limits of Poisson's Ratio (-1 and 0.5).

While continuous design variable optimization of truss structures is computationally inexpensive – due to the existence of gradient information – the solutions often require significant post-processing to produce the final built design. When designing a building such as a truss bridge or sky scraper, the designer must choose from a "library" of allowable standardized truss members. Since intermediate truss sizes are not allowed (or are prohibitively expensive), the optimization problem turns into a discrete optimization problem. With that transformation from continuous to discrete optimization, the computational cost increases drastically, as gradient based optimizers are no longer an option.

A.1.1 Current state of discrete truss opt

Discrete optimization is known to be a difficult problem and, as such, can be computationally expensive. Globally optimal results are only obtainable for relatively small-sized problems. A few globally convergent enumeration algorithms include the Branch-and-Bound optimization algorithm (Achtziger and Stolpe, 2007) and the Cut-and-Branch algorithm (Rasmussen and Stolpe, 2008). While globally convergent, (Achtziger and Stolpe, 2007) showed that a problem size of 632 design variables takes on the order of three days to solve using a typical computer, making the optimization expensive. Furthermore, there may exist situations when the engineer is interested in performing optimizations on many thousands of design variables. In this situation, globally convergent algorithms are prohibitively expensive.

While these methods are proven, the most popular of the available discrete methods are the stochastic search algorithms. There are a plethora of these heuristic optimization methods – so many that they cannot all be named – from genetic algorithms, which mimic the process of natural selection (Deb and Gulati, 2001; Ghasemi et al., 1999; Hajela and Lee, 1995; Rajan, 1995; Rajeev and Krishnamoorthy, 1997), to Ant Colony optimization (Camp and Bichon, 2004), to shape annealing, a method which mimics a physical process (Reddy and Cagan, 1995). Another method, neural networks optimization, was inspired by the central nervous system and uses machine learning to recognize patterns to obtain the optimal truss structure (Adeli and Park, 1995). While the majority of these methods yield decent results, they do not guar-

antee a globally optimal result. The methods are, however, easy to implement and are conceptually logical and interesting. Another approach sometimes used is the rounding technique, as found in (Groenwold et al., 1996). While this method will produce decent solutions, the algorithm uses heuristics, making it less desirable.

There exist some methods which span the gap between stochastic search algorithms, globally convergent algorithms and continuously differentiable algorithms. These evolutionary structural optimization (ESO) methods, while heuristic, use physical properties of the truss (usually strain energy density) in order to progress the optimization in a desirable direction (Kwak and Noh, 2006; Tanskanen, 2002).

It is seen that the established approaches have advantages and disadvantages. In general, there is a tradeoff between speed and optimality. The globally convergent algorithms are guaranteed to produce the global optimum, but are extremely computationally expensive, while the stochastic search algorithms are both computationally expensive and do no guarantee any degree of optimality. They stochastic search algorithms are, however, easy to implement and produce decent solutions. As of now, it appears there is no way to get the best of both worlds – an algorithm which can produce optimal solutions in an time efficient manner.

A.1.2 Topology optimization background and formulation

Topology optimization problems are typically formulated as maximizing stiffness, or equivalently, minimizing compliance, subject to a material volume constraint. This is represented in the following formulation:

$$\begin{aligned} \min_{\boldsymbol{\rho}} \quad & f(\boldsymbol{\rho}) = \boldsymbol{F}^T \boldsymbol{d} \\ \text{subject to:} \quad & \boldsymbol{K}(\boldsymbol{\rho})\boldsymbol{d} = \boldsymbol{F} \\ & \sum_{e \in 1} \rho^e v^e \leq V \\ & 0 \leq \rho^e \leq \rho^e_{\max} \quad \forall\, e \in \Omega \end{aligned} \tag{A.1}$$

where design variable vector $\boldsymbol{\rho}$ is the set of material densities for the structure, ρ^e is material concentration in element e, $\boldsymbol{F}$ are the applied nodal loads, $\boldsymbol{d}$ are the nodal displacements, v^e is element volume for unit ρ^e (element length for truss structures), V is the available volume of material, and $\rho^e_{\max}$ is the design variable upper bound. The global stiffness matrix $\boldsymbol{K}$ is assembled ($\boldsymbol{A}$) from element stiffness matrices $\boldsymbol{K}^e$ as follows:

$$\begin{aligned} K(\boldsymbol{\rho}) &= \underset{e \in \Omega}{\boldsymbol{A}} \boldsymbol{K}^e(\rho^e) \\ \boldsymbol{K}^e(\rho^e) &= \rho^e \boldsymbol{K}^e_0 \end{aligned} \tag{A.2}$$

where $\boldsymbol{A}_{e \in \Omega}$ designates an assembly of the elemental stiffness matrices $\boldsymbol{K}^e(\rho^e)$. The

elemental stiffness matrixes are formulated as a product of the design variables, ρ^e, and unit stiffness of each element, $\boldsymbol{K}_0^e$. Typically $\boldsymbol{K}_0^e$ is formulated for an area of unity and ρ^e are then equivalent to to the cross sectional area of the element.

Another typical formulation, minimum weight design, is a slight variation on the previous formulation in which the weight of the structure is minimized subject to some deflection (compliance) constraint. Essentially, the objective function and constraint function from Eq. A.1 are interchanged. The minimum weight formulation appears as follows:

$$\begin{aligned} \min_{\boldsymbol{\rho}} \quad & W = \sum_{e \in 1} \rho^e v^e \\ \text{subject to:} \quad & \boldsymbol{K}(\boldsymbol{\rho})\boldsymbol{d} = \boldsymbol{F} \\ & \boldsymbol{L}^T \boldsymbol{d} \leq \boldsymbol{L}^T \boldsymbol{d}_{\text{allowed}} \quad \forall\, 1, N \\ & 0 \leq \rho^e \leq \rho^e_{\max} \quad \forall\, e \in \Omega \end{aligned} \tag{A.3}$$

where the objective function, W, is the weight, $\boldsymbol{d}_{\text{allowed}}$ is the allowed displacement, $\boldsymbol{L}$ is a vector of zeros with ones placed at the degrees of freedom where the displacement is constrained, and the additional variables are defined above. The formulation seen in Eq. A.3 is more applicable to the field of structural engineering, as a design engineer may know the maximum allowable deflection, but will have no intuition as to what volume fraction should be set (as in Eq. A.1) to get the desired performance.

As formulated above in Eq. A.1 and Eq. A.3, the optimization problem is posed as a continuous problem. As a result, the solutions will contain member of any cross

sectional area within the design constraints of $0 \leq \rho^e \leq \rho^e_{\max}$. However, when designing a structure using truss members, the designer is almost always required to choose from a "library" of allowed cross sections. Hence, the problem is, in fact, not a continuous optimization problem, but a discrete optimization problem. As stated above, these problems often take days to solve on a typical computer and, additionally, the size of the problem is severely limited by the both the stochastic search optimization and global optimization methods. This paper proposes an alternative method which yields discrete values, yet allows the design variables to vary continuously. The algorithm can therefore take advantage of gradient information, thus producing final solution in an efficient manner. The method is outlined in coming sections. First, discrete truss optimization is formulated.

A.1.3 Discrete truss optimization formulation

Although structural engineers would be more interested in a minimum weight optimization, this paper will focus on minimum compliance so that the results are more readily comparable to other methods, especially the globally optimal results identified in Achtziger and Stolpe (2007). Minimum compliance, discrete truss optimization takes on the following form, which differs only slightly from the continuous optimization case in Eq. A.1:

APPENDIX A. A GRADIENT-BASED APPROACH TO TRUSS TOPOLOGY OPTIMIZATION WITH INTEGER DESIGN VARIABLE CONSTRAINTS

$$\begin{aligned} \min_{\boldsymbol{A}} \quad & f(\boldsymbol{A}) = \boldsymbol{L}^T \boldsymbol{d}_{\text{allowed}} \\ \text{subject to:} \quad & \boldsymbol{K}(\boldsymbol{A})\boldsymbol{d} = \boldsymbol{F} \\ & \sum_{e \in 1} A^e v^e \leq V \\ & A^e = A_i, \quad \text{where } A_i = \text{discrete values} \end{aligned} \tag{A.4}$$

Notice that the cross sectional areas must now be chosen from a database of allowable cross sections, A_i. Intermediate values, those which lie between the specified A_i are no longer allowed. Established methods are often slow due to the lack of derivative information to drive the optimization steps. It is for this reason that continuous optimization techniques are so attractive. As mentioned above, the common approaches to work around this issue is to use stochastic search optimization techniques, which require no derivatives but often yield excellent results (Adeli and Park, 1995; Camp and Bichon, 2004; Deb and Gulati, 2001; Ghasemi et al., 1999; Hajela and Lee, 1995; Rajan, 1995; Rajeev and Krishnamoorthy, 1997; Reddy and Cagan, 1995), use rounding techniques (Groenwold et al., 1996), or to relax the discrete variable to a continuous variable and somehow force the result to discrete values (Achtziger and Stolpe, 2007; Rasmussen and Stolpe, 2008).

A.2 Uniform Discrete Truss Optimization

A new method is proposed which attempts to drive towards discrete valued solutions while taking advantage of gradient information. The method is first applied to the "uniform discrete" case. "Uniform discrete" implies that the final cross-sectional areas of each truss member may take on values of uniform increment such as $[0, 1, 2, 3, 4, 5]$ or $[0, 0.2, 0.4, 0.6, 0.8, 1.0]$. To produce uniform discrete values of truss cross-sectional areas in the final design, a small variation of the previous continuous method is implemented.

The key to attaining discrete results from continuous design variables is to assign multiple design variables to each truss cross-section. The overall area of each truss member then becomes a summation over the design variables.

$$\rho^e = \sum_{i=1}^{n} \phi_i^e \Delta A \tag{A.5}$$

where ρ^e is the total cross-sectional area of the truss member, which is a summation of the 0-1 design variables ϕ_i^e multiplied by some constant area increment ΔA. In this scheme, the areas may take on any increment of ΔA, from $(0 * \Delta A)$ up to $(n * \Delta A)$. In the above example, ΔA equals 1 and 0.2 respectively.

This method borrows the Solid Isotropic Material with Penalization (SIMP) method common to continuum topology optimization (Eq. A.6). Each design variable ϕ_i^e is driven to 0 or 1 using SIMP. This makes design variables of intermediate volume

fraction inefficient, therefore producing solutions limited to the predefined discrete increments of ΔA. Eq. A.7 illustrates how the global stiffness matrix, $K(\boldsymbol{\rho})$, is now defined.

$$\begin{aligned} \rho^e_{\text{stiffness}} &= \sum_{i=1}^{n} (\phi^e_i)^{\eta_i} \Delta A \\ \eta_i &= \eta_0 + i\Delta\eta \end{aligned} \tag{A.6}$$

$$\begin{aligned} \boldsymbol{K}(\boldsymbol{\rho}) &= \underset{e\in\Omega}{\boldsymbol{A}} \boldsymbol{K}^e(\rho^e) \\ \boldsymbol{K}^e(\rho^e) &= \rho^e_{\text{stiffness}} \boldsymbol{K}^e_0 \end{aligned} \tag{A.7}$$

where η_i is the SIMP exponent associated with each design variable i. Slightly varying values of the exponent are needed because if each design variable is forced to 0-1 using the same exponent penalty, η, and all ϕ^e_i are initialized to the same volume fraction, there will be no difference in the design variable sensitivities. In this case, the optimizer used for all solutions, the Method of Moving Asymptotes (Svanberg, 1987), cannot decipher among the different groups. Therefore, it is proposed to use a slightly different value of the exponent for each group i. It was found that differing the η by as small as 0.001 worked well. To clarify, if there are five design variables per element with $\eta_0 = 3$ and $\Delta\eta = 0.001$, the eta's take the form $\eta_i = [3, 3.001, 3.002, 3.003, 3.004]$. Alternatively, all exponents, η_i may be equivalent but instead use slightly different initial values of ϕ_i for each group. Using this approach and an $\Delta A = 1$, the allowable final truss cross-sectional areas are $[0, 1, 2, 3, 4, \text{or } 5]$.

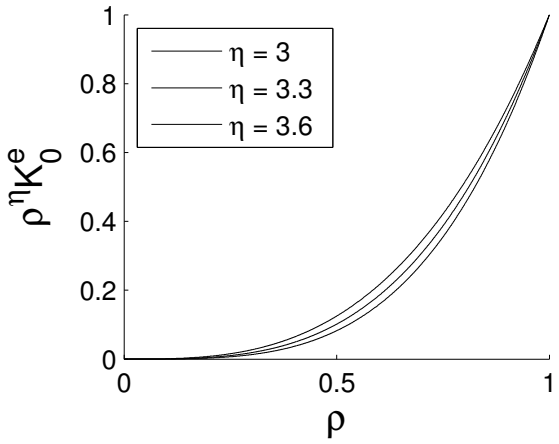

Figure A.1: varying values of exponent η

Fig. A.1 shows the effect of the proposed SIMP method. The small difference in the formulation of the stiffness matrix results in different gradient values for each ϕ_i^e at a particular value of ϕ. Here, a larger than necessary $\Delta\eta = 0.3$ is shown so that the difference between curves is obvious.

The final formulation takes on the following form:

$$\begin{aligned} \min_{\boldsymbol{\phi}} \quad & \boldsymbol{L}^T\boldsymbol{d} \\ \text{subject to:} \quad & \boldsymbol{K}(\boldsymbol{\rho})\boldsymbol{d} = \boldsymbol{F} \\ & \rho^e(\boldsymbol{\phi}, \Delta A_i)v^e \leq V \\ & 0 \leq \phi_i^e \leq \phi_{\max}^e \quad \forall\, e \in \Omega \end{aligned} \tag{A.8}$$

A.2.1 Simple tension test case

To help illustrate how this method works, take this simple test case. Figure A.2 presents the test case where the optimization starts with an initial ground structure

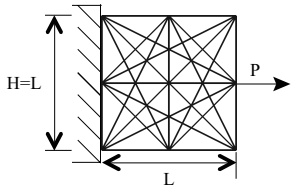

Figure A.2: Simple tension case. Initial ground structure with 28 bars. $H = L = 2$.

containing 28 truss members. Here $L = H = 2$.

Optimized as a minimum compliance problem (as in Eq A.1) and given a total allowable volume of 7 it would yield 2 bars, each with a cross-sectional area of 3.5. However, when optimized according to Eq. A.2, non-integer intermediate values are undesirable due to the SIMP penalty.

Notice that three design variables go to one for the bar 1 and 4 design variables go to one for bar 2. In Fig. A.3, the areas from Fig. A.3c are summed to get the total areas seen in Fig. A.3b – bar one has an area of three and bar two has an area of four. The red lines in Fig. A.3b indicate the "allowable" cross sectional areas.

A.2.2 Test Cases

With a the simple example working well (Fig. A.3) it is now necessary to test the algorithm on larger problems to test its robustness. As identified in the paper by Achtziger and Stolpe (Achtziger and Stolpe, 2007), the following benchmark problems are known to be good test cases.

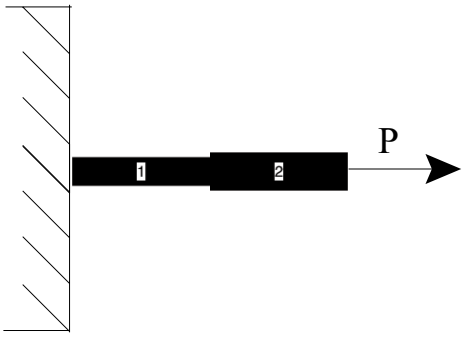

a Solution

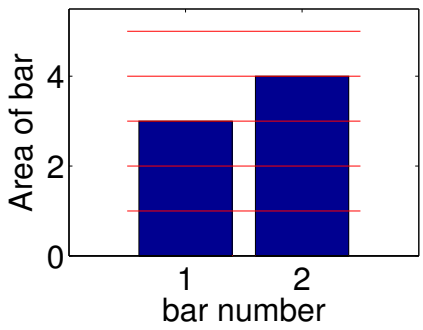

b Final bar areas

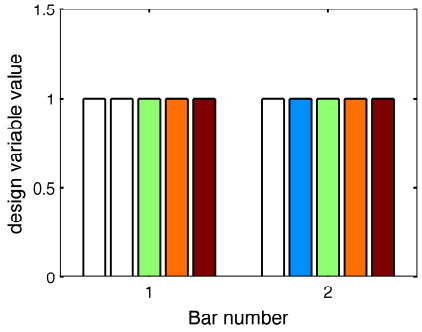

c Green indicates allowable overhang while yellow indicates a violation of the overhang rule.

Figure A.3: Simple tension example optimization results.

A.2.2.1 Michell Beam

The Michell Beam, as seen in Fig. A.4, is a cantilever beam supported over half its height along the left side of the domain. A load is applied on the right side at the halfway point. The ground structure (Fig. A.4b) has 9 nodes in the x direction ($x_{\text{nodes}} = 9$) and 5 nodes in the y direction ($y_{\text{nodes}} = 5$) with a total of 632 initial bar members.

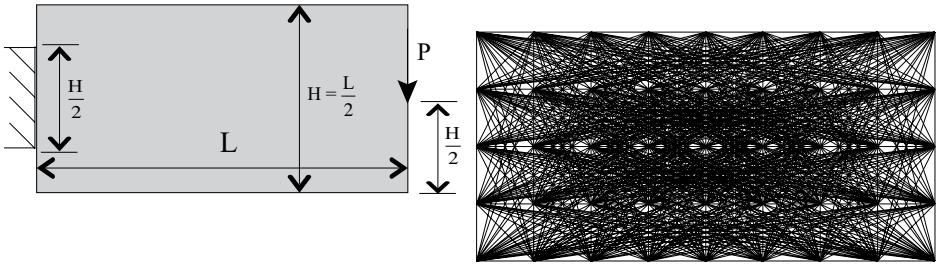

a Problem definition **b** Ground Structure

Figure A.4: Michell beam

A.2.2.2 Single-load short bridge

The single-load short bridge, as seen in Fig. A.5 is a short span bridge with 4 evenly spaced equal magnitude loads. The ground structure (Fig. A.5b) has $x_{\text{nodes}} = 6$ and $y_{\text{nodes}} = 4$ for a total of 188 initial bar members.

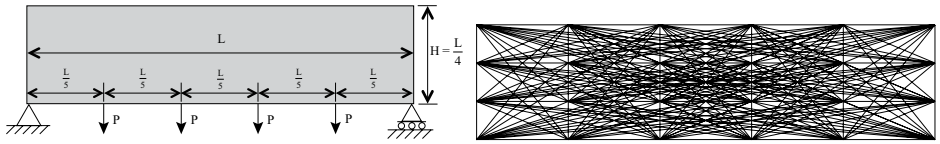

a Problem definition **b** Ground Structure

Figure A.5: Single-load short bridge

A.2.2.3 A single-load wheel

The single-load short wheel, as seen in Fig. A.6 is simply supported domain with one downward load on the bottom center of the span.The ground structure (Fig. A.6b) has $x_{\text{nodes}} = 5$ and $y_{\text{nodes}} = 5$ for a total of 200 initial bar members.

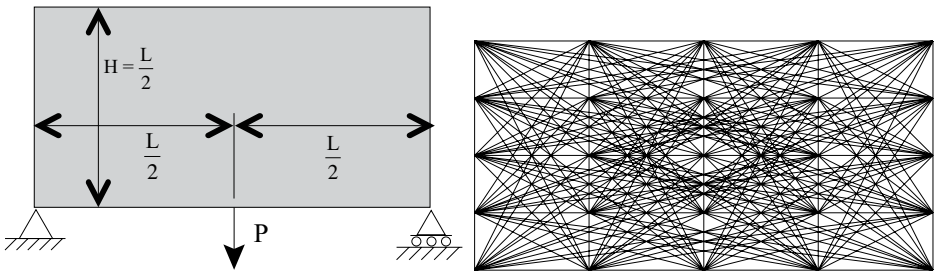

a Problem definition **b** Ground Structure

Figure A.6: Wheel Problem

A.2.2.4 A single-load cantilever

The single-load cantilever, as seen in Fig. A.7 is pin supported on the left and center bottom of the domain with one downward load on the bottom right of the span.The ground structure (Fig. A.7b) has $x_{\text{nodes}} = 5$ and $y_{\text{nodes}} = 5$ for a total of 200 initial bar members.

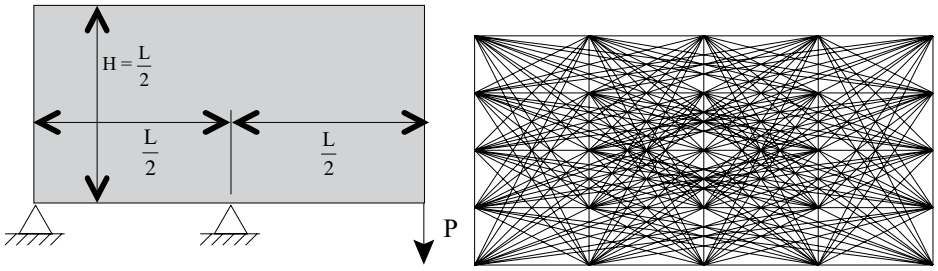

a Problem definition **b** Ground Structure

Figure A.7: Single load cantilever

A.2.2.5 MBB beam with many design variables

The MBB beam, while not a benchmark problem identified by Stolpe, is always a good test case for topology optimization, since the user can intuitively evaluate the quality of result. As seen in Fig. A.8, the MBB beam is simply supported domain with

one downward load on the top center of the span.The ground structure (Fig. A.8b) has $x_{\text{nodes}} = 15$ and $y_{\text{nodes}} = 8$ for a total of 4921 initial bar members. The purpose of solving this example is to illustrate the efficiency inherent in the algorithm. Such an example would be prohibitively large to solve using heuristic or global optimization (e.g. Branch and Bound) methods.

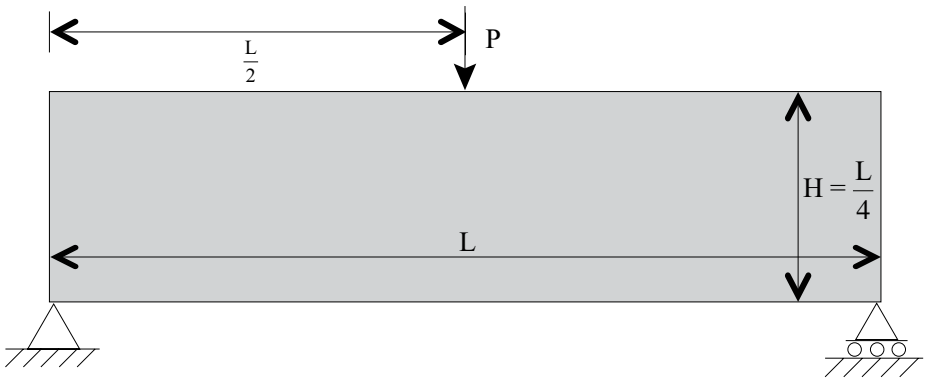

a Problem definition

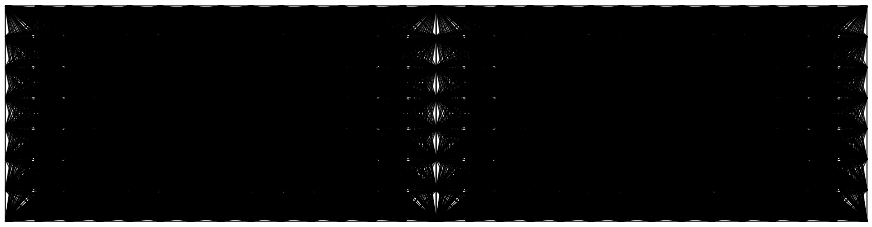

b Ground Structure

Figure A.8: MBB beam

A.2.3 Solutions

Test cases in Figs. (A.4, A.5, A.6, A.7, A.8) were all run with a continuation method in which the initial optimization was run with an exponent, η, of one for 50 iterations. The result of that optimization was then used as the initial design for a

second optimization that was run with an exponent of two.

Table A.2.3 summarizes the results in comparison with the globally optimal compliance, C, found by Achtziger and Stolpe.

Test Case	η	C_{SIMP}	C_{global}
Stolpe 1	2	9.39	8.96
Stolpe 2	2	10.67	10.56
Stolpe 3	2	0.28	0.28
Stolpe 4	2	0.98	0.94

In nearly all cases, except for Fig. A.10, a few cross sectional areas are not driven to discrete values. The intermediate values are present due to the formulation. While most are driven to discrete values, depending on the specified volume constraint, there will almost always be one member that contains an intermediate value. This is because, for minimum compliance case, the algorithm will always add material to drive down the objective function, even if the addition of material is not very efficient due to the SIMP penalty. This is a flaw which cannot be eliminated, but is not a huge problem. The few elements in the intermediate regime can simply be rounded up to the next cross section size (via post processing), so as to design on the conservative side. It is argued, that, while not ideal, the extremely fast speed at which these solutions are obtained greatly outweighs the issue.

The MBB beam, in Fig. A.13 completed the optimization in a surprising short

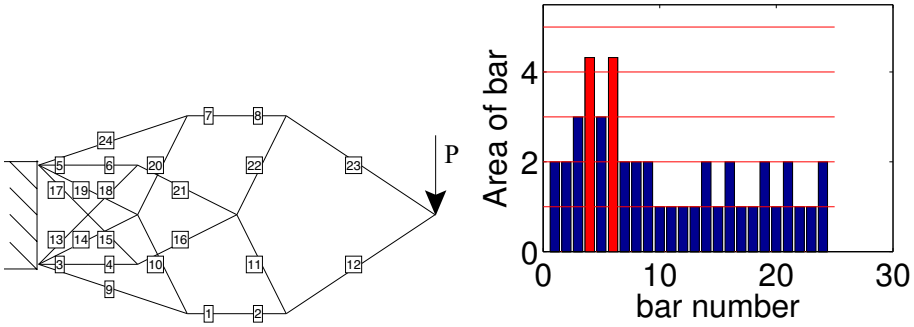

a Optimized Topology **b** Bar Areas

Figure A.9: Single load Michell Beam Results

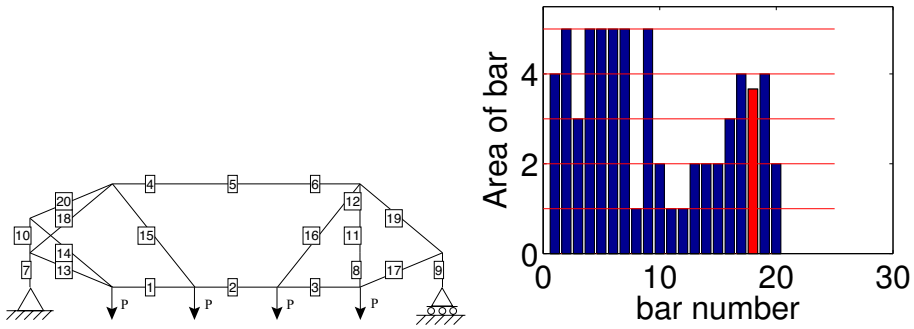

a Optimized Topology **b** Bar Areas

Figure A.10: Bridge Results

amount of time. The algorithm proposed in this paper solves the problem in 205 seconds yielding a near uniform discrete final topology. The MBB beam in Fig. A.13 has 24605 design variables (4921 truss elements). A problem of this size cannot be solved in a reasonable amount of time using either Branch and Bound or stochastic search type algorithms.

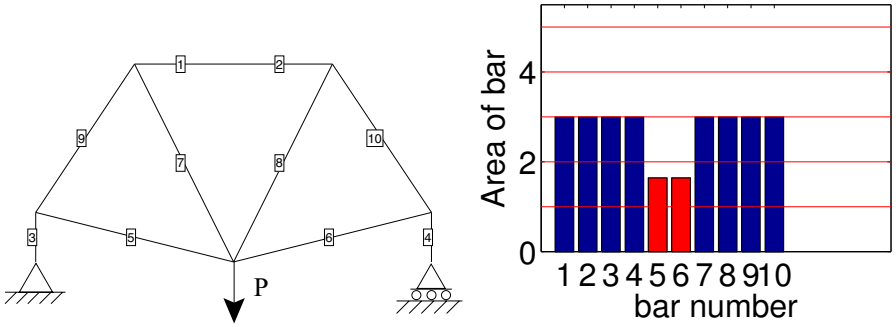

a Optimized Topology **b** Bar Areas

Figure A.11: Wheel Results

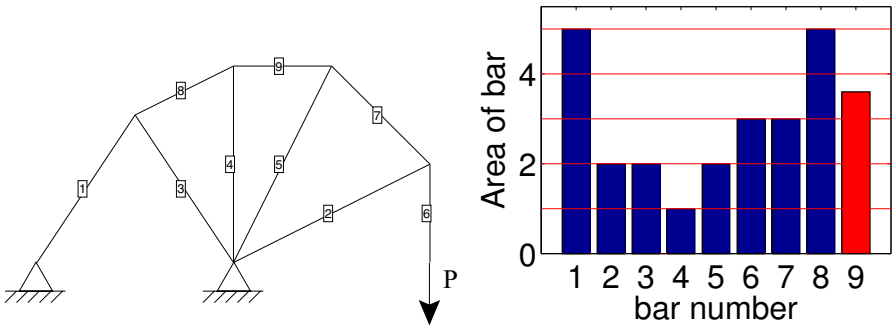

a Optimized Topology **b** Bar Areas

Figure A.12: Single load cantilever Results

A.3 Test with simple ground structure

Here the algorithm is tested again with the Michell Beam and the single load bridge structures (see Fig. A.15 and Fig. A.16), but this time run using the most simple of ground structures (Figs. A.14a and A.14b). These are included to show that the algorithm succeeds even when it must choose a more complicated load path. By looking at the results in Fig. A.15 and Fig. A.16, it can be seen that the algorithm performs exactly as expected. This shows that the proposed method not only works

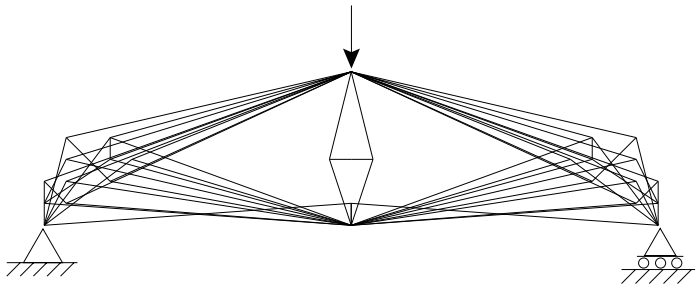

a Optimized Topology

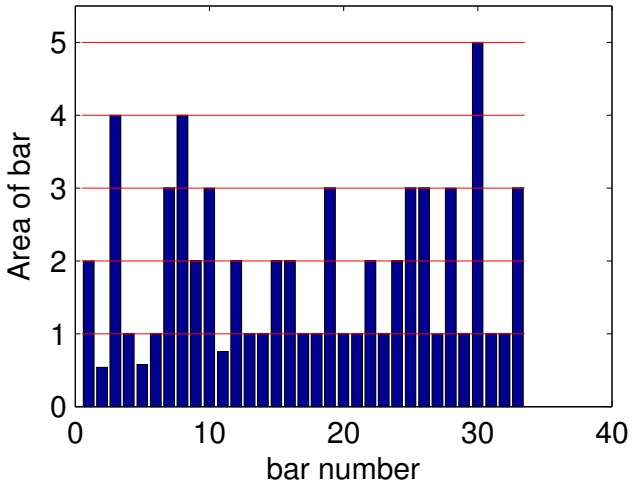

b Bar Areas

Figure A.13: Single load cantilever Results

for very large problems as in see Fig. A.13, but in small test cases as well.

A.4 Non-uniform discrete truss optimization

In this section, the integer truss optimization is expanded to general discrete truss optimization. The new formulation is a slight revision of the formulation in the

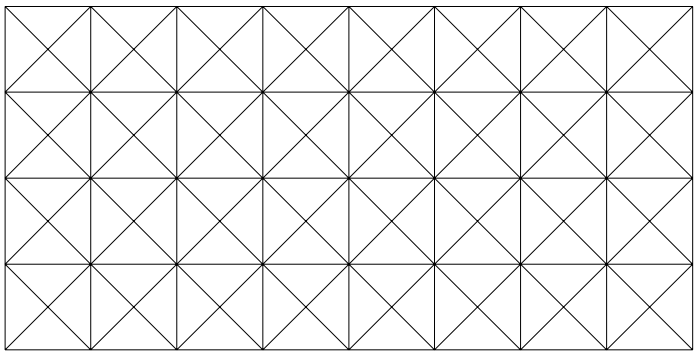

a Simple GS Michell Beam

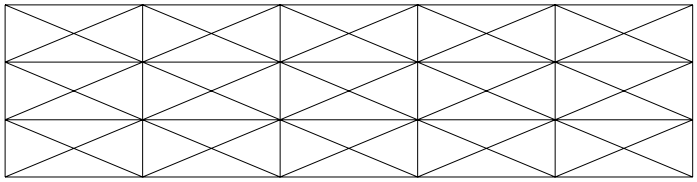

b Simple GS bridge single load case

Figure A.14: Simple ground structures

previous section. Introduced now are increments of the areas, which we will call ΔA_i. The increments are ordered in such a way that if each design variable i is forced to 1 in a certain order, then the desired allowable areas will result. The desired allowable areas are a cumulative summation of the A. For example, if the allowable areas are $[1, 1.5, 3, 5, 9]$, then $\Delta A = [1, 0.5, 1.5, 2, 4]$.

Obviously, this approach requires the design variables, i, to "turn on" in a certain order. To accomplish this, a simple rule on the initial starting point is enforced. Assuming the sensitivities remain negative (no inverter problem), the MMA will force the design variables with higher magnitude to 1 before those of lower magnitude. It is seen below, in which ρ_i is now a function of the design variable ϕ_i.

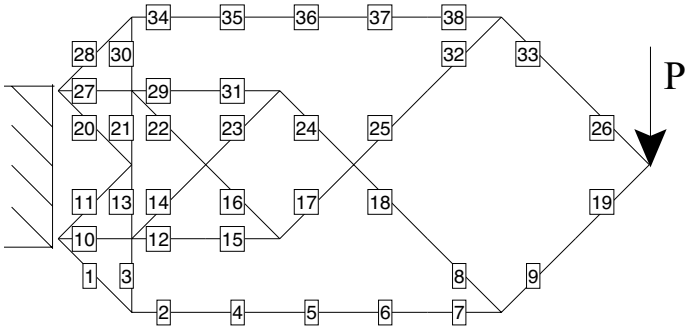

a Optimized Topology

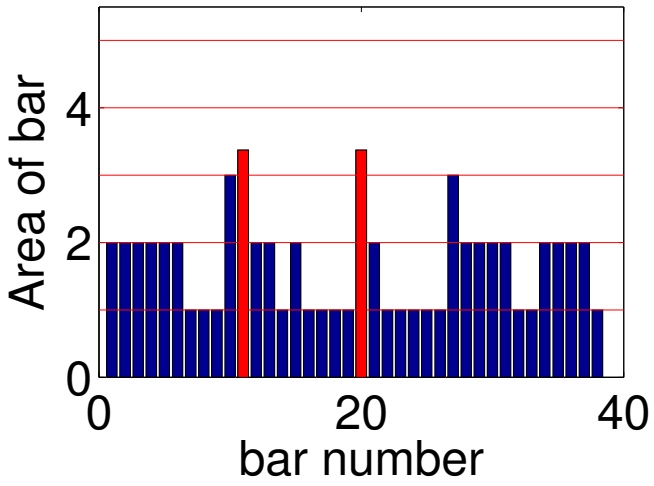

b Bar Areas

Figure A.15: Simple GS Cantilever Beam Result

$$\rho^e_{\text{stiffness}} = \sum_{i=1}^{n} (\phi^e_i)^\eta \Delta A$$
$$\phi_i = \phi_0 + i\Delta\phi \tag{A.9}$$

$$\rho^e_{\text{stiffness}} = \sum_{i=1}^{n} (\phi^e_i)^\eta \Delta A_i$$
$$\phi_i = \phi_0 + \Delta\phi_i \tag{A.10}$$

This is seen in Fig. A.17. Having a higher starting value on the SIMP curve results

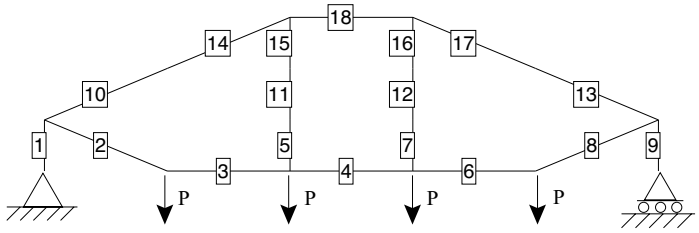

a Optimized Topology

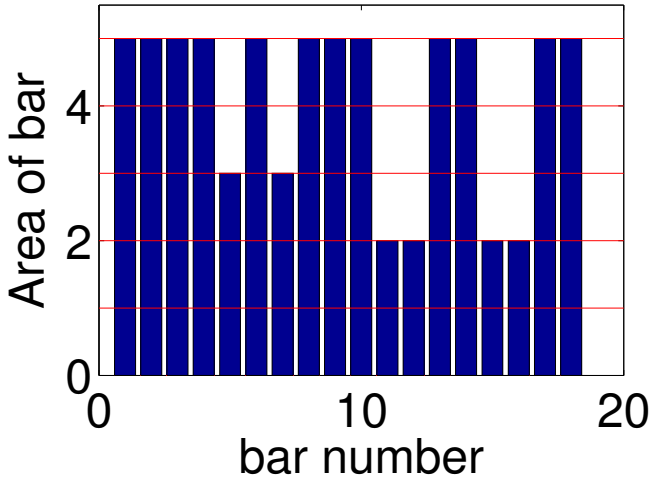

b Bar Areas

Figure A.16: Simple GS Cantilever Beam Result

in that corresponding design variable turning on before others.

To demonstrate turning on the design variables in the correct order, we again examine the simple tension case as seen in Fig. A.2. Here, we want the design variable ϕ_1^e to become one before ϕ_2^e, before ϕ_3^e, etc. It can be seen in Fig. A.18 that the same solution is obtained as in Fig. A.2, however, design variables 1-3 and 1-4 for bar members 1 and 2 respectively are driven to one. This is in contrast to the 3-5 and 2-5 as seen in Fig. A.2.

While the order makes no difference for the uniform ΔA, it is required when the

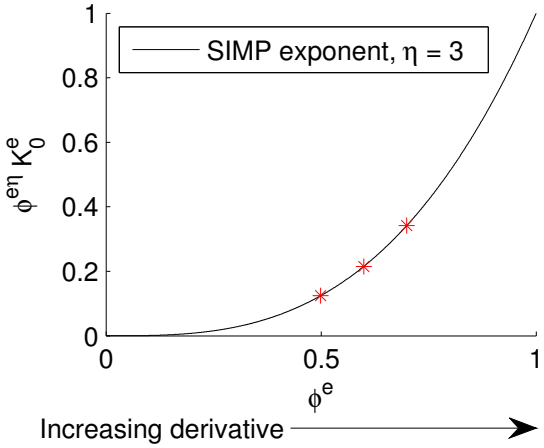

Figure A.17: No heaviside required

ΔA are not uniform. Investigating some more complicated examples, the algorithm is seen to behave quite nicely for fairly arbitrary ΔA. In Fig. A.19, the bridge problem is solved using a relatively arbitrary assortment of ΔA. The red bars indicate truss member which contain a design variable that was not driven all the way to one. As explained above, this is due to the volume constraint. The design variables do, in fact, turn on in the desired order, even for these members.

A.5 Conclusions

There are some limitations to the method. Most notably, the non-uniform discrete method will almost always fail on the force inverter problem. This is due to the sign of the sensitivities changing from negative to positive. The logic of starting the design variables at different starting points along the SIMP curve only holds true if the sign of the sensitivities remains the same. Also, as noted earlier, there is almost no way to

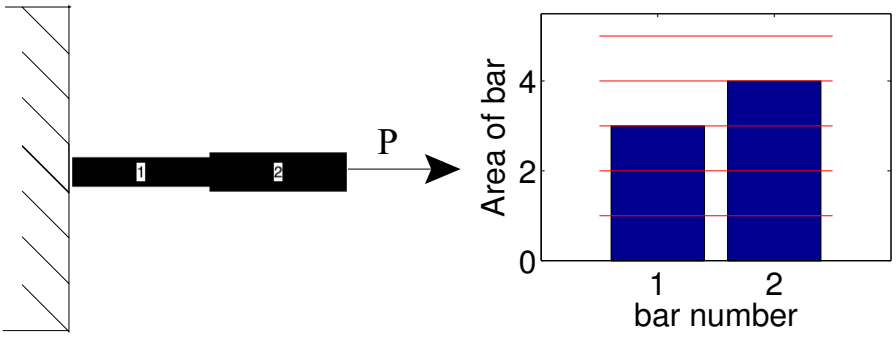

a Solution **b** Final Bar Areas

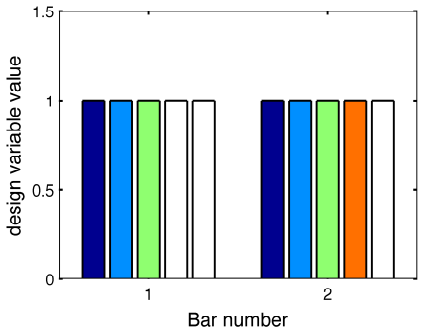

c Design Variables

Figure A.18: Simple tension example optimization results

end up with every bar element at one of the predefined allowable areas. The algorithm will always end with the volume constraint being active, since adding material will always decrease the compliance (even if adding material is made inefficient by the SIMP exponent).

APPENDIX A. A GRADIENT-BASED APPROACH TO TRUSS TOPOLOGY OPTIMIZATION WITH INTEGER DESIGN VARIABLE CONSTRAINTS

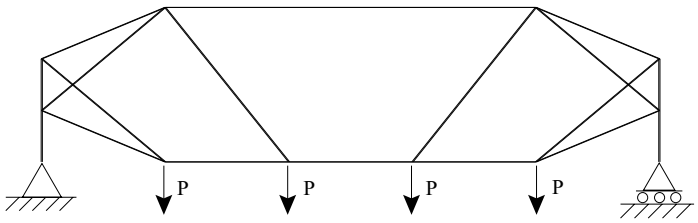

a Optimized Topology

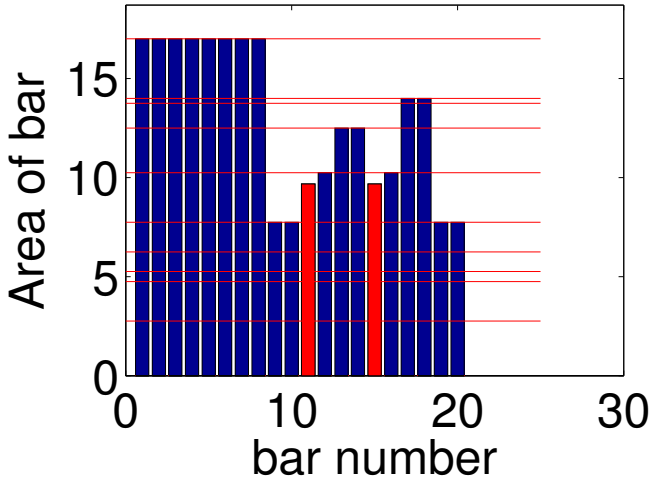

b Bar Areas

Figure A.19: Bridge Results with arbitrary ΔA

Bibliography

Design of concrete structures can3-a23.3-m84. In *CSA Technical Committee A23.3*, Rexdale, Ontario, 1984. Canadian Standards Association.

Ceb-fip model code 1990. In *Comité Euro-International du Béton*, London, 1993. Thomas Telford Services, Ltd.

Building code requirements for structural concrete (aci 318-02) and commentary (aci 318r-02). In *ACI Committee 318*, Farmington Hills, Michigan, 2002. American Concrete Institute.

Objet 350 connex: Build mid-size prototypes in multiple materials, 2009. URL `http://stratasys.com/3d-printers/design-series/precision/objet-connex350`.

Brigham young compliant mechanism research group: Grippers, Dec. 2014. URL `http://compliantmechanisms.byu.edu/image-gallery/grippers`.

Fdm technology, Nov. 2014. URL `http://www.stratasys.com/3d-printers/technologies/fdm-technology/`.

BIBLIOGRAPHY

Fortus 360mc and 400mc systems: Build strong, accurate parts, 2015. URL `http://www.stratasys.com/3d-printers/production-series/fortus-360-400mc`.

Uprint se: Professional powerhouse, 2015. URL `http://www.stratasys.com/3d-printers/idea-series/uprint-se`.

W. Achtziger. Truss topology optimization including bar properties different for tension and compression. *Structural Optimization*, 12(1):63–74, 1996.

W. Achtziger and M. Stolpe. Truss topology optimization with discrete design variables-guaranteed global optimality and benchmark examples. *Structural and Multidisciplinary Optimization*, 34(1):1–20, 2007. cited By (since 1996) 20.

W. Achtziger, M. Bendsøe, A. Ben-Tal, and J. Zowe. Equivalent displacement based formulations for maximum strength truss topology design. *IMPACT of Computing in Science and Engineering*, 4(4):315–345, 1992. cited By (since 1996)43.

H. Adeli and H. Park. Optimization of space structures by neural dynamics. *Neural Networks*, 8(5):769–781, 1995. cited By (since 1996)60.

M. Aguirre and M. Frecker. Design and optimization of hybrid compliant narrow-gauge surgical forceps. volume 1, pages 779–788, 2010. cited By (since 1996)1.

M. Ali and R. White. Automatic generation of truss model for optimal design of reinforced concrete structures. *ACI Structural Journal*, 98(4):431–442, 2001.

BIBLIOGRAPHY

H. Almeida and P. Brtolo. Topological optimisation of scaffolds for tissue engineering. volume 59, pages 298–306, 2013. cited By 0.

AASHTO LRFD Bridge Specifications. American Association of State Highway and Transportation Officials, Washington, D.C., 1 edition, 1994.

O. Amir and M. Bogomolny. Topology optimization for conceptual design of reinforced concrete structures. In *Proceedings of the 9th World Congress on Structural and Multidisciplinary Optimization*, Shizuoka, Japan, June 2011.

O. Amir and O. Sigmund. Reinforcement layout design for concrete structures based on continuum damage and truss topology optimization. *Structural and Multidisciplinary Optimization*, 47(2):157–174, 2013. cited By (since 1996)5.

E. Andreassen, B. Lazarov, and O. Sigmund. Design of manufacturable 3d extremal elastic microstructure. *Mechanics of Materials*, 69:1–10, 2014. cited By (since 1996)2.

A. Aremu, I. Ashcroft, R. Wildman, R. Hague, C. Tuck, and D. Brackett. A hybrid algorithm for topology optimization of additive manufactured structures. pages 279–289, 2011. cited By (since 1996)1.

J. S. Arora. Guide to structural optimization. Technical Report 90, American Society of Civil Engineers, 1997. cited By 10.

A. Asadpoure, M. Tootkaboni, and J. K. Guest. Robust topology optimization of

structures with uncertainties in stiffness–application to truss structures. *Computers & Structures*, 89(11):1131–1141, 2011.

S. A. Bailey, J. G. Cham, M. R. Cutkosky, and R. J. Full. Biomimetic robotic mechanisms via shape deposition manufacturing. pages 403–410, Snowbird, UT, October 1999.

W. Bejgerowski, J. Gerdes, S. Gupta, H. Bruck, and S. Wilkerson. Design and fabrication of a multi-material compliant flapping wing drive mechanism for miniature air vehicles. volume 2, pages 69–80, 2010. cited By (since 1996)5.

W. Bejgerowski, J. Gerdes, S. Gupta, and H. Bruck. Design and fabrication of miniature compliant hinges for multi-material compliant mechanisms. *International Journal of Advanced Manufacturing Technology*, 57(5-8):437–452, 2011. cited By (since 1996)5.

M. Bendsøe. Optimal shape design as a material distribution problem. *Structural Optimization*, 1(4):193–202, 1989.

M. Bendsøe and N. Kikuchi. Generating optimal topologies in structural design using a homogenization method. *Computer Methods in Applied Mechanics and Engineering*, 71(2):197–224, 1988.

M. Bendsøe and O. Sigmund. *Topology Optimization: Theory, Methods, and Applications*. Springer-Verlag, Berlin, 2003a.

BIBLIOGRAPHY

M. Bendsøe, A. Ben-Tal, and J. Zowe. Optimization methods for truss geometry and topology design. *Structural Optimization*, 7(3):141–159, 1994.

M. P. Bendsøe and O. Sigmund. Material interpolation schemes in topology optimization. *Archive of Applied Mechanics*, 69(9-10):635–654, 1999. ISSN 0939-1533.

M. P. Bendsøe and O. Sigmund. *Topology optimization: Theory, methods and applications*. Springer, Berlin, 2003b.

F. Biondini, F. Bontempi, and P. Malerba. Optimal strut-and-tie models in reinforced concrete structures. *Computer Assisted Mechanics and Engineering Sciences*, 6(3): 279–293, 1999.

D. Brackett, I. Ashcroft, and R. Hague. Topology optimization for additive manufacturing. pages 348–362, 2011a. cited By (since 1996)4.

D. Brackett, I. Ashcroft, and R. Hague. A dithering based method to generate variable volume lattice cells for additive manufacturing. pages 671–679, 2011b. cited By (since 1996)1.

M. Bruggi. Generating strut-and-tie patterns for reinforced concrete structures using topology optimization. *Computers and Structures*, 87(23-24):1483–1495, 2009.

T. Bruns and D. Tortorelli. Topology optimization of non-linear elastic structures and compliant mechanisms. *Computer Methods in Applied Mechanics and Engineering*, 190(26-27):3443–3459, 2001.

BIBLIOGRAPHY

A. Bryan, S. Hu, and Y. Koren. Assembly system reconfiguration planning. *Journal of Manufacturing Science and Engineering, Transactions of the ASME*, 135(4), 2013. cited By (since 1996)0.

T. Buhl, C. Pedersen, and O. Sigmund. Stiffness design of geometrically nonlinear structures using topology optimization. *Structural and Multidisciplinary Optimization*, 19(2):93–104, 2000.

K. Cai. A simple approach to find optimal topology of a continuum with tension-only or compression-only material. *Structural and Multidisciplinary Optimization*, 43 (6):827–835, 2011.

C. Camp and B. Bichon. Design of space trusses using ant colony optimization. *Journal of Structural Engineering*, 130(5):741–751, 2004. cited By (since 1996) 68.

H. Carlo, J. Patrick Spicer, and A. Rivera-Silva. Simultaneous consideration of scalable-reconfigurable manufacturing system investment and operating costs. *Journal of Manufacturing Science and Engineering, Transactions of the ASME*, 134(1), 2012. cited By (since 1996)3.

J. Carstensen and J. Guest. New projection methods for two-phase minimum and maximum length scale control in topology optimization. 2014.

V. Challis, A. Roberts, J. Grotowski, L.-C. Zhang, and T. Sercombe. Prototypes for bone implant scaffolds designed via topology optimization and manufactured

by solid freeform fabrication. *Advanced Engineering Materials*, 12(11):1106–1110, 2010. cited By (since 1996)17.

V. Challis, J. Guest, J. Grotowski, and A. Roberts. Computationally generated cross-property bounds for stiffness and fluid permeability using topology optimization. *International Journal of Solids and Structures*, 49(23-24):3397–3408, 2012. cited By (since 1996)6.

Y. Chen and S. Wang. Computer-aided product design with performance-tailored mesostructures. *Computer-Aided Design and Applications*, 5(1-4):565–576, 2008. cited By (since 1996)5.

Y. Chen, M. Schellekens, S. Zhou, J. Cadman, W. Li, R. Appleyard, and Q. Li. Design optimization of scaffold microstructures using wall shear stress criterion towards regulated flow-induced erosion. *Journal of Biomechanical Engineering*, 133(8), 2011. cited By 3.

C. Chu, G. Graf, and D. Rosen. Design for additive manufacturing of cellular structures. *Computer-Aided Design and Applications*, 5(5):686–696, 2008. cited By (since 1996)9.

J. Chu, S. Engelbrecht, G. Graf, and D. Rosen. A comparison of synthesis methods for cellular structures with application to additive manufacturing. *Rapid Prototyping Journal*, 16(4):275–283, 2010. cited By (since 1996)9.

BIBLIOGRAPHY

M. Cloots, A. Spierings, and K. Wegener. Assessing new support minimizing strategies for the additive manufacturing technology slm. pages 631–643, 2013. cited By 1.

M. P. Collins and D. Mitchell. Shear and torsion design of prestressed and non-prestressed concrete beams. *Journal - Prestressed Concrete Institute*, 25(5):32–100, 1980.

D. Darwin and D. A. Pecknold. Nonlinear biaxial stress-strain law for concrete. *ASCE J Eng Mech Div*, 103(2):229–241, 1977.

K. Deb and S. Gulati. Design of truss-structures for minimum weight using genetic algorithms. *Finite Elements in Analysis and Design*, 37(5):447–465, 2001. cited By (since 1996)116.

B. Deuser, L. Tang, R. Landers, M. Leu, and G. Hilmas. Hybrid extrusion force-velocity control using freeze-form extrusion fabrication for functionally graded material parts. *Journal of Manufacturing Science and Engineering, Transactions of the ASME*, 135(4), 2013. cited By (since 1996)0.

M. Dias, J. Guedes, C. Flanagan, S. Hollister, and P. Fernandes. Optimization of scaffold design for bone tissue engineering: A computational and experimental study. *Medical Engineering and Physics*, 36(4):448–457, 2014. cited By 1.

C. Emmelmann, P. Sander, J. Kranz, and E. Wycisk. Laser additive manufacturing

and bionics: Redefining lightweight design. volume 12, pages 364–368, 2011. cited By 6.

M. Frecker, G. Ananthasuresh, S. Nishiwaki, N. Kikuchi, and S. Kota. Topological synthesis of compliant mechanisms using multi-criteria optimization. *Journal of Mechanical Design, Transactions of the ASME*, 119(2):238–245, 1997. cited By (since 1996)327.

M. J. G. *Reinforced Concrete: Mechanics and Design.* Prentice-Hall,Inc., 2 edition, 1992. ed. Englewood Cliffs.

A. Gaynor, J. Guest, and C. Moen. Reinforced concrete force visualization and design using bilinear truss-continuum topology optimization. *Journal of Structural Engineering (United States)*, 139(4):607–618, 2013. cited By (since 1996)2.

A. T. Gaynor, N. A. Meisel, C. B. Williams, and J. K. Guest. Multiple-material topology optimization of compliant mechanisms created via polyjet three-dimensional printing. *Journal of Manufacturing Science and Engineering*, 136(6):061015, 2014.

M. Ghasemi, E. Hinton, and R. Wood. Optimization of trusses using genetic algorithms for discrete and continuous variables. *Engineering Computations (Swansea, Wales)*, 16(3):272–301, 1999. cited By (since 1996)46.

R. Gouker, S. Gupta, H. Bruck, and T. Holzschuh. Manufacturing of multi-material compliant mechanisms using multi-material molding. *International Journal of*

BIBLIOGRAPHY

Advanced Manufacturing Technology, 30(11-12):1049–1075, 2006. cited By (since 1996)23.

G. Graf, J. Chu, S. Engelbrecht, and D. Rosen. Synthesis methods for lightweight lattice structures. volume 2, pages 579–589, 2009. cited By (since 1996)1.

A. Groenwold, N. Stander, and J. Snyman. A pseudo-discrete rounding method for structural optimization. *Structural Optimization*, 11(3-4):218–227, 1996. cited By (since 1996) 15.

J. Guest. Imposing maximum length scale in topology optimization. *Structural and Multidisciplinary Optimization*, 37(5):463–473, 2009a.

J. Guest. Topology optimization with multiple phase projection. *Computer Methods in Applied Mechanics and Engineering*, 199(1-4):123–135, 2009b.

J. Guest and L. Smith Genut. Reducing dimensionality in topology optimization using adaptive design variable fields. *International Journal for Numerical Methods in Engineering*, 81(8):1019–1045, 2010a. cited By (since 1996)21.

J. Guest and M. Zhu. Casting and milling restrictions in topology optimization via projection-based algorithms. volume 3, pages 913–920, 2012.

J. Guest, J. Prévost, and T. Belytschko. Achieving minimum length scale in topology optimization using nodal design variables and projection functions. *International Journal for Numerical Methods in Engineering*, 61(2):238–254, 2004.

BIBLIOGRAPHY

J. Guest, A. Asadpoure, and S.-H. Ha. Eliminating beta-continuation from heaviside projection and density filter algorithms. *Structural and Multidisciplinary Optimization*, 44(4):443–453, 2011.

J. K. Guest. A projection-based topology optimization approach to distributing discrete features in structures and materials. *9th World Congress on Structural and Multidisciplinary Optimization, Shizuoka, Japan, June*, pages 13–17, 2011.

J. K. Guest and T. Igusa. Structural optimization under uncertain loads and nodal locations. *Computer Methods in Applied Mechanics and Engineering*, 198(1):116–124, 2008.

J. K. Guest and J. H. Prévost. Optimizing multifunctional materials: design of microstructures for maximized stiffness and fluid permeability. *International Journal of Solids and Structures*, 43(22):7028–7047, 2006.

J. K. Guest and J. H. Prévost. Design of maximum permeability material structures. *Computer Methods in Applied Mechanics and Engineering*, 196(4):1006–1017, 2007.

J. K. Guest and L. C. Smith Genut. Reducing dimensionality in topology optimization using adaptive design variable fields. *International journal for numerical methods in engineering*, 81(8):1019–1045, 2010b.

S.-H. Ha and J. K. Guest. Optimizing inclusion shapes and patterns in periodic

materials using discrete object projection. *Structural and Multidisciplinary Optimization*, pages 1–16, 2014.

P. Hajela and E. Lee. Genetic algorithms in truss topological optimization. *International Journal of Solids and Structures*, 32(22):3341–3357, 1995. cited By (since 1996) 88.

D. Hofmann, H. Huang, and G. Reinhart. Automated shape optimization of orienting devices for vibratory bowl feeders. *Journal of Manufacturing Science and Engineering, Transactions of the ASME*, 135(5), 2013. cited By (since 1996)1.

L. Howell. Compliant mechanisms. In J. M. McCarthy, editor, *21st Century Kinematics*, pages 189–216. Springer London, 2013. ISBN 978-1-4471-4509-7. doi: 10.1007/978-1-4471-4510-3_7.

A. Hussein, L. Hao, C. Yan, R. Everson, and P. Young. Advanced lattice support structures for metal additive manufacturing. *Journal of Materials Processing Technology*, 213(7):1019–1026, 2013.

M. Jalalpour, T. Igusa, and J. K. Guest. Optimal design of trusses with geometric imperfections: accounting for global instability. *International Journal of Solids and Structures*, 48(21):3011–3019, 2011.

M. Jansen, G. Lombaert, M. Diehl, B. Lazarov, O. Sigmund, and M. Schevenels.

BIBLIOGRAPHY

Robust topology optimization accounting for misplacement of material. *Structural and Multidisciplinary Optimization*, 47(3):317–333, 2013. cited By (since 1996)3.

A. Keshavarz Panahi, H. Mianajiy, E. Miandoabchi, and M. Hussaini Fareed. Optimization of the powder injection molding process parameters using the sequential simplex algorithm and sensitivity analysis. *Journal of Manufacturing Science and Engineering, Transactions of the ASME*, 135(1), 2013. cited By (since 1996)0.

U. Kirsch. Optimal topologies of truss structures. *Computer Methods in Applied Mechanics and Engineering*, 72(1):15–28, 1989. cited By (since 1996)40.

T. Krol, M. Zaeh, and C. Seidel. Optimization of supports in metal-based additive manufacturing by means of finite element models. pages 707–718, 2012. cited By 0.

D. Kuchma, S. Yindeesuk, T. Nagle, J. Hart, and H. Lee. Experimental validation of strut-and-tie method for complex regions. *ACI Structural Journal*, 105(5):578–589, 2008.

H.-G. Kwak and S.-H. Noh. Determination of strut-and-tie models using evolutionary structural optimization. *Engineering Structures*, 28(10):1440–1449, 2006.

N. Lei, S. Moon, and G. Bi. Additive manufacturing and topology optimization to support product family design. pages 505–510, 2014. cited By 0.

J. Leng, Z. Li, J. Guest, and B. Schafer. Shape optimization of cold-formed steel

columns with manufacturing constraints and limited number of rollers. pages 313–331, 2013. cited By (since 1996)2.

L.-J. Leu, C.-W. Huang, C.-S. Chen, and Y.-P. Liao. Strut-and-tie design methodology for three-dimensional reinforced concrete structures. *Journal of Structural Engineering*, 132(6):929–938, 2006.

Y. Li, Y. Chen, and C. Zhou. Design of flexible skin for target displacements based on meso-structures. volume 2, pages 611–624, 2009. cited By (since 1996)0.

Q. Liang, Y. Xie, and G. Prentice Steven. Topology optimization of strut-and-tie models in reinforced concrete structures using an evolutionary procedure. *ACI Structural Journal*, 97(2):322–330, 2000.

J. Luo, Z. Luo, S. Chen, L. Tong, and M. Wang. A new level set method for systematic design of hinge-free compliant mechanisms. *Computer Methods in Applied Mechanics and Engineering*, 198(2):318–331, 2008. cited By (since 1996)37.

U. Maheshwaraa, D. Bourell, and C. Seepersad. Design and freeform fabrication of deployable structures with lattice skins. *Rapid Prototyping Journal*, 13(4):213–225, 2007. cited By (since 1996)11.

P. Marti. On plastic analysis of reinforced concrete, report no. 104. Zurich, 1980. Institute of Structural Engineers, ETH.

BIBLIOGRAPHY

K. Maute and E. Ramm. Adaptive topology optimization. *Structural Optimization*, 10(2):100–112, 1995. cited By (since 1996)63.

K. Maute, S. Schwarz, and E. Ramm. Adaptive topology optimization of elastoplastic structures. *Structural Optimization*, 15(2):81–91, 1998.

N. A. Meisel, A. M. Elliott, and C. B. Williams. A procedure for creating actuated joints via embedding shape memory alloys in polyjet 3d printing. *Journal of Intelligent Material Systems and Structures*, page 1045389X14544144, 2014.

P. Mercelis and J.-P. Kruth. Residual stresses in selective laser sintering and selective laser melting. *Rapid Prototyping Journal*, 12(5):254–265, 2006.

K. Mumtaz, P. Vora, and N. Hopkinson. A method to eliminate anchors/supports from directly laser melted metal powder bed processes. pages 55–64, 2011.

P. Nagarajan and T. Pillai. Analysis and design of simply supported deep beams using strut and tie method. *Advances in Structural Engineering*, 11(5):491–499, 2008.

M. Ohsaki and C. Swan. *Topology and geometry optimization of trusses and frames*. 2002.

L. Pang and H. Kishawy. Modified primary shear zone analysis for identification of material mechanical behavior during machining process using genetic algorithm.

BIBLIOGRAPHY

Journal of Manufacturing Science and Engineering, Transactions of the ASME, 134(4), 2012. cited By (since 1996)2.

H. Park and T. Anh. Development of evolutionary method for optimizing a roll forming process of aluminum parts. *Journal of Manufacturing Science and Engineering, Transactions of the ASME*, 134(2), 2012. cited By (since 1996)0.

R. Paul and S. Anand. Optimization of layered manufacturing process for reducing form errors with minimal support structures. *Journal of Manufacturing Systems*, 2014. cited By 0; Article in Press.

D. Pham and R. Gault. A comparison of rapid prototyping technologies. *International Journal of Machine Tools and Manufacture*, 38(10-11):1257 – 1287, 1998. ISSN 0890-6955. doi: http://dx.doi.org/10.1016/S0890-6955(97)00137-5.

T. Poulsen. A new scheme for imposing a minimum length scale in topology optimization. *International Journal for Numerical Methods in Engineering*, 57(6):741–760, 2003.

A. Rainer, S. Giannitelli, D. Accoto, S. De Porcellinis, E. Guglielmelli, and M. Trombetta. Load-adaptive scaffold architecturing: A bioinspired approach to the design of porous additively manufactured scaffolds with optimized mechanical properties. *Annals of Biomedical Engineering*, 40(4):966–975, 2012. cited By 6.

S. Rajagopalan, R. Goldman, K.-H. Shin, V. Kumar, M. Cutkosky, and D. Dutta.

BIBLIOGRAPHY

Representation of heterogeneous objects during design, processing and freeform-fabrication. *Materials and Design*, 22(3):185–197, 2001. cited By (since 1996)16.

S. Rajan. Sizing, shape, and topology design optimization of trusses using genetic algorithm. *Journal of structural engineering New York, N.Y.*, 121(10):1480–1487, 1995. cited By (since 1996)114.

S. Rajeev and C. Krishnamoorthy. Genetic algorithms-based methodologies for design optimization of trusses. *Journal of Structural Engineering*, 123(3):350–358, 1997. cited By (since 1996)108.

J. Rajkowski, A. Gerratt, E. Schaler, and S. Bergbreiter. A multi-material milli-robot prototyping process. pages 2777–2782, 2009. cited By (since 1996)1.

M. Rasmussen and M. Stolpe. Global optimization of discrete truss topology design problems using a parallel cut-and-branch method. *Computers and Structures*, 86 (13-14):1527–1538, 2008. cited By (since 1996)18.

G. Reddy and J. Cagan. Improved shape annealing algorithm for truss topology generation. *Journal of Mechanical Design, Transactions of the ASME*, 117(2 A): 315–321, 1995. cited By (since 1996)38.

J. Riddick, A. Hall, M. Haile, R. von Wahlde, D. Cole, and S. Biggs. Effect of manufacturing parameters on failure in acrylonitrile-butadiane-styrene fabricated by fused deposition modeling. 2012.

BIBLIOGRAPHY

D. Rosen. Computer-aided design for additive manufacturing of cellular structures. *Computer-Aided Design and Applications*, 4(1-6):585–594, 2007. cited By (since 1996)38.

G. Rozvany. Some shortcomings in michell's truss theory. *Structural and Multidisciplinary Optimization*, 12(4):244–250, 1996.

G. Rozvany, M. Zhou, and T. Birker. Generalized shape optimization without homogenization. *Structural optimization*, 4(3-4):250–252, 1992. ISSN 0934-4373.

A. Saxena. On multiple-material optimal compliant topologies: Discrete variable parameterization using genetic algorithm. volume 5 A, pages 85–96, 2002. cited By (since 1996)5.

A. Saxena. Topology design of large displacement compliant mechanisms with multiple materials and multiple output ports. *Structural and Multidisciplinary Optimization*, 30(6):477–490, 2005. cited By (since 1996)41.

M. Schevenels, B. Lazarov, and O. Sigmund. Robust topology optimization accounting for spatially varying manufacturing errors. *Computer Methods in Applied Mechanics and Engineering*, 200(49-52):3613–3627, 2011. cited By (since 1996)26.

J. Schlaich, K. Schaefer, and M. Jennewein. Toward a consistent design of structural concrete. *PCI Journal*, 32(3):74–150, 1987.

BIBLIOGRAPHY

O. Sigmund. Tailoring materials with prescribed elastic properties. *Mechanics of Materials*, 20(4):351–368, 1995. cited By (since 1996)124.

O. Sigmund. On the design of compliant mechanisms using topology optimization. *Mechanics of Structures and Machines*, 25(4):493–524, 1997. cited By (since 1996)523.

O. Sigmund. Manufacturing tolerant topology optimization. *Acta Mechanica Sinica/Lixue Xuebao*, 25(2):227–239, 2009. cited By (since 1996)57.

O. Sigmund and J. Petersson. Numerical instabilities in topology optimization: A survey on procedures dealing with checkerboards, mesh-dependencies and local minima. *Structural Optimization*, 16(1):68–75, 1998. cited By (since 1996)616.

C. Smith, I. Todd, and M. Gilbert. Utilizing additive manufacturing techniques to fabricate weight optimized components designed using structural optimization methods. pages 879–894, 2013. cited By 0.

R. Stainko. An adaptive multilevel approach to the minimal compliance problem in topology optimization. *Communications in Numerical Methods in Engineering*, 22 (2):109–118, 2006. cited By (since 1996)17.

M. Stolpe and K. Svanberg. An alternative interpolation scheme for minimum compliance topology optimization. *Structural and Multidisciplinary Optimization*, 22 (2):116–124, 2001.

BIBLIOGRAPHY

G. Strano, L. Hao, R. Everson, and K. Evans. A new approach to the design and optimisation of support structures in additive manufacturing. *International Journal of Advanced Manufacturing Technology*, 66(9-12):1247–1254, 2013. cited By 3.

K. Svanberg. Method of moving asymptotes - a new method for structural optimization. *International Journal for Numerical Methods in Engineering*, 24(2):359–373, 1987.

C. Swan and I. Kosaka. Voigt-reuss topology optimization for structures with nonlinear material behaviors. *International Journal for Numerical Methods in Engineering*, 40(20):3785–3814, 1997.

P. Tanskanen. The evolutionary structural optimization method: Theoretical aspects. *Computer Methods in Applied Mechanics and Engineering*, 191(47-48):5485–5498, 2002. cited By (since 1996)64.

D. Thomas. *The Development of Design Rules for Selective Laser Melting.* PhD thesis, University of Wales Institute, 10 2009.

B. Vandenbroucke and J. Kruth. Selective laser melting of biocompatible metals for rapid manufacturing of medical parts. *Rapid Prototyping Journal*, 13(4):196–203, 2007.

M. Victoria, O. Querin, and P. Martií. Generation of strut-and-tie models by topology

design using different material properties in tension and compression. *Structural and Multidisciplinary Optimization*, 44(2):247–258, 2011.

L. Villalpando, H. Eiliat, and R. Urbanic. An optimization approach for components built by fused deposition modeling with parametric internal structures. volume 17, pages 800–805, 2014. cited By 0.

S. Vogel. Better bent than broken. *Discovery*, 16(5):62–67, 1995.

D. Vogtmann, S. Gupta, and S. Bergbreiter. A systematic approach to designing multi-material miniature compliant mechanisms. volume 6, pages 211–221, 2011. cited By (since 1996)3.

H. Wang and D. Rosen. An automated design synthesis method for compliant mechanisms with application to morphing wings. volume 2006, 2006. cited By (since 1996)2.

H. Wang and D. W. Rosen. Computer-aided design methods for the additive fabrication of truss structures. Atlanta, GA, 2001. Georgia Institute of Technology.

H. Wang, Y. Chen, and D. Rosen. A hybrid geometric modeling method for large scale conformal cellular structures. volume 3 A, pages 421–427, 2005. cited By (since 1996)4.

C. Xu, W. Chai, Y. Huang, and R. Markwald. Scaffold-free inkjet printing of three-

dimensional zigzag cellular tubes. *Biotechnology and Bioengineering*, 109(12):3152–3160, 2012.

Y. Yang, C. D. Moen, and J. K. Guest. Three-dimensional force flow paths and reinforcement design in concrete via stress-dependent truss-continuum topology optimization. *Journal of Engineering Mechanics*, 2014.

Vita

Andrew Gaynor was born on September 20$^{\text{th}}$, 1987 in Arlington Heights, Illinois. He received his Bachelor's of Civil Engineering Degree from the University of Minnesota in 2010. Upon graduation, he enrolled in the Ph.D. program in the Civil Engineering program at Johns Hopkins University. Andy participates in a number of on campus activities including the Johns Hopkins Graduate Representative Organization (GRO) and was a founding member of the JHU Civil Engineering Graduate Association (CEGA). While at Hopkins, Andy received a number of Fellowship awards including the George Jenkins II fellowship and the NSF IGERT Traineeship. His work primarily focuses on developing novel topology optimization algorithms to design for particular materials and/or manufacturing methods. His works has been published in both ASCE and ASME journals and has been presented at conferences organized by ISSMO, ASCE, ASME and AIAA.